C00-3130TC-38

A Study of the Weak Neutral Current and the Electronmagnetic Properties of the Muon Neutrino

by

Milind Vaman Diwan

B.A., University of Colorado at Boulder, 1982

Sc.M., Brown University, 1984

Report

A major portion of this report was submitted
in partial fulfillment of the requirements for the
Degree of Doctor of Philosophy
in the Department of Physics at Brown University

July 1988

This thesis is dedicated to my grandparents

Sripad Hanumant Diwan

and

Ramabai Sripad Diwan

असे कसे काय?

Vita

The author was born in Pune, India, on 9 April 1963. He graduated from City High School in the town of Sangli, Maharashtra. He came to the United States in 1978. After attending the Panhandle State University of Oklahoma for a year and the University of Colorado at Boulder for three, he graduated with a B.A. in Physics from the University of Colorado. He came to Brown University in 1982.

Acknowledgments

I have been very lucky to gain many friendships during my stay at Brown. I would like to mention them all, but because of limited space let me mention those whom I esteem the most.

My advisor, Prof. Robert Lanou, has been kind, generous, and inspiring. He has often cleared my mind, sometimes with only a word. I thank Prof. David Cutts, who has nearly been a second advisor, for making me feel welcome at his home. I have had the fortune of working on a superb experiment with a very bright and driven group of people. I want to thank Dr. Michael Murtagh for the advice and the care he has shown me. I would like to thank Fern Coyle for the meticulous book keeping. I also thank Marty Van Lith for a difficult job well done. I thank Dr. Takao Shinkawa, Prof. Stanley Durkin, Prof. David Hedin , Dr. John Callas, Dr. Eric Stern, Dr. Yoshi Kurihara, and Dr. Keigo Yamaguchi for their constant help. I thank Greg Fortin for all the trouble shooting. I thank Mitch Newcomer for the late night chats. I thank Dr. D. H. White and Prof. Alfred Mann for their guidance. I want to thank many others , especially those who kept the accelerator and the experiment functioning, but I have never even met some of them.

I want to thank Kaushik De, Piali De, Vivian Odell, Edward Holupka, Brinda Mehta, Shiv Khemka, and also all the members of my graduate class for a great period of companionship. My special thanks to Emy Tseng for being such a good friend. My special thanks to Eileen Wong for proof reading, suggesting changes and for being a friend in need. Also my special thanks to my apartment mates and fellow graduate students, Mike Altman, Anthony Panteziris, Mihir Desai, and Spurgeon Keeney, for the excited long conversations which I will always remember. How can I thank everybody whose belief in me made it possible? Never a discouraging word did I hear from anyone. Thank you, my friends, for always being interested in what I had to say.

I cannot thank my mother and father enough for the long years of care, for instilling a sense of purpose, and a sense of history. I thank my brothers, Madhav and Mahesh, for their complete trust in me.

This work was partially supported by the U.S. Department of Energy,

contract number DEAC02-76ER03130.

Contents

List of Figures

List of Tables

Chapter 1.

Introduction.

1. The Standard Model:

The Standard Model of Electro-weak Interactions(SM) [1–3] is a gauge theory that decribes electromagnetic and weak interactions as manifestations of a single force. It is based on the symmetry group $SU(2)_L \times U(1)$. The $SU(2)_L$ gauge field gives three gauge bosons and the $U(1)$ gives one. The weak neutral current and the electromagnetic current are a result of mixing the neutral component of the $SU(2)_L$ gauge field and the $U(1)$ gauge field. A free parameter, $\sin^2\theta_w$, gives the strength of this mixing. Because of the mixing, weak neutral current coupling, charged current coupling , electromagnetic coupling, and the masses of the vector bosons are all related to $\sin^2\theta_w$, the electro-weak mixing angle, also known as the Weinberg angle. The Standard Model has been tested repeatedly during the last decade. With the discoveries of the Z^0, W^+ and W^- particles [4–5], current understanding of electro-weak interactions seems to be extremely accurate.

Even with all its successes, the SM need not be the most basic theory of particle physics. There is a consensus among experts that there must exist a fundamental theory of which the SM is an approximation. Many such Grand Unified Theories have been postulated, the most recent of them being the Theory of Superstrings. In order to further determine the nature of the true theory, we must make precise measurements of all parameters in the SM and reconcile differences in measurements using various techniques. Any deviations in these comparisons should point towards new physics such as additional heavier intermediate vector bosons. The measurements should also constrain the Grand Unified Theories. For example, a theory, developed by Georgi and Glashow [6], based on the gauge group $SU(5)$ has now been ruled out by experiments that measure the lifetime of the proton [7]. This theory like many others predicts a specific value for $\sin^2\theta_w$. An accurate measurement of $\sin^2\theta_w$ points towards the correct path to a unified theory of matter.

The most direct determination of the Weinberg angle is derived from measurements of the masses of the intermediate vector bosons[4,5]. Cross sections of reactions that occur through the neutral current also depend on $\sin^2\theta_w$. Ideally, we want to measure $\sin^2\theta_w$ from all possible neutral current reactions at all energy scales and correct these measurements to compare them with the measurements at the natural energy scale of weak interactions. A recent analysis of all data previous to this work can be found in Ref. 8.

The simplest of the neutral current reactions are in the lepton sector. $\nu_\mu e \rightarrow \nu_\mu e$ and $\bar{\nu}_\mu e \rightarrow \bar{\nu}_\mu e$ scattering reactions occur at a low energy scale. These low Q^2 reactions are not complicated by corrections due to strong or electromagnetic interactions; they occur purely through the weak neutral current; the cross sections have a simple dependence on $\sin^2\theta_w$; the two body kinematics allow for exact theoretical calculations, and as we shall see, the kinematics also facilitate identification of the signal in the E-734 detector.

2. $\nu_\mu + e \rightarrow \nu_\mu + e$ and $\bar{\nu}_\mu + e \rightarrow \bar{\nu}_\mu + e$ Scattering:

The two body scattering reactions can be completely described by a single quantity(see Fig. 1.2.1). The quantity of choice in this experiment is the laboratory angle of the recoiling electron with respect to the direction of the neutrino. Nevertheless, in this experiment both the angle and the energy of the electron are measured. Conservation of energy and momentum relates the neutrino energy to the direction and the energy of the recoiling electron. The mass of the neutrino is assumed to be zero.

$$E_\nu = \frac{m_e(E_e - m_e)}{({E_e}^2 - {m_e}^2)^{1/2}\cos\theta - (E_e - m_e)}$$

We define $T_e = (E_e - m_e)$ as the kinetic energy of the electron and rewrite above equation.

$$cos\theta = \frac{T_e(1 + m_e/E_\nu)}{({T_e}^2 + 2T_e m_e)^{1/2}}$$

Since $m_e << T_e$ and $m_e << E_\nu$ appropriate approximations lead to an interesting limit on the observed angle of the electron.

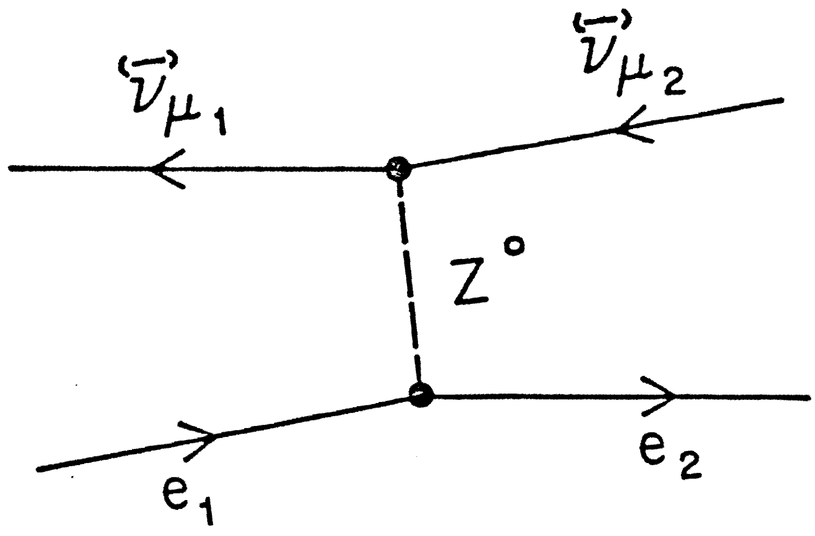

(a)

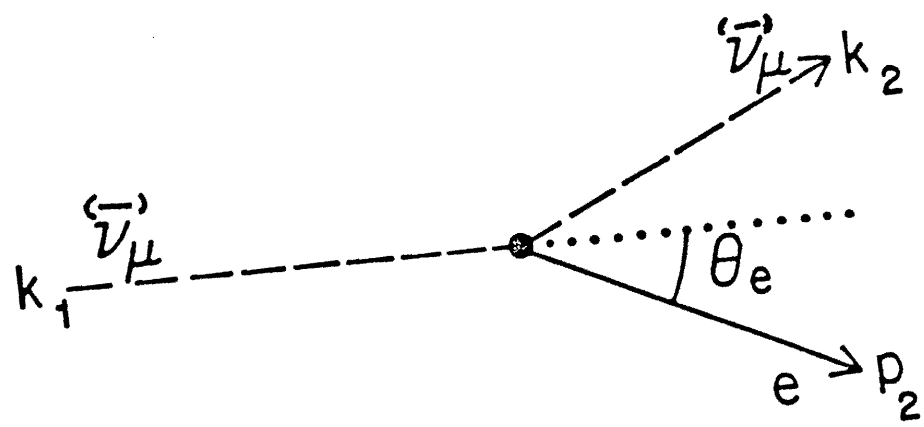

(b)

Figure 1.2.1 Feynman diagram(a) and kinematics (b) for $\nu_\mu e \rightarrow \nu_\mu e$ or $\bar{\nu}_\mu e \rightarrow \bar{\nu}_\mu e$ scattering.

$$\theta^2 < \frac{2m_e}{T_e}$$

We expect to observe electrons of energies greater than 0.2GeV in our detector. Thus we conclude that all the electrons observed from these reactions should have angles less than $.005 rad^2$ with respect to the neutrino beam. If the detector is capable of fine angular resolution in the forward direction we expect to see a sharp peak at low angles in the angular distribution of electromagnetic showers.

3. Cross sections:

Elastic scattering of muon neutrinos and electrons is supressed to first order if all weak currents are charged currents. Existence of the neutral weak current, nevertheless, makes these reactions possible. They occur through the exchange of the neutral intermediate vector boson, Z^0. The Weinberg-Salam Lagrangian gives us the means to calculate the cross section of this process. The coupling of the Z^0 with a lepton is given by the following part of the Lagrangian. The sum is over all generations of leptons.

$$L_{nc} = \sum_l \frac{g}{4\cos\theta_w}[\bar{\nu}_l\gamma_\epsilon(1+\gamma_5)\nu_l + 2\bar{l}\gamma_\epsilon(g_v + g_a\gamma_5)l]Z^\epsilon$$

$$e = g\sin\theta_w$$

$$g_v = -1/2 + 2\sin^2\theta_w$$

$$g_a = -1/2$$

For low energy (1GeV) interactions we can write an effective current-current Lagrangian in the limit of an infinitely heavy Z boson.

$$L_{eff} = \frac{\rho G}{2\sqrt{2}} J_{n\epsilon} {J_n}^{\dagger\epsilon}$$

$${J_n}^\epsilon = \sum_l [\bar{\nu}_l\gamma^\epsilon(1+\gamma_5)\nu_l + 2\bar{l}\gamma^\epsilon(g_v + g_a\gamma_5)l]$$

$$\frac{G}{\sqrt{2}} = \frac{e^2}{8{M_W}^2\sin^2\theta_w}$$

A similar effective Lagrangian exists for the charged current. The factor ρ quantifies the possibility of the neutral current having a different coupling strength than the charged current. In the Standard Model, $\rho = 1$. From these relations, we can calculate the differential cross sections for $\nu_\mu e \to \nu_\mu e$ and $\bar{\nu}_\mu e \to \bar{\nu}_\mu e$.

$$\frac{d\sigma}{dy}(\nu_\mu e) = \frac{\rho^2 G^2 m_e E_\nu}{2\pi}[(g_v + g_a)^2 + (g_v - g_a)^2(1-y)^2 - ({g_v}^2 - {g_a}^2)\frac{m_e y}{E_\nu}]$$

$$\frac{d\sigma}{dy}(\bar{\nu}_\mu e) = \frac{\rho^2 G^2 m_e E_\nu}{2\pi}[(g_v - g_a)^2 + (g_v + g_a)^2(1-y)^2 - ({g_v}^2 - {g_a}^2)\frac{m_e y}{E_\nu}]$$

where $y = (E_e - m_e)/E_\nu$. By changing variables from y to θ^2 we can obtain $\frac{d\sigma}{d\theta^2}$. The cross sections are illustrated in Fig. 1.3.1. The very sharp peak in the forward direction is obvious. For accelerator energies, $E_\nu >> m_e$; the last term in above differential cross sections is therefore negligible. Integration of the differential cross sections yields the total cross sections.

$$\sigma(\nu_\mu e) = \frac{\rho^2 G^2 m_e E_\nu}{2\pi}[(g_v + g_a)^2 + \frac{1}{3}(g_v - g_a)^2]$$

$$\sigma(\bar{\nu}_\mu e) = \frac{\rho^2 G^2 m_e E_\nu}{2\pi}[(g_v - g_a)^2 + \frac{1}{3}(g_v + g_a)^2]$$

The cross sections are linearly dependent on the neutrino energy. The linear dependence cannot be correct for arbitrarily high energies and is good only for low energies compared to the mass of the Z^0 (90 GeV). The parameters to be determined are $\sin^2\theta_w$ and ρ. The ratio of the cross sections $R = \frac{\sigma(\nu_\mu e)}{\sigma(\bar{\nu}_\mu e)}$ gives an expression for $\sin^2\theta_w$ independent of ρ^2.

$$R = 3\frac{1 - 4\sin^2\theta_w + \frac{16}{3}\sin^4\theta_w}{1 - 4\sin^2\theta_w + 16\sin^4\theta_w}$$

This expression can be inverted to get $\sin^2\theta_w$.

$$\sin^2\theta_w = \frac{(R-3) + \sqrt{(3-R)^2 + 4(R-1)(3-R)}}{8(R-1)}$$

The cross sections and ratio are plotted in figures 1.3.1 and 1.3.2.

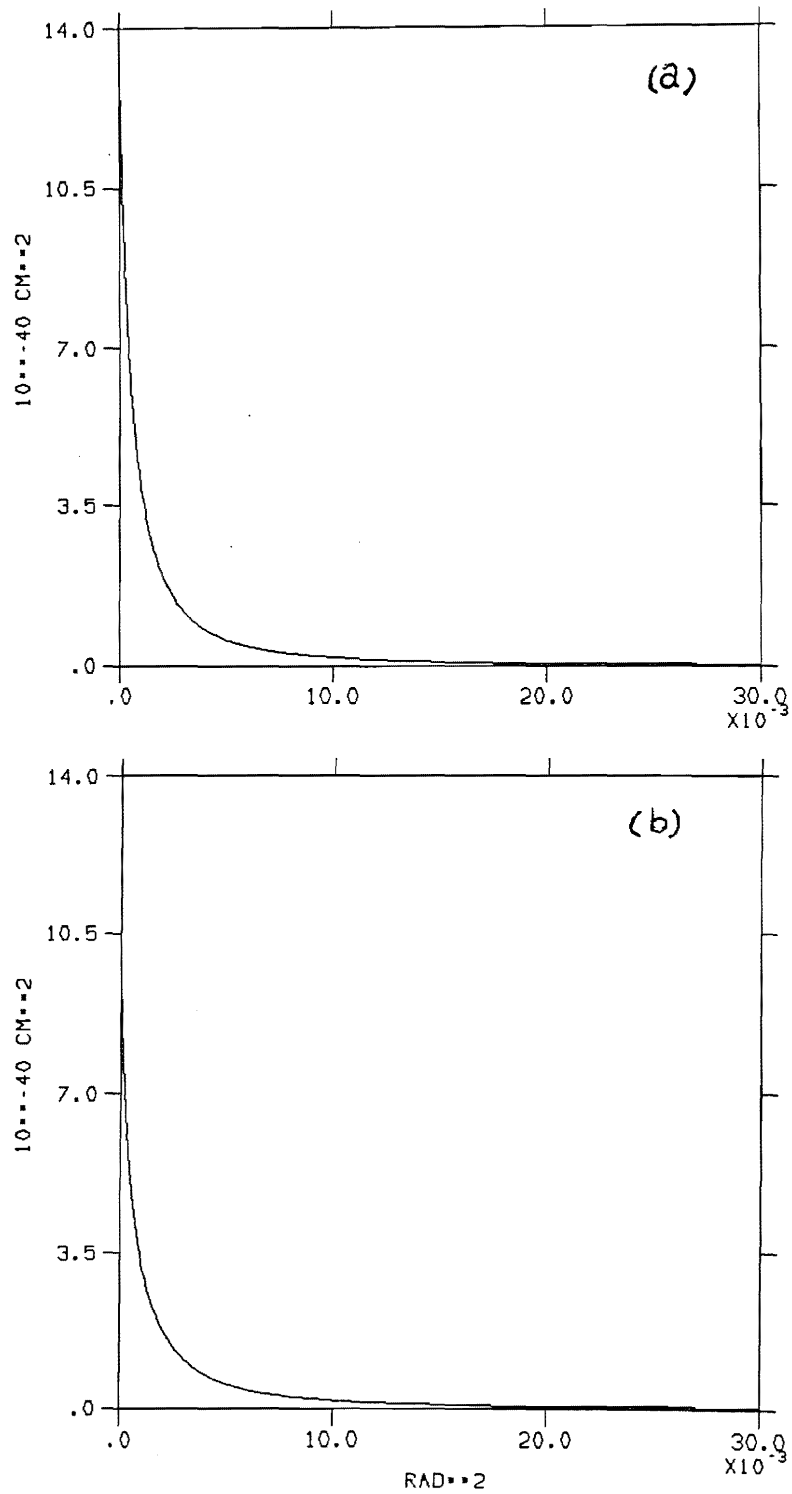

Figure 1.3.1 $\frac{d\sigma}{d\theta^2}$ for $\nu_\mu e \rightarrow \nu_\mu e$ scattering (a) and $\bar{\nu}_\mu e \rightarrow \bar{\nu}_\mu e$ (b) scattering. The energy of the muon neutrino (antineutrino) is set to 1.0 GeV, and $\sin^2\theta_w = 0.230$ for these plots.

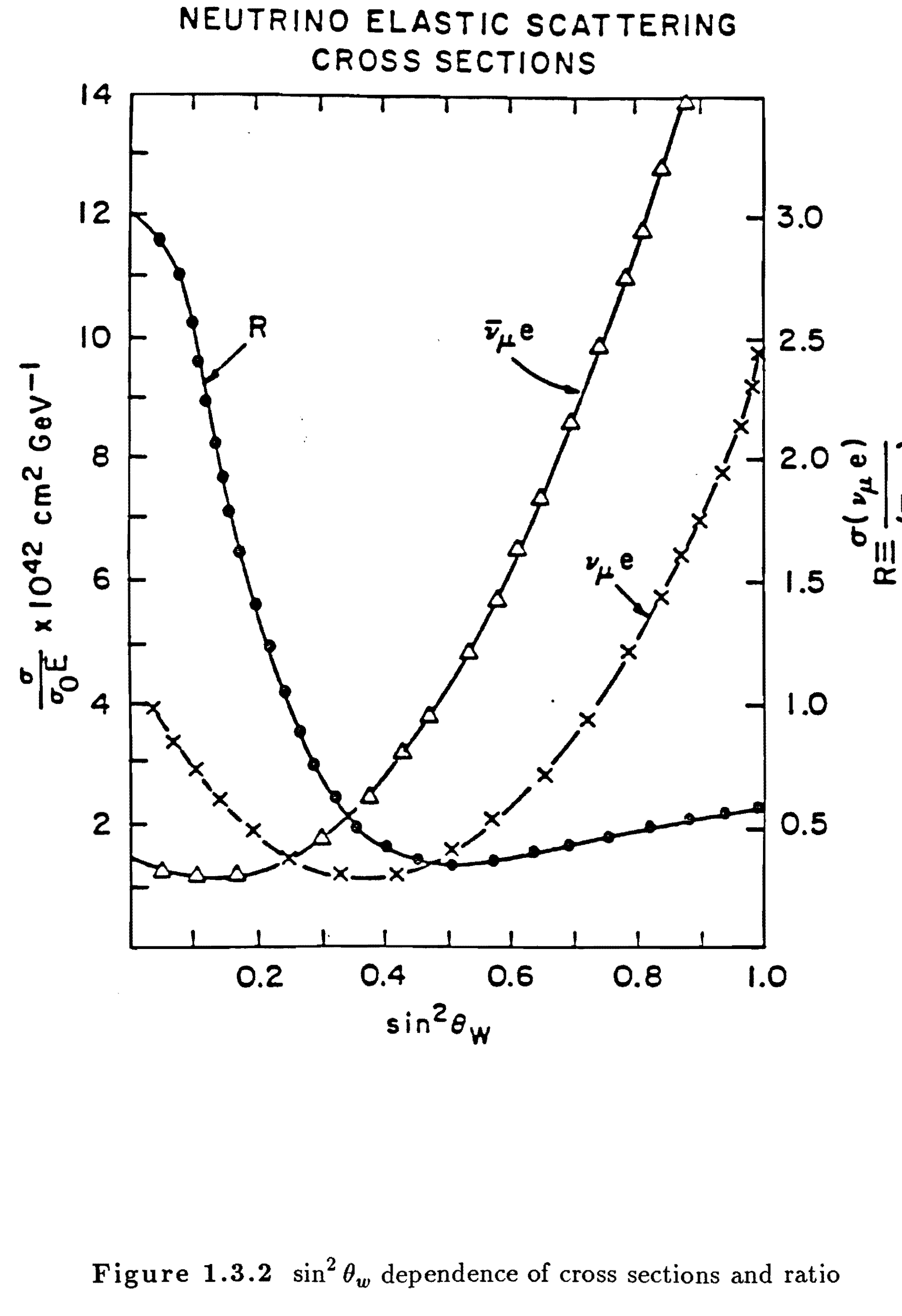

Figure 1.3.2 $\sin^2\theta_w$ dependence of cross sections and ratio

4. Experimental Goals:

The E-734 data on neutrino electron and antineutrino electron scattering were accumulated during three different periods. Three papers [10,11,12] were published about the analysis of data from the periods in 1981 and 1983. Analysis of data from the period in 1986 is the subject of this thesis. The analysis methods were improved in 1986 to reduce eyescanning of the data. With the additional data from 1986, we have improved the result on $\sin^2\theta_w$.

Maximum likelihood fits were made by combining data from the 1981, 1983 and 1986 runs. From these fits we get measurements of the total cross sections for $\nu_\mu e \to \nu_\mu e$ and $\bar{\nu}_\mu e \to \bar{\nu}_\mu e$ scattering. We get a measurement of the ratio R which gives us a determination of $\sin^2\theta_w$. Fits to the cross sections give an improved limit for the charge radius and magnetic dipole moment of the muon neutrino[9,10].

Chapter 2.

Experimental Apparatus.

1. The Neutrino Beam

The neutrinos/antineutrinos in this experiment were the products of decays of pions and kaons, [20] which were produced as secondary particles when a proton beam, accelerated to an energy of 28.3 GeV, was bombarded into a target. The proton beam was accelerated in 12 bunches in the Brookhaven AGS; it was extracted in a single revolution and steered towards a target as shown in Fig. 2.1.1. The beam spot was circular with a diameter of 2 mm. Each burst of protons had about 10^{13} protons in it. A count was kept of protons on target (P.O.T.) during the experimental run. The extraction process did not disturb the time structure of the proton beam as it arrived at the target. The secondary particles, with the same time structure, were allowed to decay in a long decay tunnel. The bunches were 224 ns apart, and the width of each bunch was 30 ns. The neutrino beam also kept the same time structure (Fig. 2.1.2), which was measured with neutrino interactions in our detector.

A titanium rod 6.4 mm in diameter, 45 cm long served as the target. It represented about 2 interaction lengths. Secondary particles of selected sign generated in the target were focused by a toroidal magnetic field produced by a system of horns. Horns were cylindrically symmetric current carrying devices. The magnetic field was produced by a large electric current that flowed on the surface. The horns, the shapes of which were optimized to collect particles of all possible momenta, produced a nearly parallel beam in the decay region. A schematic of the target-horns system is shown in Fig. 2.1.3(a). The whole assembly was cooled with water.

The energy-storage capacitors C, each $42\mu F$, were charged to $12kV$ in the $1.4sec$ between AGS pulses. When they discharged through ignitrons, they provided about $250kA$ of current for the horns. Firing of the ignitrons and the proton

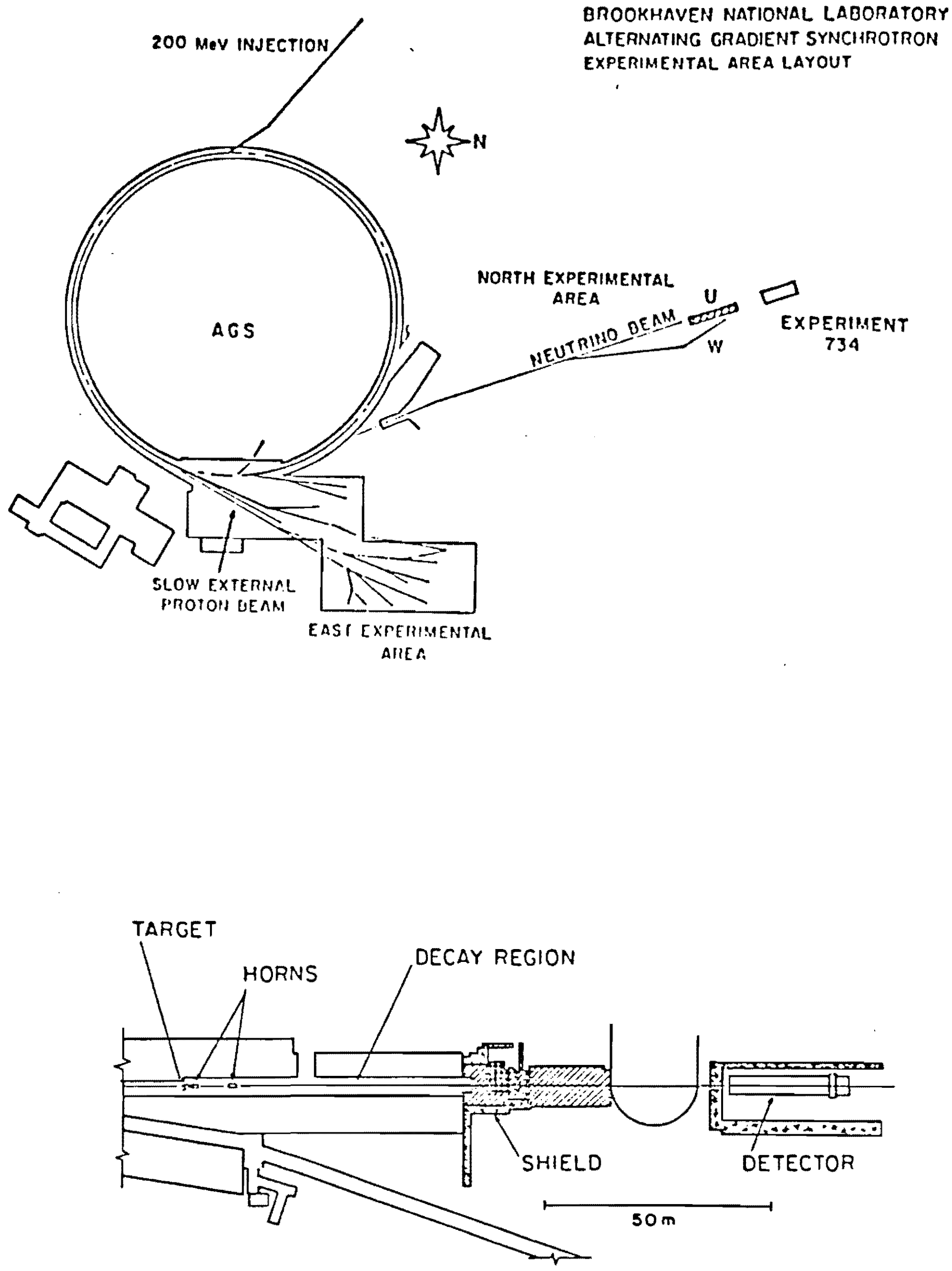

Figure 2.1.1 The wide band neutrino beam line at the BNL AGS.

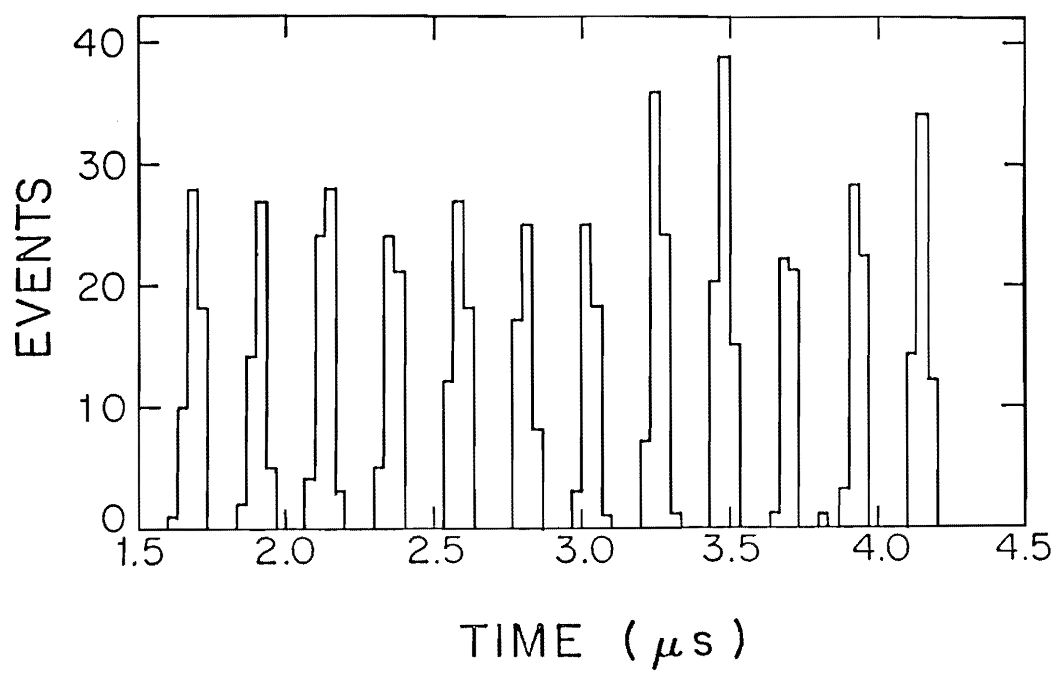

Figure 2.1.2 Time stucture of the neutrino beam as measured by the interactions in the detector.

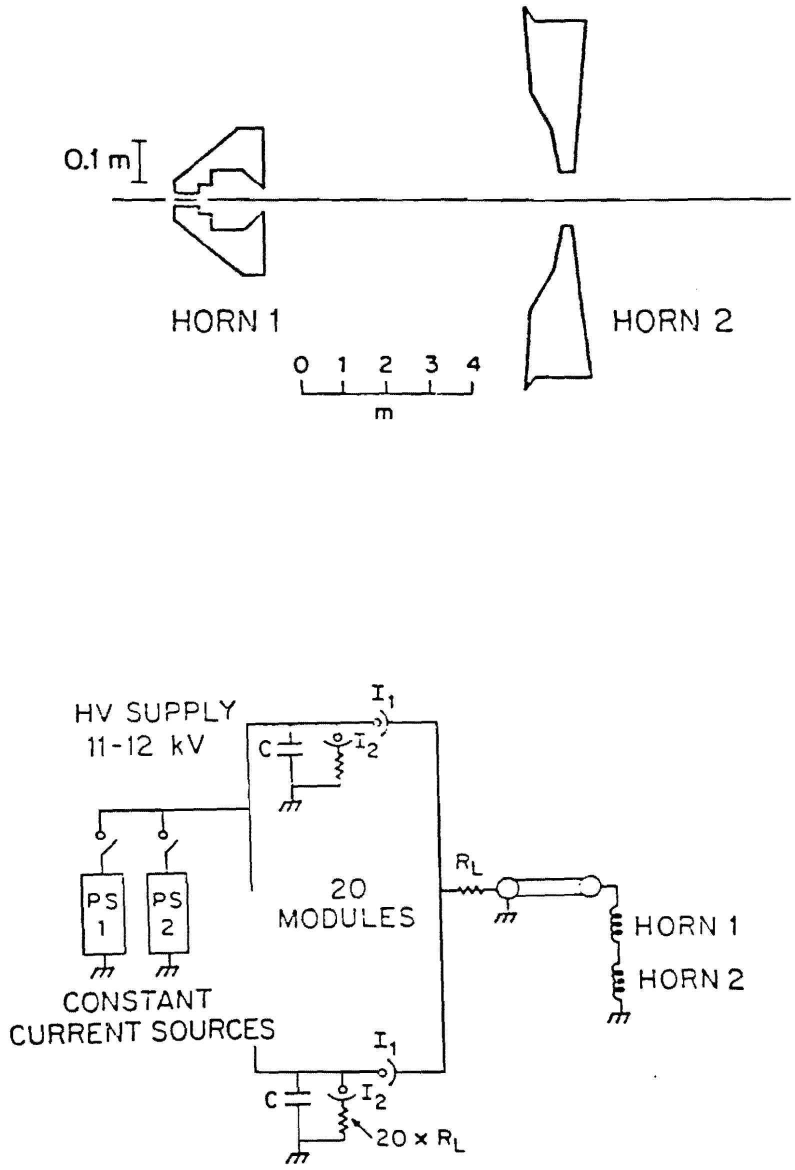

Figure 2.1.3 (a)The target horns system, (b)The horn power supply

beam extraction occured at the same time. After triggering, the horn current supply behaved as a series RLC circuit with a time constant of about $32\mu s$. After the current pulse decayed, the capacitors were charged up again. The time required to charge up the capacitor bank was monitored as a check on proper discharge of all the capacitor modules. Fig. 2.1.3(b) illustrates the power supply for the horns.

The target horns system, normally mounted so that the decay region was $62.0m$ long[18,19], was moved back $19.3m$ for the 1986 run because of some obstructions. Iron shielding, $25m$ thick, followed the $81.3m$ long decay tunnel. The shield stopped most muons and hadrons, accompanying the neutrino beam, from entering the detector. Ion chambers, mounted in the shielding, detected muons. They were used to monitor beam alignment and intensity by being moved vertically or horizontally.

2. The Spectrum

Decays of mesons that contribute to the neutrino beam are listed below in order of decreasing importance:

(1)$\pi \rightarrow \mu\nu_\mu$

(2)$K \rightarrow \mu\nu_\mu$

(3)$\mu \rightarrow e\nu_\mu\nu_e$

(4)$K \rightarrow \pi^0 e\nu_e$

(5)$K \rightarrow \pi^0 \mu\nu_\mu$

(6)$K^0{}_L \rightarrow \pi e\nu_e$

(7)$K^0{}_L \rightarrow \pi\mu\nu_\mu$

(8)$\pi \rightarrow e\nu_e$

At the target approximately twice as many positive pions and kaons were produced as negative pions and kaons, and so the total neutrino flux was twice as large as the total antineutrino flux. The predominant decay was $\pi \rightarrow \mu\nu_\mu$. For neutrinos close to the forward direction the kinematics of this reaction give:

$$E_\nu = \frac{{m_\pi}^2 - {m_\mu}^2}{{m_\pi}^2 + {p_\pi}^2{\theta_\nu}^2} p_\pi.$$

The formula shows that the neutrino energy decreases from $0.42p_\pi$ to $0.28p_\pi$ as θ increases from 0 to $33mrad$, the maximum angle of neutrinos in the detector. The neutrino spectrum from pion decay was a slightly broadened version of the pion spectrum transmitted by the horns with the energy scaled by a factor of about 0.35. The production rate of kaons was approximately 0.05 of pions. The kinematics for kaon decay (No. 2) are similar to pion decay, but kaons are heavier, and so neutrinos from kaon decay mainly contributed to the high energy end of the spectrum.

To obtain a predominantly neutrino (antineutrino) beam, the magnetic horn system was used to focus positive (negative) mesons while defocusing mesons of opposite charge. Some background processes (e.g. interactions in the materials downstream from the target) were less likely to suffer sign selection than direct production from the target. These processes caused a wrong helicity contamination in the primary beam. It was difficult to model these processes properly; therefore yields of muons of both signs for each horn polarity were measured by the spectrometer, described later.

Electron neutrinos (antineutrinos) were the other source of contamination present in the muon neutrino (antineutrino) beam. Electron neutrinos came from decays of kaons (No. 4 and 6 in above list) and decays of muons (No. 3). The muons were products of pion decays (No. 1). The contamination level was calculated by simulations of the beam to be approximately $7 \times 10^{-3} \frac{\nu_e}{\nu_\mu}$. The electron neutrinos (antineutrinos) interacted with nucleons in the detector and produced final state electrons (positrons) which were a source of background for the neutrino electron elastic scattering reaction. The cross section for electron neutrino quasielastic scattering is four orders of magnitude higher than the elastic neutrino electron scattering. Therefore understanding of the electron neutrino contamination was important.

The program NUBEAM was used for simulating the neutrino spectra of this experiment. For a complete description and further references see Ref. 20. The program incorporated particle properties, the beam geometry (e.g. magnetic field of the horns), interaction cross sections, and particle production rates to produce spectrum shapes which are presented below.

Neutrino (antineutrino) spectrum was measured by observing quasielastic interactions, $\nu_\mu n \rightarrow \mu^- p$ and $\bar{\nu}_\mu p \rightarrow \mu^+ n$, in the detector. Kinematics of this reaction relate the muon energy to the neutrino energy as follows:

$$E_\nu = \frac{m_N E_\mu - \frac{1}{2} {m^2}_\mu}{m_N - E_\mu + P_\mu \cos\theta_\mu}$$

$$P_\mu = \sqrt{{E^2}_\mu - {m^2}_\mu}$$

m_N is the nucleon mass (0.939 GeV), m_μ is the muon mass (0.106 GeV), E_μ is the observed total muon energy, θ_μ is the muon recoil angle with respect to the direction of the neutrino beam. To determine the neutrino spectrum, quasielastic events were selected and the total energy and direction of the muon was measured. The spectrum of neutrino energies, gotten from the above formula, was then corrected for cross section, backgrounds, and acceptance. Charged current single pion production was the main background for the quasielastic events which show up as single track or two track events in the detector. The background was estimated by Monte Carlo simulations.

Since two track events were available only in the ν_μ data sets, events with only a single long track were selected to treat both neutrino and antineutrino data equally. These events were classified in two ways: events in which the muon stops in the detector, and events in which the muon leaves the detector and traverses the muon spectrometer. The muon spectrometer is described in the next section.

The energy of stopping muons [20,21] was determined from their range in the detector. The range was required to be at least 20 modules (25 modules for antineutrinos) in order to eliminate hadronic background. The selection limited acceptance to neutrinos above 300 MeV, which was considered adequate because both flux and cross section were small below this energy. The upper energy limit, dictated by the size of the detector, was about 1.5 GeV. 2011 events from the 1986 neutrino data and 512 events from the 1986 antineutrino data were selected. Background levels were $(17 \pm 4)\%$ for neutrino data and $(18 \pm 4)\%$ from antineutrino data. The stopping muon data sets provided a check at low energies on the determination of the spectrum using the spectrometer.

Muons that traversed the muon spectrometer were analysed in a similar way. The muon energy was determined from the momentum measured in the magnet plus the calculated energy loss in the detector. The aperture and position of the magnet limited acceptance to neutrinos above 800MeV. Upper limit of 5GeV was chosen for good momentum resolution and correct determination of the muon charge. Totals of 5389 μ^- (4456 μ^+) and 179 μ^+ (591 μ^-) events were obtained for the 1986 neutrino (antineutrino) data. The contamination of antineutrinos in the neutrino beam was determined to be 0.043 ± 0.007, and the contamination of neutrinos in the antineutrino beam was determined to be 0.103 ± 0.015.

Quasielastic reactions, $\nu_e n \rightarrow ep$ and $\bar{\nu}_e p \rightarrow en$, were used to obtain the flux of the ν_e and $\bar{\nu}_e$. The method was similar to the one used in a previous paper (see Ref. 22). The sample of electromagnetic showers (selected by eyescanning) that eventually led to the set of events containing neutrino electron elastic scattering events also contained high energy ($> 1GeV$) showers that resulted from the final state electron(positron) in the quasielastic events (see chapter 4). To prevent scanning bias and to treat both neutrino and antineutrino data equally, the vertex energy was restricted to be less than $60MeV$, and since the elastic scattering signal was expected to be at low angles, the angle was restricted to be greater than $0.01rad^2$. 464 events from the neutrino data and 308 events from the antineutrino data were obtained. The background correction was calculated by using a sample of showers (stubs) that were clearly photons because they pointed back to other hits in the detector(see chapter 4). By assuming all showers below $1GeV$(except for a small correction due to $\nu_\mu e \rightarrow \nu_\mu e$ and $\bar{\nu}_\mu e \rightarrow \bar{\nu}_\mu e$) to be photons, background subtraction was done for showers above $1GeV$ using the shape of the energy distribution of the stub events. Thus the background fraction for neutrino (antineutrino) data was estimated to be 0.33 ± 0.05 (0.32 ± 0.05). Monte Carlo simulations of quasielastic ν_e and $\bar{\nu}_e$ events were used to estimate the acceptance for these events. Difficulties in modeling the final state neutron from the antineutrino reactions prohibited accurate determination of the $\bar{\nu}_e$ flux. Addition difficulties were presented by the neutron because for some events it deposited energy near the positron shower, and during scanning these events were rejected because they were considered electromagnetic showers associated with other interactions. The scanning efficiency for detecting a neutron could not be determined accurately. Therefore only upper and lower limits could be obtained for the flux of $\bar{\nu}_e$. The results were:

$$\frac{\nu_e}{\nu_\mu} = (7.3 \pm 1.4) \times 10^{-3}$$

$$2.8 \times 10^{-3} < \frac{\bar{\nu}_e}{\bar{\nu}_\mu} < 6.1 \times 10^{-3}$$

Results for the neutrino spectra are displayed in figures 2.2.1 ,2.2.2, 2.2.3, and 2.2.4 along with the NUBEAM calculations done for the neutrino (antineutrino) beam in 1982 (1983). Comparison of the 1986 results with the results from the 1982 and 1983 data sets showed no significant departure in the shape of the spectra. The total flux and contamination levels were, nevertheless, different, illustrating the need to measure contamination levels accurately for every neutrino experiment.

3. The E734 Detector

The detector has been extensively described elsewhere [13,26,25,16,17,18,19] and will be briefly reviewed here. The neutrino beam intensities (10^{10} ν_μ per AGS pulse), in conjunction with the small cross section for neutrino electron scattering ($10^{-42} cm^2$), demand a large mass detector to obtain useful event rates. The detector must provide many measurements of dE/dx along a track for particle identification. We also need excellent angular resolution for forward tracks. These considerations led to the size and the modular design of the E734 detector shown schematically in Fig. 2.3.1.

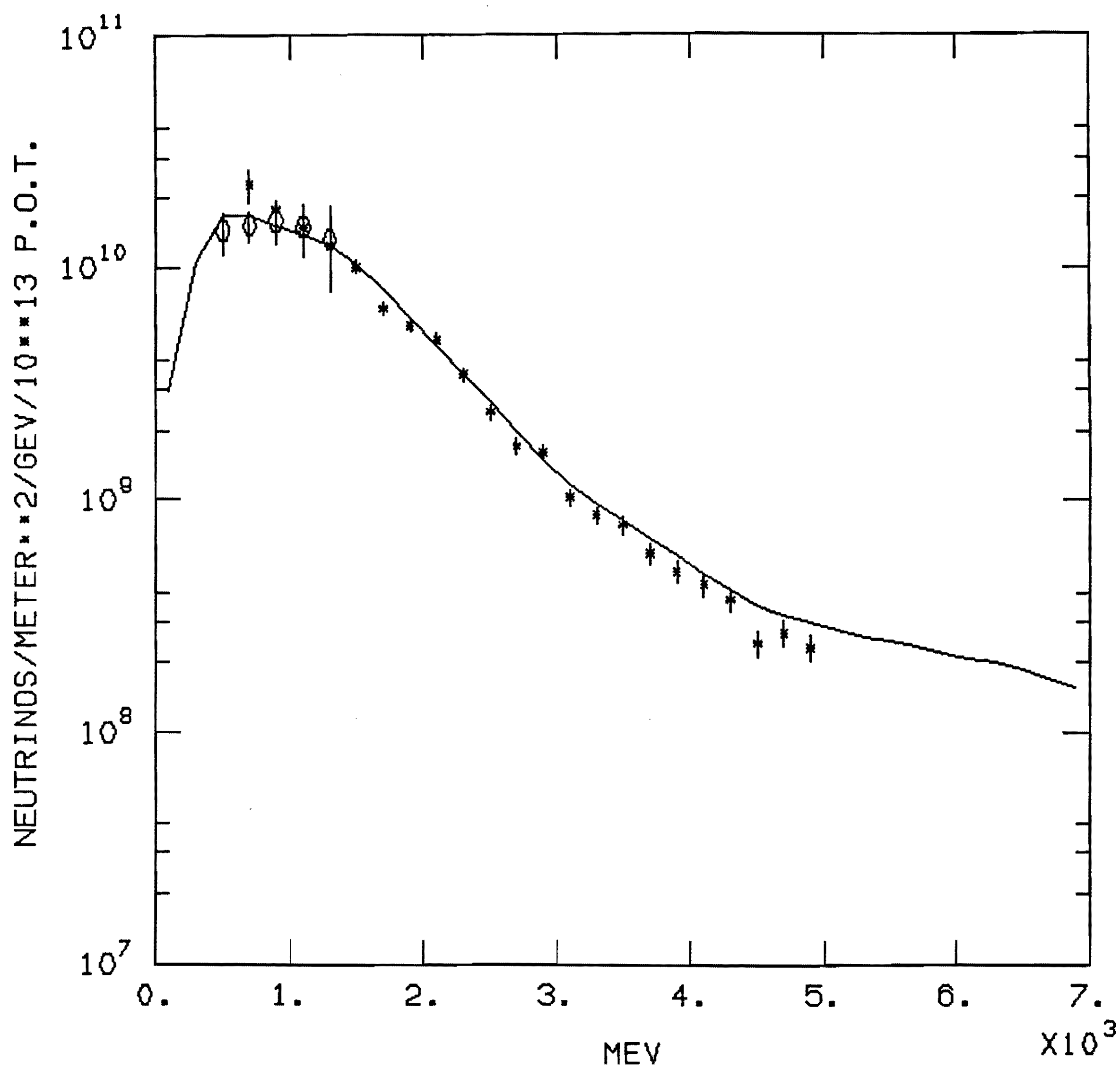

Figure 2.2.1 The ν_μ flux. The (*) are data from the magnetic spectrometer; the (0) are stopping muon data, and the curve is a NUBEAM calculation done for the neutrino beam in 1982. The curve has been scaled to correspond to the data.

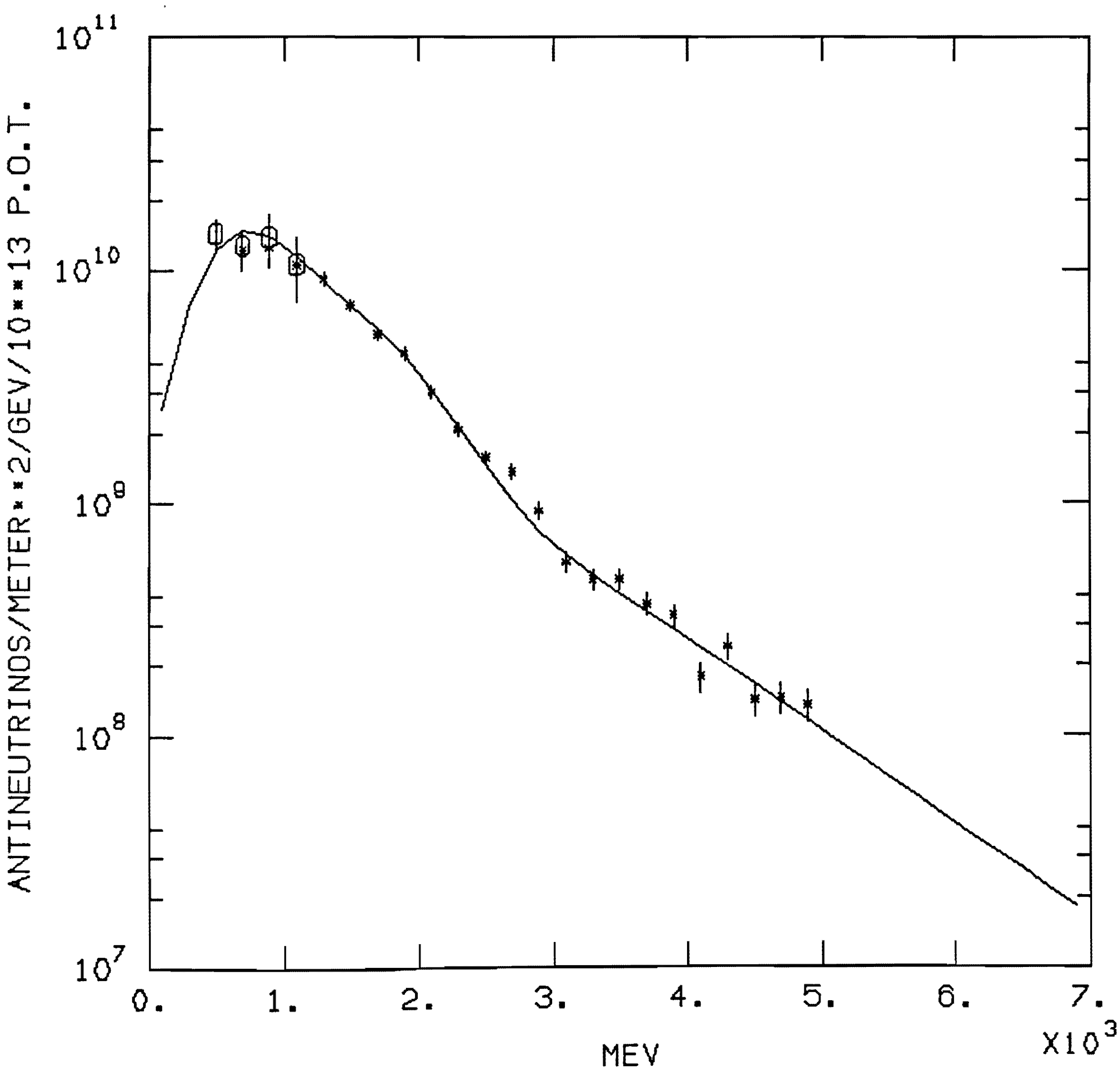

Figure 2.2.2 The $\bar{\nu}_\mu$ flux. The (*) are data from the magnetic spectrometer; the (0) are stopping muon data, and the curve is a NUBEAM calculation done for the antineutrino beam in 1983. The curve has been scaled to correspond to the data.

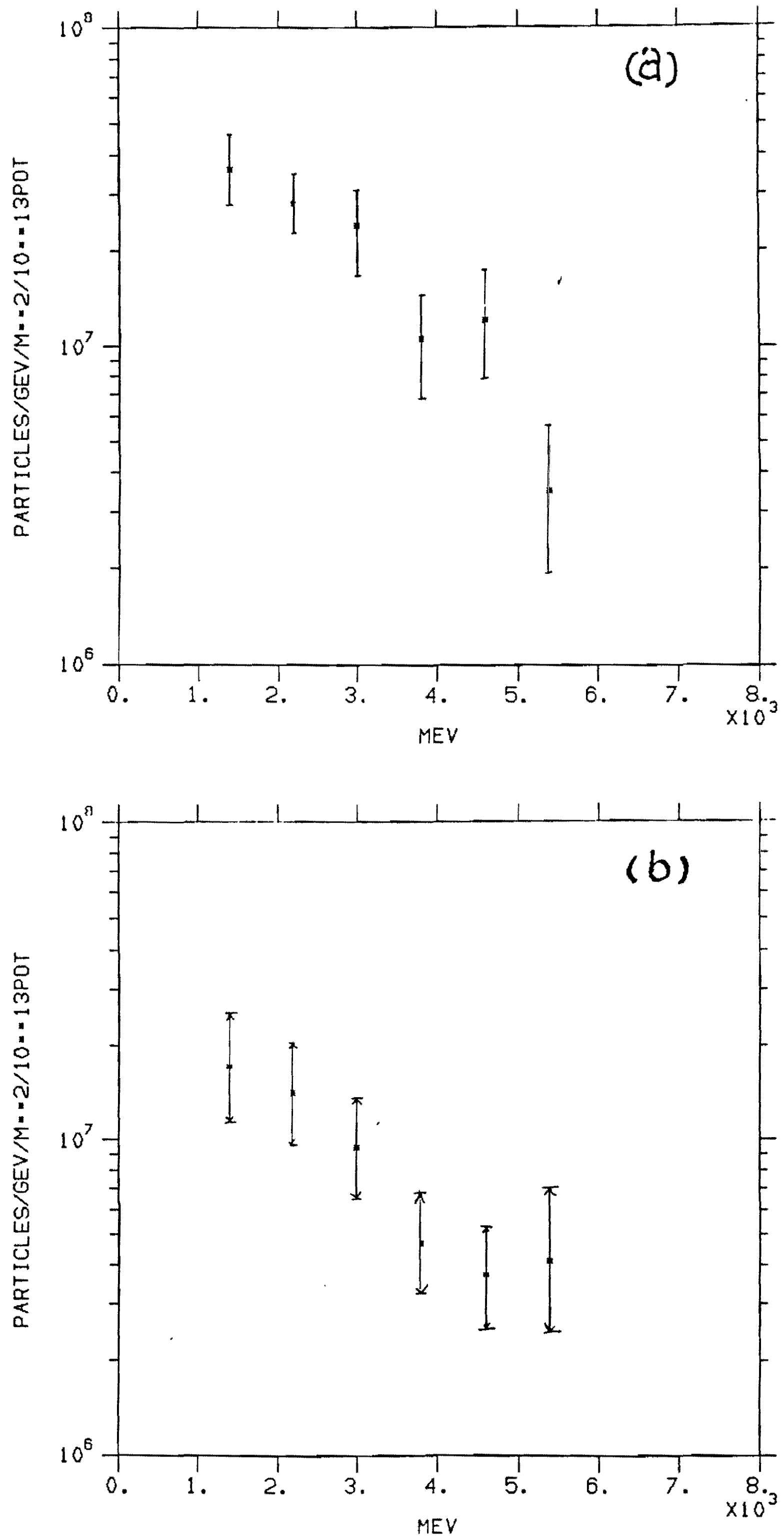

Figure 2.2.3 The ν_e(a) and $\bar{\nu}_e$(b) contamination.

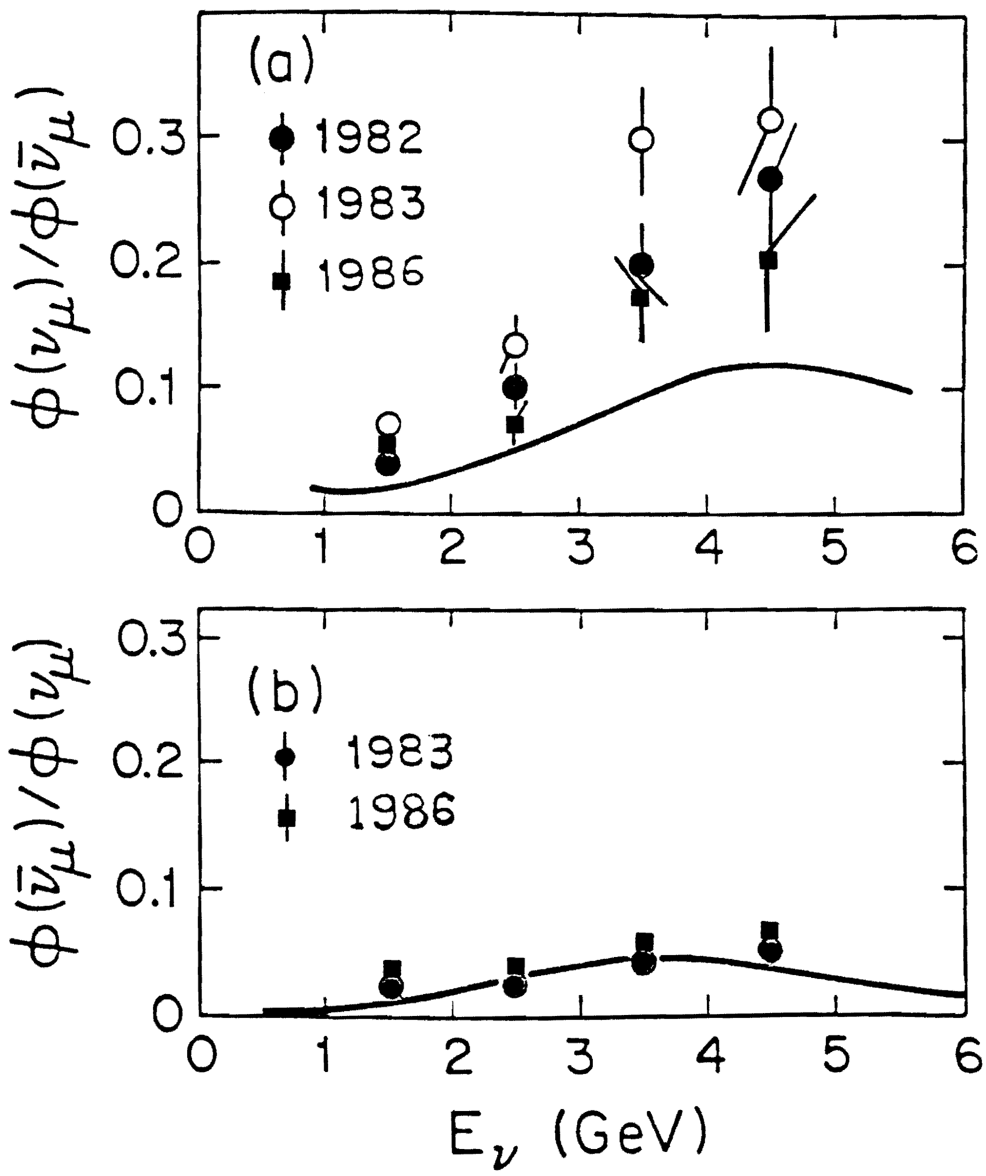

Figure 2.2.4 The contamination levels $\frac{\bar{\nu}_\mu}{\nu_\mu}$(a) and $\frac{\nu_\mu}{\bar{\nu}_\mu}$(b). The solid curves are NUBEAM calculations.

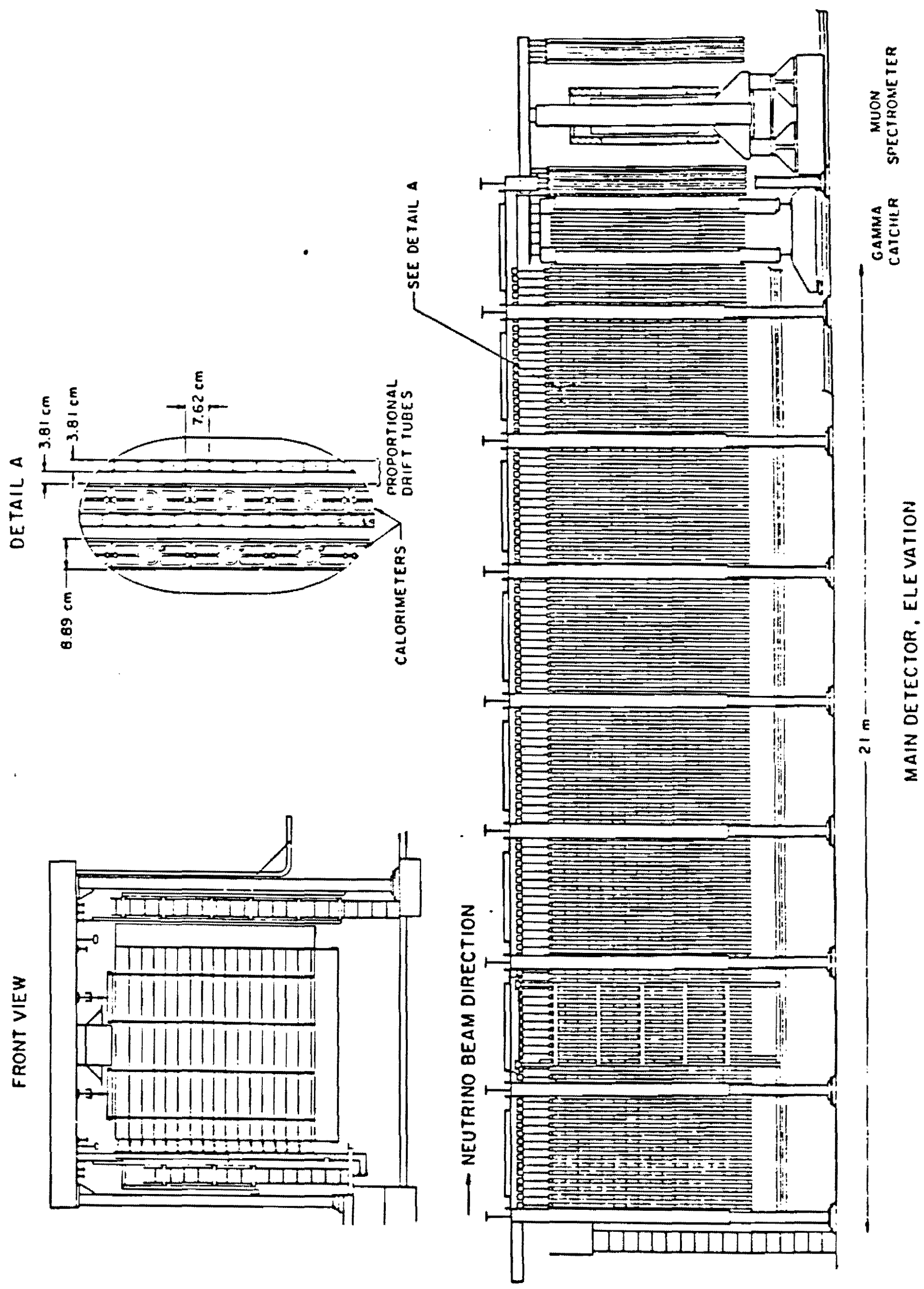

Figure 2.3.1 The E734 detector.

The detector had two major systems: The liquid scintillator calorimeter and the proportional drift tube system. The liquid scintillator served as a target for neutrinos and also as a detector with fine energy and time resolution. The proportional drift tubes (PDTs) were used for particle tracking and dE/dx measurements along the track. The main detector was divided in 112 modules. Each module contained a wall of liquid scintillator cells and an x-y proportional drift tube plane. Each module was $4m \times 4m$ in area and 0.22 radiation lengths in thickness. It had a mass of about 1.5 tons. As a charged particle traveled through the detector it crossed about 5 modules within one radiation length, permitting us multiple measurements of position and energy deposits along the track before multiple scattering or bremsstrahlung altered the original momentum of the track.

The total mass of the detector was 170 tons. The mass of the fiducial region was about 100 tons. About 90% of the mass was in liquid scintillator. After the main detector there was a shower detector. The gamma-catcher, as it was called, consisted of ten walls of liquid scintillator cells with a sheet of lead after each wall. Each sheet of lead was one radiation length thick. There were no PDTs in the gamma-catcher. Ten radiation lengths were considered sufficient to contain electromagnetic showers that originated at the end of the main detector.

At the very end of the detector there was a magnetic spectrometer [20] to measure the momentum of muons produced in the main detector. It used an air gap magnet with an aperture of $1.8m \times 1.8m \times 0.46m$. To a charged particle traversing the magnet, the magnetic field imparted transverse momentum of $40MeV/c$ at the center and $70MeV/c$ at the edge. Nine pairs of PDT planes, four before the magnet and five after, served to measure the bend of a particle track, which was fit to a parabola. The start time for the drift measurements was generated from the last six calorimeter walls in the main detector. The momentum of the particle was calculated by using the appropriate field integral and the bend angle. Uncertainties in the PDT positions, about $1.3mm$, limited the momentum resolution, described below:

$$\frac{\delta p}{p} = \sqrt{[0.010 + (0.067p/(GeV/c))^2]}.$$

The detector was at the end of the neutrino beam line at the Brookhaven AGS, 147.8 meters downstream from the target. The center of the neutrino beam passed about 30 cm away from the center of the side facing the beam. The main part of the detector was 21 meters long and $4.2m \times 4.2m$ in cross section.

Item	Density $moles/cm^2/mod$
Carbon	0.471
Hydrogen	0.832
Oxygen	0.021
Aluminum	0.032
Protons	4.241
Neutrons	3.441
Electrons	4.241

Table 2.3.1 Chemical makeup of the detector

Liquid scintillator NE235A mixed with mineral oil (40% by weight) was used in the liquid scintillator cells. It mainly contained long chains of hydrocarbons, described by the formula CH_2 [16]. Table 2.3.1 shows the chemical makeup of the detector after taking account of the mass in the acrylic walls of the scintillator cells and the aluminium walls of the PDTs.

A typical data accumulation cycle began when a burst of protons, $2.7\mu s$ wide and with the bunch structure described earlier, hit the target. The repetition rate of bursts of 28.3 GeV protons from the AGS was 1.4 sec. About 1.5 ν_μ induced events occured in the detector. A $10\mu s$ gate, opened at the same time as the proton beam extraction, enabled all detector elements to record data. The electronics associated with each detector element, a PMT or a PDT, was able to record total energy deposition in that element and at least two pulse times. After the end of the $10\mu s$ gate the data was read out and recorded on magnetic tape by computers. The entire process taking no more than $50ms$, there was ample time to perform monitoring and calibration procedures between beam bursts.

4. The Calorimeter System

As shown in Fig. 2.4.1 each module had sixteen horizontal calorimeter cells (each cell $25cm$ high, $8cm$ along the beam, and $4m$ long) mounted one above the other with a photomultiplier tube at each end. Total internal reflection at the outside surface helped guide the light, generated by the liquid scintillator in the cells, to the photo-tubes.

An individual cell was made from an extruded rectangular acrylic tube with $2.5mm$ wall thickness. End caps were made from injection molded black acrylic silvered on the inside face, and fitted with windows for a PMT and an optical fiber. End caps were glued to the extrusions with acrylic cement. Care was taken to prevent stress and fine cracks in glue and the walls of the extrusions. A black plastic sleeve made the cell light-tight. The cells were individually supported and hung in a plane by four equally spaced steel straps. Each cell could be filled and drained independently. The cells were mounted at a slight angle which ensured that the small included bubble remained at one end of the cell and did not affect light transmission along the cell. After the cells were filled, they did not require attention for many years until the end of the experiment.

The PMTs fitted on each end of a calorimeter cell were $2in$ diameter twelve stage Amperex 2212A. The manufacturer fitted each of them with a resistor chain on a printed circuit board. The cathode of the tube was grounded. A DC current of about $0.3mA$ persisted through the divider chain. An NaI scintillator and a standard source (^{241}Am) were used to calibrate the gain. The gains of all the tubes were equalized to within 5% by the choice of a resistor between the high voltage supply and the divider chain. Uniform gains enabled us to operate all 3904 PMTs at the same high voltage, 2150 V, using twenty-four supplies. The signal

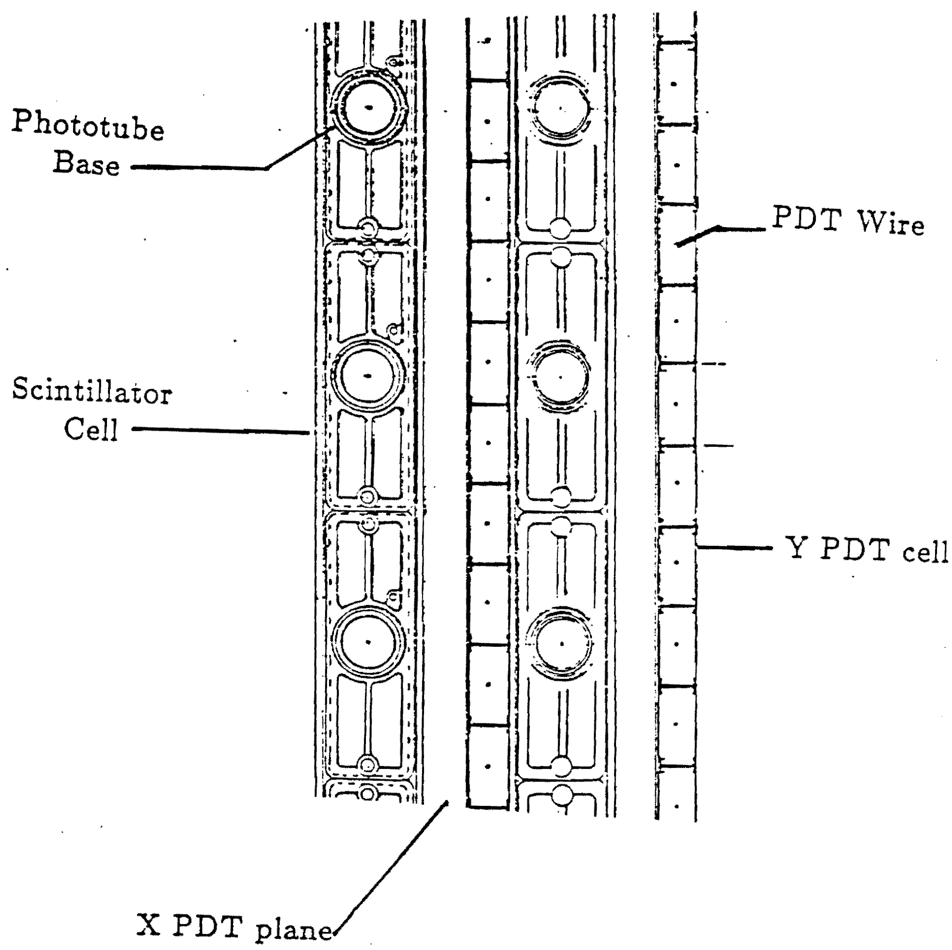

Figure 2.4.1 A module in the detector.

ground and the PMT ground were isolated from each other by a $10k\Omega$ resistor. An RG62/U cable transported signals from the PMT to the detector electronics.

The anode pulses from a PMT during data collection were about $50ns$ long and contained an integrated charge between 2 and 400 picocoulombs. The charge and time of arrival of a pulse were stored by the signal processing electronics for readout after the $10\mu s$ data collection cycle. The left and right signals from four scintillator cells were processed in one group. The analog processing for the eight inputs was done on one board (the Q board), and the timing information was processed on another (the T board). Eight pairs of these boards were housed in a crate. The boards plugged into the backplane of the crate. There was a control board in each of the crates. Control and readout busses carried the data from a crate through the control board. The control board was also used to form logical combinations of signals to trigger readout cycles for cosmic ray data.

A signal from a photo-tube went to an integrator and a discriminator. The threshold for the discriminator was set from a computer through a DAC. It was set to correspond to 0.1 milliamperes. The discriminated signal went on to the T-card for timing purposes. It also enabled the readout of the integrate and hold circuit. A signal over threshold in either the left or right photo-tube of a calorimeter enabled the readout of charge integrators on both channels. The integrator accumulated charge for one microsecond and held it on a capacitor. If, within a single data accumulation cycle, a train of several pulses came from a photo-tube, a single charge was recorded for each of the left and right channels, but several times were recorded. Fig. 2.4.2(a) shows the signal processing electronics for a pair of left right channels of a calorimeter cell.

The Q-board sent ECL pulses about $125ns$ to $175ns$ long to the T-board. The timing was done with a hybrid digital-analog system. A pulse between two clock pulses started the discharge of a capacitor and caused the value of a 25 MHz 12 bit scaler to be stored in a memory. The capacitor discharged until the next clock pulse. The voltage on the discharged capacitor interpolated the time between pulses. Each channel had two independent interpolation circuits for two

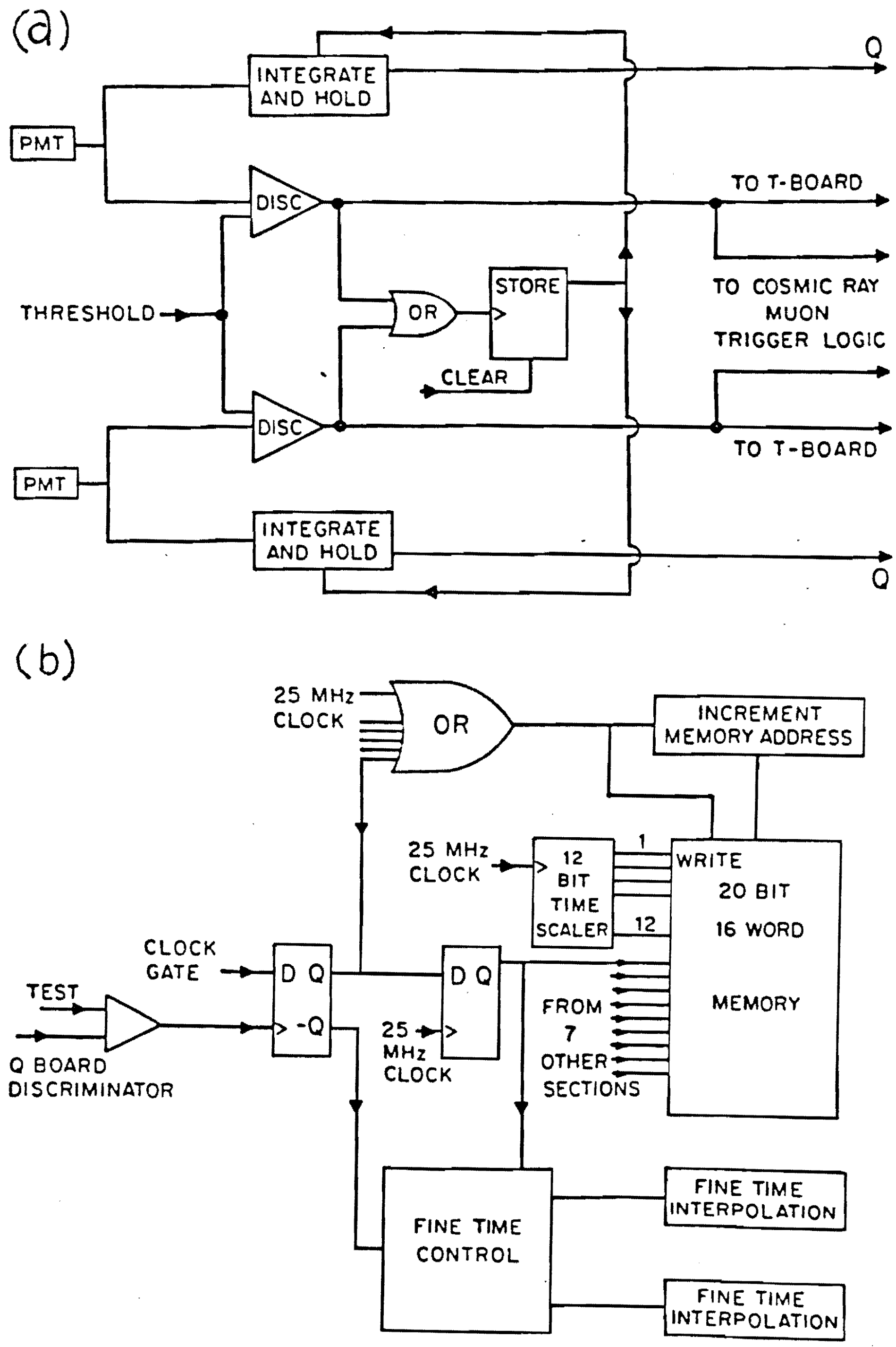

Figure 2.4.2 (a) Signal processing for a single calorimeter cell on the Q-card. (b) Time measurement on the T-card

pulses. Fig. 2.4.2(b) shows the circuit on the T-board used for measuring the time of arrival of a signal within a nanosecond.

The 25 MHz clock was derived from a precise 100 MHz oscillator. On each T-card there was a memory with 16 words, each 20 bits long. A word contained the scaler contents in the first 12 bits and the bit pattern of the eight inputs in the last 8 bits. After the data collection cycle, all time information about the pulses received by the T-card was in the 16 word memory and the two interpolation circuits for each of the eight channels. During readout of the data the analog information (fine time) was digitized in units of approximately a nanosecond. By combining information from the fine time circuit and the clock scaler, we were able to determine the time to within a nanosecond for two pulses from each of the photo-tubes in the detector.

5. *The PDT System*

Each detector module contained x and y PDT planes. Sheets of aluminium ($0.5mm \times 4m \times 0.6m$) were placed edge to edge to form a single sheet ($4m \times 4.2m$). "I beams " made from $0.5mm$ thick aluminium were glued $76mm$ apart onto these sheets. Injection molded end caps were glued to the ends of 54 cells in each plane. A stainless steel wire 75 microns in diameter was threaded through the end caps. Grooved pins held the wire within 50 microns of the center of the cell with a tension of about 4.4 newtons. A plane was completed by placing aluminium sheets above to form the other surface. Thick ($3.8cm$) box beams were glued along two edges of the plane to give strength to the plane and support for the electronics mounted along one edge. Each plane was checked for gas leaks and filled with P-10 gas (90% Ar, 10% Methane). A ^{109}Cd source was used to measure and eliminate fluctuations in gain greater than 10% over the entire surface of the plane. Fig. 2.5.1 is a schematic of a PDT plane.

An x-y pair of planes was supported from above by electrically insulated bars. Alternate chamber pairs were offset by one half cell to resolve tracking ambiguities. Commercially available P-10 gas was circulated through a closed

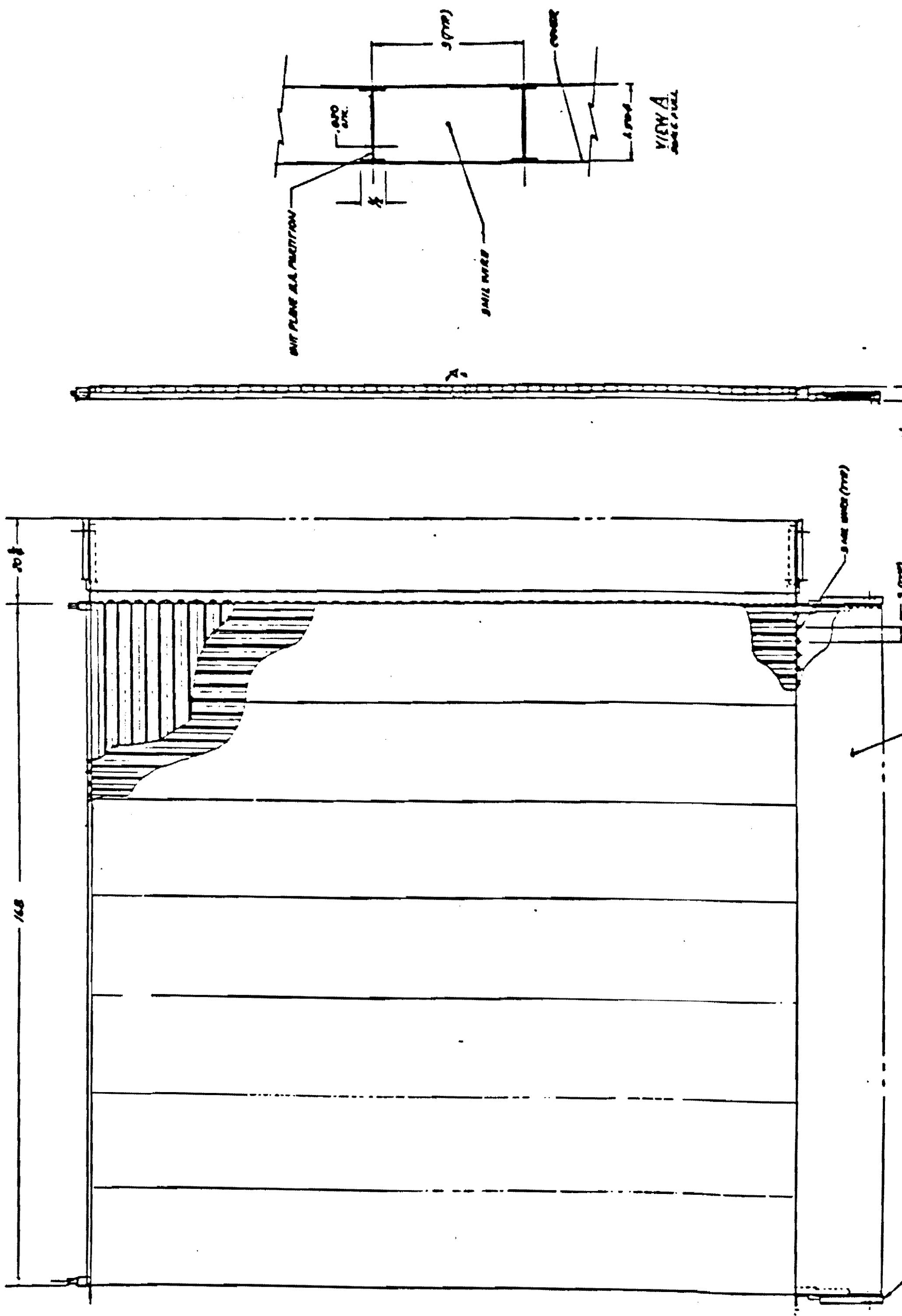

Figure 2.5.1 Schematic of an x-y PDT plane pair.

system that cleaned all the gas every 48 hours. By removing water vapor and replacing some of the gas, oxygen contamination, which can cause loss of ionization electrons, was kept low.

The PDT electronics was mounted on the PDT planes. Eight channels were processed together on two boards, one for analog processing (A) and the other for digital processing (D). A long printed circuit card was attached tranverse to the anode wires. It distributed high voltage and calibration pulses to the wires, and brought signals from the wires to the A board.

It was designed to measure two pulse times and one integrated charge in much the same way as the calorimeter electronics. The signal from a wire was AC coupled to a preamplifier. The preamplifier produced two signals, one of which was differentiated and sent to the D board where a discriminator determined if the PDT was hit. If the discriminator detected a signal above threshold, it triggered one of two $100MHz$ clocks which counted until the end of the master gate. A dead time of $800 - 1200ns$ was enforced to prevent double hits from a single long pulse. The second output from the preamplifier went to a charge integrator through another amplifier and a gate switch, S, which was closed during the master gate to collect all the charge deposited in the PDT. The time counters and the charge integrator held their data until it was read by the data aquisition system. The PDT were used in the proportional mode, so the integrated charge was proportional to the amount of energy deposited in the PDT. Time was measured for maximum of two pulses in unit of $10ns$, corresponding to $0.4mm$ of drift distance. The electronics for one channel is illustrated in Fig. 2.5.2.

6. Data Aquisition and Control

The operation of the detector required control, monitoring and calibration of 3904 PMT, 13068 PDT channels, as well as associated power supplies and test pulsers. Accelerator and beam information was also processed[13]. The data aquisition system (Fig. 2.6.1) consisted of custom built scanners, LSI-11 microprocessors, a PDP 11-73 computer, and a remote analysis computer (VAX8600). The system

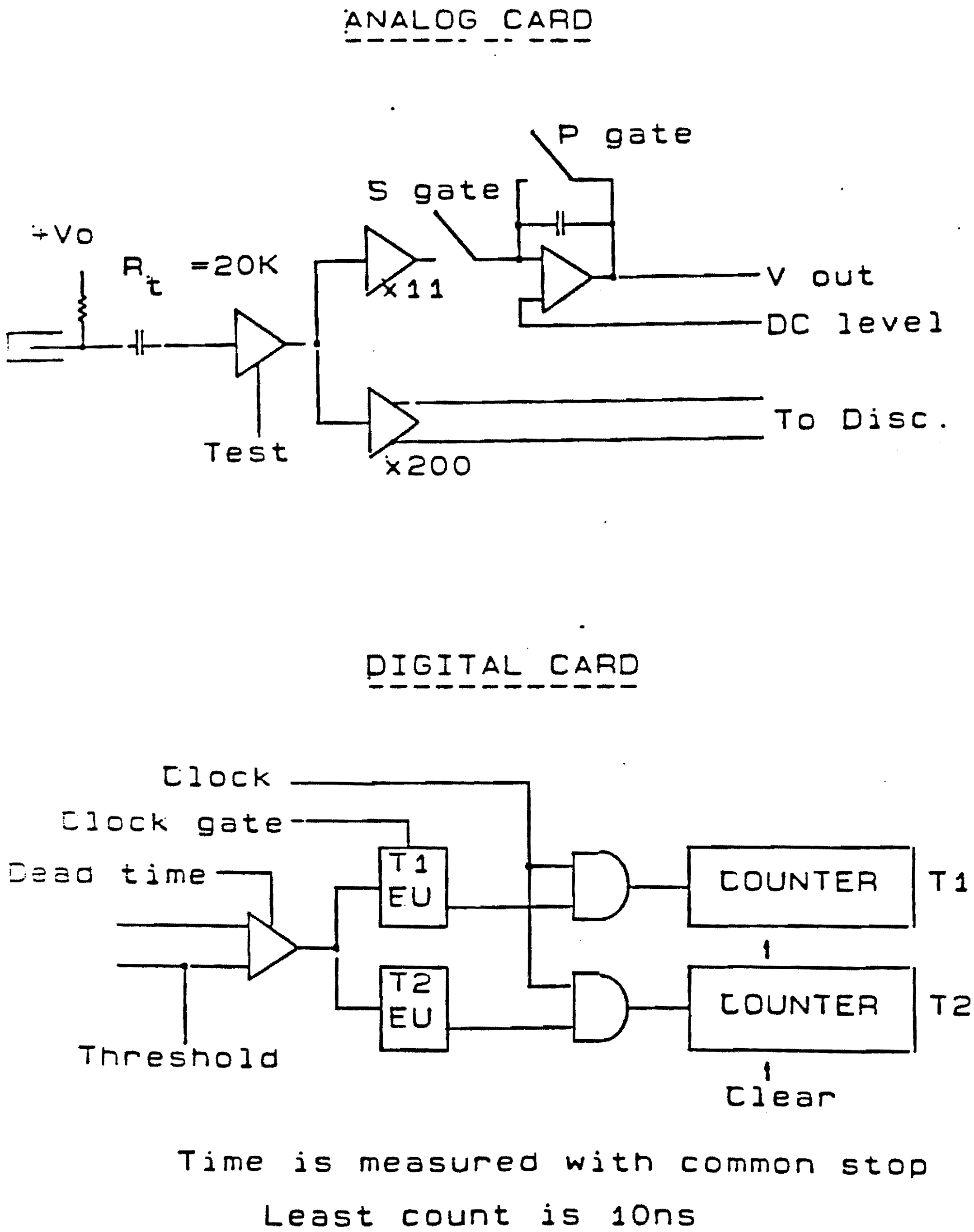

Figure 2.5.2 The PDT electronics

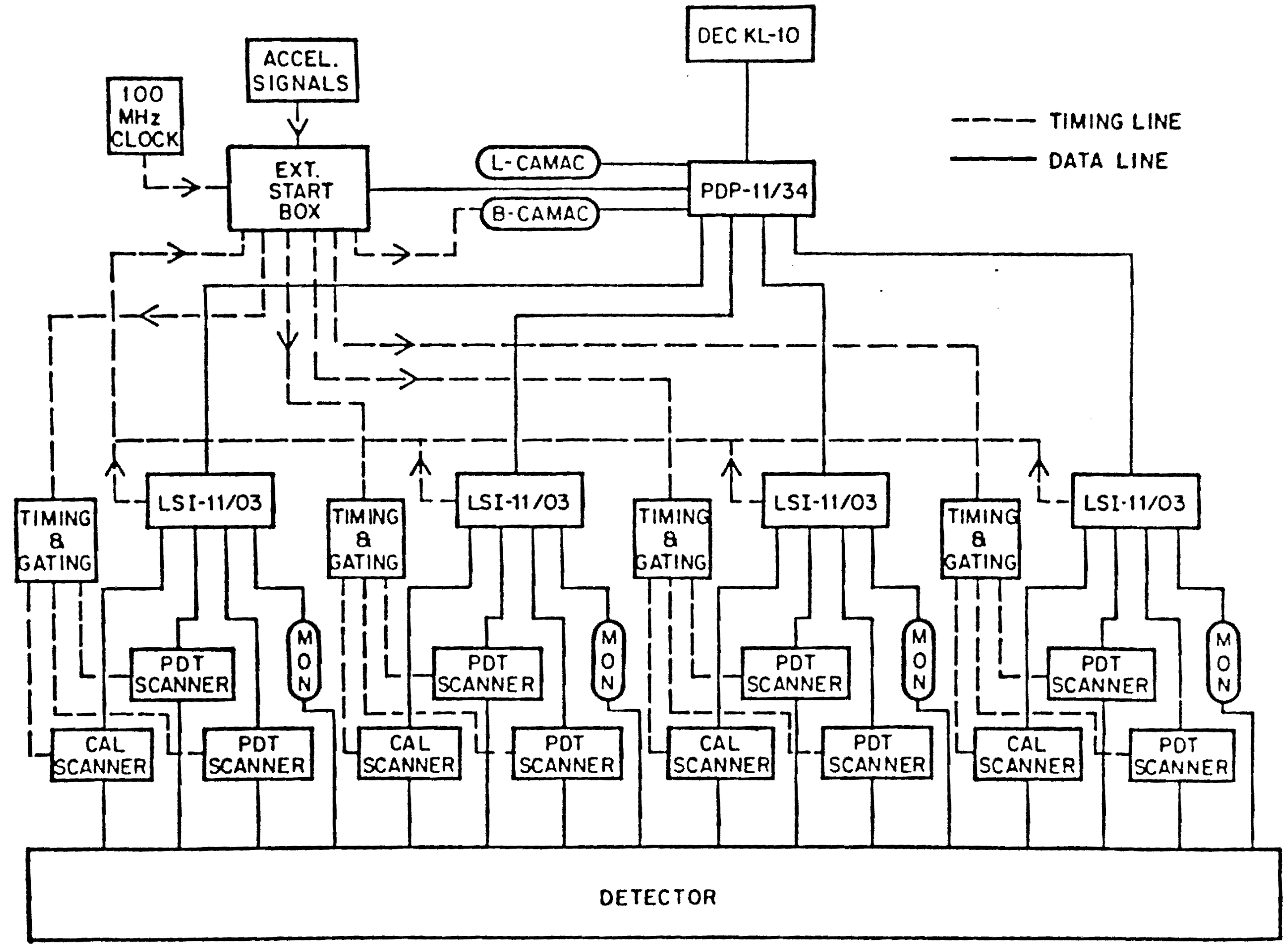

Figure 2.6.1 The data aquisition system for E734

used in 1986 was an improvement over an older system. In 1986, older LSI-11/03 microprocessors were replaced by LSI-11/23 microprocessors. The PDP 11-73 and the VAX8600 were also improvements over the older PDP 11-34 and KL10. The changes afforded a gain in speed for all tasks.

The LSI-11 microprocessors ran asynchronously with interrupts to announce completion of tasks. Overall synchronization of data digitization was required because portions of a single event usually originated in different microprocessors. A coincidence unit, the external start box, (ESB), accomplished the synchronization to about a nanosecond. It accepted ready signals from the microprocessors, and timing signals from both the accelerator and the $100MHz$ master clock of the experiment. It then transmitted synchronized signals to the timing and gating circuits of the microprocessors.

Data collected by the front end electronics were read out, mapped, and digitized by specially designed PDT and calorimeter scanners. A PDT scanner controlled 16 pairs of x-y-planes including readout logic, a pulser system, and majority logic for triggering on cosmic ray muons. A calorimeter scanner controlled 32 calorimeter planes, readout logic, majority logic for cosmic ray muons, and trigger logic for cosmic ray muons that traversed planes associated with more than one scanner. Scanners collected data asynchronously at the end of the $10\mu s$ beam gate. A DMA link connected each scanner with an LSI-11 microprocessor.

The detector was divided into 4 independent sections (3 sections of 32 modules and 1 section of 16 modules of the main detector, the gamma catcher, and the magnetic spectrometer). Each section was controlled by an independent LSI-11/23 microprocessor. Data flowed into each microprocessor via separate DR11-B DMA links associated with its two PDT scanners and one calorimeter scanner. After reformatting in the microprocessor data were transferred using a DA11-B01 link between the microprocessor and the PDP-11/73, the central control computer of the experiment.

The PDP-11/73 was connected to the four LSI 11/23 microprocessors and to a remote analysis computer (VAX8600) through a high speed serial link. Two CAMAC crates attached to the PDP 11/73 read out accelerator information and parameters of the light pulser calibration unit. The operator defined running conditions and enabled data collection from the detector with the help of the 11/73 program, MULCH, which was based on the Fermilab RT version of MULTI[23] and included major additions to the data acquisition and analysis areas appropriate to managing the data collection[24], and also to graphics (based on MATROX video boards) and transfer routines (for the link to the VAX8600).

Through MULCH the operator was able to change interactively contents of registers that controlled data acquisition in the scanners; particular modes of operation were defined and enabled through MULCH. The register-driven scanner design proved very powerful, and made possible elaborate automated calibration procedures.

In response to a trigger, the scanners associated with each microprocessor independently addressed and digitized the detector electronics for each one quarter of the detector. These data were read into the 11/23 where they were reformatted and assembled with appropriate headers. After this processing the 11/73 was interrupted with the request that it receive data. The data acquisition system in MULCH recognized six interrupts: the data sources represented by 4 micros, 1 CAMAC crate for beam data, and 1 CAMAC crate for a light pulser calibration system. An event consisting of blocks of data from one or more of these sources was packaged in the 11/73. Beam events usually were combined from 4 micros and the beam CAMAC, received in any order, built into the same record with an overall header and pointers to individual data blocks. Once collected, complete events could be selectively dispatched to tape, to the remote analysis computer, and to monitor and display routines in MULCH.

7. *Maintainance*

The E734 detector has over 15000 detecting elements. Continuous effort was required to maintain this complex system during the data collection periods.

Except for periodically replacing some photomultipliers and gas containers, the calorimeters and the PDTs required no maintainance. The calorimeter electronics, however, proved to be fragile; it had to be watched over very carefully. The PDT electronics also required much attention. Problems in the detector were routinely found during monitoring and calibration tasks. Dirty contacts between the printed circuit boards and the back-planes were the cause of most malfunctions. If cleaning the contacts sometimes did not solve a problem, the board was sent to a testing station that simulated all signals on the board and found bad circuit elements. The calorimeter electronics crates were provided with power through the back-plane. The power supplies were operated near their full capacity. The power supplies failed often and had to be replaced. Effects of floating grounds, unstable power supplies and fast, small ECL signals combined to cause problems that required much time and skill to solve.

Finally, spark chambers from another newly installed experiment behind E734 induced spurious signals in the PDT electronics. A copper mesh was spread over the back wall to act as a shield against the electromagnetic radiation emmitted by the spark chambers. Even with the shielding, there were some bad hits in the spectrometer whenever the spark chambers were triggered. The bad hits were not syncronous with real data, and thus did not cause difficulty in analysis.

8. *Monitoring and Calibrations*

Many routine tasks that had to be performed while operating the detector, were automatically performed by a monitor system that had sensors to check voltages, currents and temperatures in the major detector components. Each microprocessor read the sensors in its part of the detector between beam spills with a 64 channel multiplexed ADC. The system checked the values of these quantities against a table, and if a quantity was found out of tolerance, the operator was alerted. The monitor system reliably detected obvious problems such as tripped high voltage supplies and lack of cooling for the electronics.

Four calibration tasks were performed routinely during data-taking: (1) PDT cell timing using an electronic pulser, (2) calorimeter cell timing and pedestals using a light pulser, (3) almost horizontal cosmic ray muons for monitoring overall performance, and (4) vertical cosmic ray muons for determining light attenuation constants for energy measurements in the calorimeters.

Electronic pulses of varying amplitudes and time were sent to the inputs of the PDT electronics to test their performance. The PDT pulser was operated in three different modes. In the first mode two pulses of known times and amplitudes were fed to the PDT electronics. The times and amplitudes determined by the electronics were then compared with the known values. In the second mode a pulse of small amplitude was used to trigger the readout electronics. This mode determined the charge pedestal because the pulse was small enough not to contribute anything to the charge integration. In the third mode pulses of varying amplitude were fed, and a functional relationship between pulse height and charge integration was determined. Extrapolation of the function to zero yielded another value for the charge pedestal.

Four separate spark gaps inside light tight boxes, one for each quarter of the detector, generated light pulses for the calorimeters. Fiber optic cables, one for each PMT, carried the light from a spark to the calorimeters. A vacuum photodiode, viewing the spark directly, defined the starting time of the spark, and three PMT standards, viewing the spark through fiber optic cables of the same length, defined the amplitude of the flash of light viewed by the calorimeters. Three filters were used to vary the amplitude of the light signal. There were four modes of calorimeter calibrations. In the first mode the firing time of the PMT and the vacuum photodiode were subtracted to get the time pedestal for each PMT. In the second mode one of the filter settings was used; values obtained for integrated charge were compared with standard values from previous studies. In the third mode three different filter settings were used to test the linearity of the charge integration. In the fourth mode high voltage for PMTs on one side of the detector was turned off, and light pulser data was collected. The charge read from the electronics of the disabled PMT was its charge pedestal. The PMT that was not turned off provided the trigger for charge integration of both PMTs in a calorimeter.

A trigger was generated in the calorimeter scanner when a cosmic ray traversed a given number of planes. These nearly horizontal cosmic rays were used to determine plane and element efficiencies. The remote analysis computer made fits to a cosmic ray track, and calculated the frequency with which cells indicated hits if they were on the track. Cosmic ray pulse height was used to check PDT and calorimeter dE/dx values to find problems in the detector. Information from cosmic ray data was analysed and presented to the operator during data runs for diagnostic purposes.

Majority logic was available to provide a trigger for vertical cosmic rays that went through single calorimeter planes. The x position of the vertical cosmic ray in each calorimeter cell was computed from the times of the hits in tubes on either end. The charges collected in the tubes were fitted against the position of the hit with a function that models the attenuation of light as it travels in the liquid scintillator.

$$Q(x) = A(e^{-x/L} + B)$$

The constants A, L, and B were determined from the vertical cosmic ray data.

At the end of the run all the calibration data were combined to produce sets of constants for different periods in the run. Long muon tracks that accompanied the neutrino data were used to fine tune the calibration constants. They were used to establish timing offsets among the four parts of the detector and the timing offsets between the start times for the PDT and calorimeter cells. The long muons were also used to obtain gain constants for the PDTs. Gas amplification of the PDT had to be stabilized by changing the applied high voltage to compensate for changes produced by gas density or gas composition. Gain over the entire detector was stabilized continuously within 5% by measuring the position of the $23KeV$ x-ray peak from a ^{109}Cd source which illuminated a monitor PDT.

9. Test beam

A smaller version of the E734 detector was placed in a test beam at BNL. It has been described in earlier theses[17,18,19].

The test beam at BNL provided beams consisting of protons, pions, muons, and electrons for momenta of about $0.4GeV$ to $5.0GeV$. Magnets was used to select particles of a given sign and momentum. Two gas filled Cherenkov detectors and time of flight measurements were used to identify particles. Beam chambers upstream of the test detector were used to measure the direction of an incoming particle.

Data were taken for several particle types and momentum ranges. The information was used to establish ionization profiles for different particles moving through the detector. Also many of the analysis procedures were tested on these data.

The energy and angular resolution of electron induced showers was very important for the analysis of electron events. Test beam electrons with energies of 0.4, 0.6, 0.8, and 1.0 GeV were bombarded into the test detector. The known incident angle, determined from the beam chambers, was compared with the angle measured by an interactive hand fit (see chapter 4) in each projection of the test detector. An angular resolution function (Fig. 2.9.1(a)) was obtained:

$$\Delta\theta_{x,y} = \frac{(13 \pm 1)mrad}{\sqrt{E_e[GeV]}}$$

The known energy of the electron was then compared with the energy measured in the test detector to obtain the energy resolution function and a scale factor to account for the energy lost in the inactive parts of the detector. The energy resolution function (Fig. 2.9.1(b)) was as follows:

$$\frac{\Delta E}{E} = \frac{0.13}{\sqrt{E[GeV]}}$$

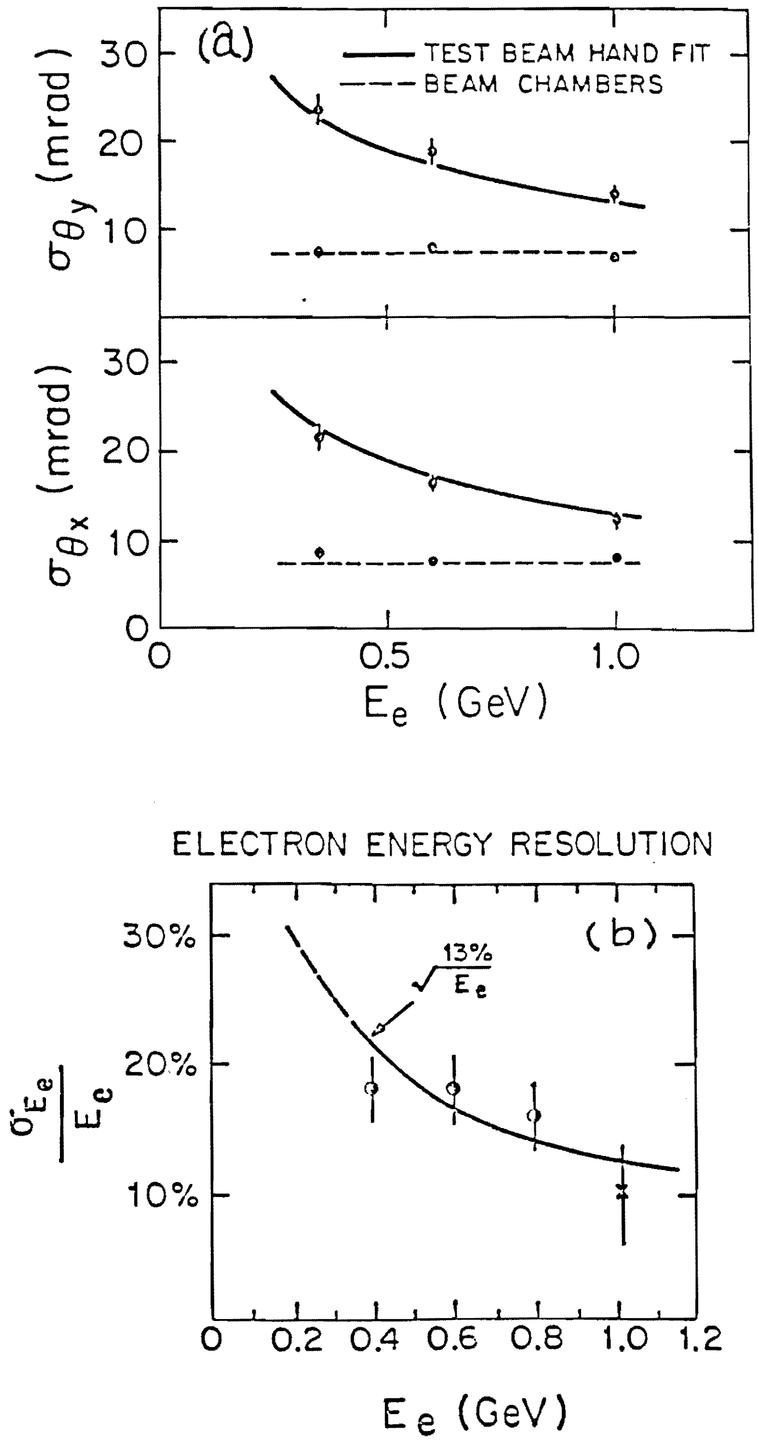

Figure 2.9.1 (a)Angular resolution of electrons in the test beam detector from a hand fit to the PDT data. (b)Energy resolution of electrons in the test beam detector

The scale factor was 1.43 $\pm$ 0.14. In the shower counter the scale factor was determined to be 2.5 ± 0.2. The scale factor was also studied using Monte Carlo simulations and kinematically reconstructing $\nu_e n \rightarrow e^- p$ events seen in the main detector. All results were found to be consistent within 10%.

Chapter 3.

Data Reduction.

The E734 detector has accumulated hundreds of hours of data from exposure to a wide band neutrino or antineutrino beam since becoming operational in 1981. The antineutrino data set consists of 354 (800 BPI from 1981), 325 (1600 BPI from 1983), and 156 (1600 BPI from 1986) raw magnetic data tapes. The neutrino data set consists of 371 (800 BPI from 1981), 311 (1600BPI from 1983), and 240 (1600 BPI from 1986) raw magnetic data tapes.

The data sets from 1981 and 1983 were analysed for neutrino and antineutrino electron scattering, and were the subject of previous theses[14,15,18,19]. This thesis analyses the 1986 data with improved methods. It also presents the entire sample of $\nu_\mu e \rightarrow \nu_\mu e$ and $\bar{\nu}_\mu e \rightarrow \bar{\nu}_\mu e$ elastic scattering events from E734.

The 1986 data consisted of 1.2 million neutrino bursts and 1.13 million antineutrino bursts from the AGS. The expected number of single electron events was small (50 $\nu_\mu e \rightarrow \nu_\mu e$ and 25 $\bar{\nu}_\mu e \rightarrow \bar{\nu}_\mu e$). To achieve this reduction without losing a single event, careful book-keeping and much software was needed. The first step in the reduction occurred with the NUE/FELIX production program.

1. The Production Program

NUE/FELIX, running on a CDC 7600 computer, read events from a raw data tape, used calibration and geometry constants for each element, recognized tracks and showers, and produced two sets of data: a set containing events with single electron showers and a set containing quasi-elastic events for normalization.

For each event all the hits were recorded on the raw data tape. For each hit three numbers were saved: the address of the element, digitized time of arrival of the hit, and the digitized integrated charge. NUE used the calibration and geometry files, which contained the pedestals, gains, time offsets, and co-ordinate positions for each element, to correct the raw time and charge. The time was converted into nanoseconds from the start of the master gate. The charge was converted into energy in MeV. The x-position of the hit in a calorimeter was calculated from the time difference in photo-tube hits from both ends. NUE stored new information along with the old in FORTRAN arrays and COMMON BLOCKS.

As explained in chapter 1 the beam of neutrinos was in bunches, also called time clusters. The same bunch structure was exhibited by the neutrino interactions. The calorimeter hits in each burst had to be grouped in time clusters to separate overlapping interactions in the pattern of hits. For each event a histogram was made of calorimeter hits. The hits were placed in time bins of $40ns$. Hits from nonzero bins that were within two bins of each other were considered to make up one time cluster. PDT elements were associated with a time cluster if the PDT time was within a window around the mean time of the cluster. A PDT could be associated with three different time clusters.

After time clustering, NUE sent events through two different algorithms. All events went through the first algorithm, the PDT filter. The PDT filter recognized events that contained electromagnetic showers; it wrote these events onto a tape. Showers selected by the PDT-filter were further sent to be scanned by eye. Events with tracks in the spectrometer were also written onto the same tape. Spectrometer events were later used to calculate the neutrino spectrum. Every third event went through the second algorithm, which was a track fitting algorithm that fully reconstructed the event and wrote the results in a standardized form onto a data summary tape (DST). The quasi-elastic events, used for normalization, were obtained from these DST's.

2. The PDT Filter:

An electromagnetic shower leaves fluctuating deposits of energy as it travels in the detector. Figure 3.2.1 is an example of events containing electromagnetic showers. A shower is originated by an electron or a gamma ray. A large number of secondary particles are produced through pair production and bremsstrahlung.

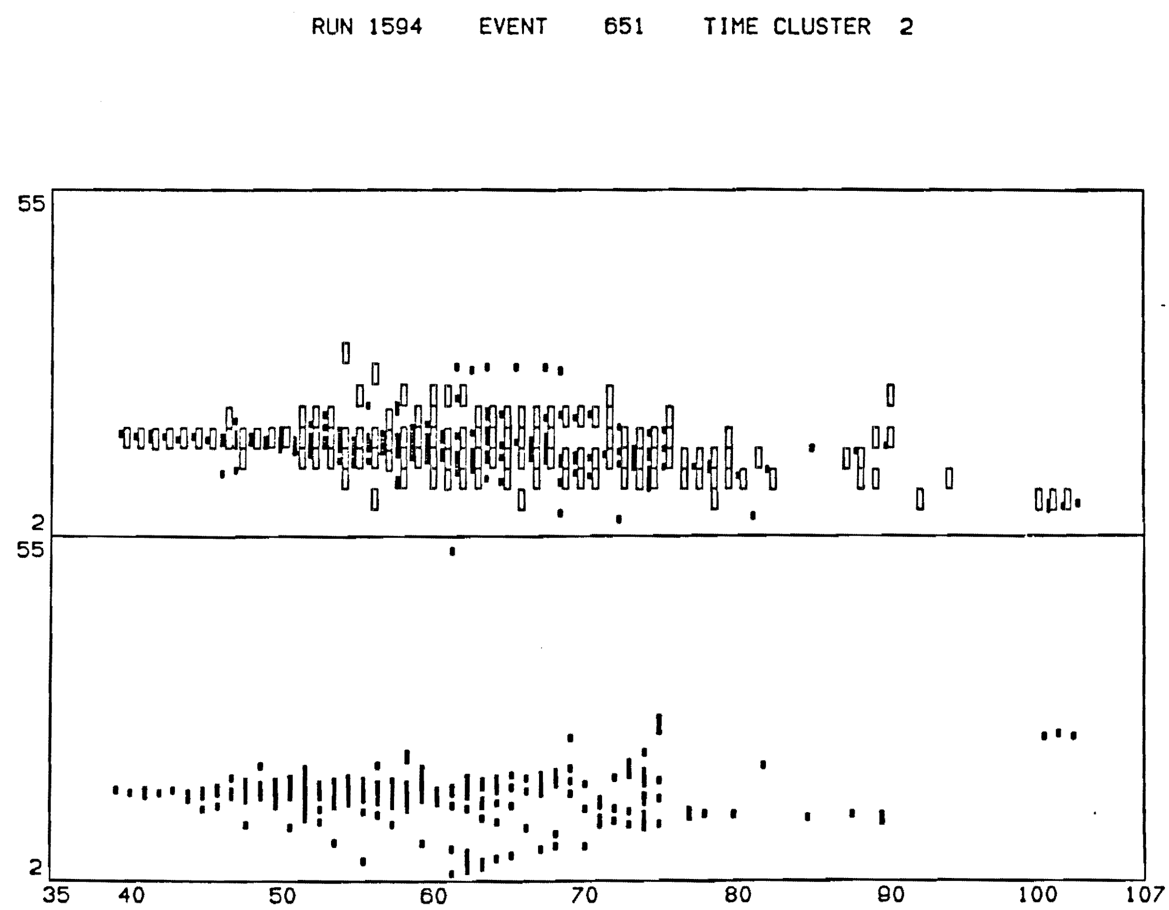

Figure 3.2.1 Example of an electromagnetic shower

Bremsstrahlung photons convert into e^+e^- pairs, which often have enough energy to produce photons that pair-produce. A typical shower starts with a single track; the center of the shower contains a very large number of secondary particles. Towards the end of the shower secondary photons are no longer energetic enough to pair-produce, so the shower, exhausted of its energy, stops. Some photons convert away from the main body of the shower. These appear as single energy deposits or small separated showers.

For an energetic shower the secondary particles tend to be produced at very small angles with respect to the original particle. The finite size of the PDT's does not permit us to follow the development of each particle in the shower. However, the secondaries do cause the number of elements hit per plane to increase along the path of the shower. A 1 GeV shower leaves a typical pattern of hits in the detector: the number of PDT hits per plane increases from one to four or five; the number of calorimeter hits increases from one to two or three; there are several gaps along the length of the shower, and towards the end of the shower there are hits separated from the main body. The PDT filter is an algorithm implemented within NUE to recognize electromagnetic showers of energy above 200MeV. The algorithm used energy and time clustering information from NUE for each event. It used spatial information from the PDT's to recognize patterns associated with electromagnetic showers.

The PDT filter algorithm can be summarized as follows: After rearranging the PDT data for convenience, it steps through the planes for both views looking for an event vertex. After finding a vertex candidate, checks are made downstream and upstream to get a trial fit for the track, to match projections of the track from both views, and to assemble all elements involved in the shower. Finally, restrictions are imposed to make certain that the events found were good electromagnetic showers.

For each time cluster in an event, the PDT filter located the calorimeter planes that contained hits as the region to search for possible showers. It summarized all PDT hits within this region and within a time window ($-100ns <$

$T_{PDT} - T_{cluster} < 1200ns$) around the mean time of the time cluster. Groups of PDT hits that were nearest neighbours in a plane were assigned a mean hit position and error ($error = 8.0cm \times N_{PDT}/2$). The PDT wire position was used as the coordinate for a PDT; drift information was not used in the PDT filter.

For both views, the filter stepped through planes looking for a vertex. For each plane, all combinations of three PDT hit positions in four consecutive planes were considered. The first hit was required to be within a fiducial volume ($3 < x\ or\ y\ PDT < 53$) to eliminate tracks entering from the side. To test if any of the hit combinations could form a shower vertex, a line was fit through the first and the third positions and the following criteria were used: The line must make a slope of less than 0.5 with respect to the beam; the second hit must lie within the error of the second hit position plus the average error of the first and the third hit positions (Fig. 3.2.2); in the first upstream plane, there must be no PDT hits within $16cm$ of the fit line and for the y-view, no calorimeter hits within $20cm$ of the line.

Upon finding a vertex candidate, groups of PDT hits downstream of the vertex were associated with it if they were within a road, defined below:

$$\Delta x < 8.0cm \times N_{hits}/2 + 0.06 \times \Delta z + 8.0cm$$

or

$$\Delta x < 8.0cm \times N_{hits}/2 + 20.0cm$$

where Δx is the transverse distance of the PDT group from the trial line and Δz is the downstream distance of the PDT group from the vertex. The first term on the right is the error on the position of each PDT group, and the second term is a simple model for effects of multiple scattering. The PDT filter stepped through the planes checking groups of PDT's until it encountered a plane with no PDT hits within the road in either view. It then calculated a new trial line based on all the PDT groups found to be part of the event. The process of searching for PDT hits within the road downstream of the vertex was repeated with the new trial

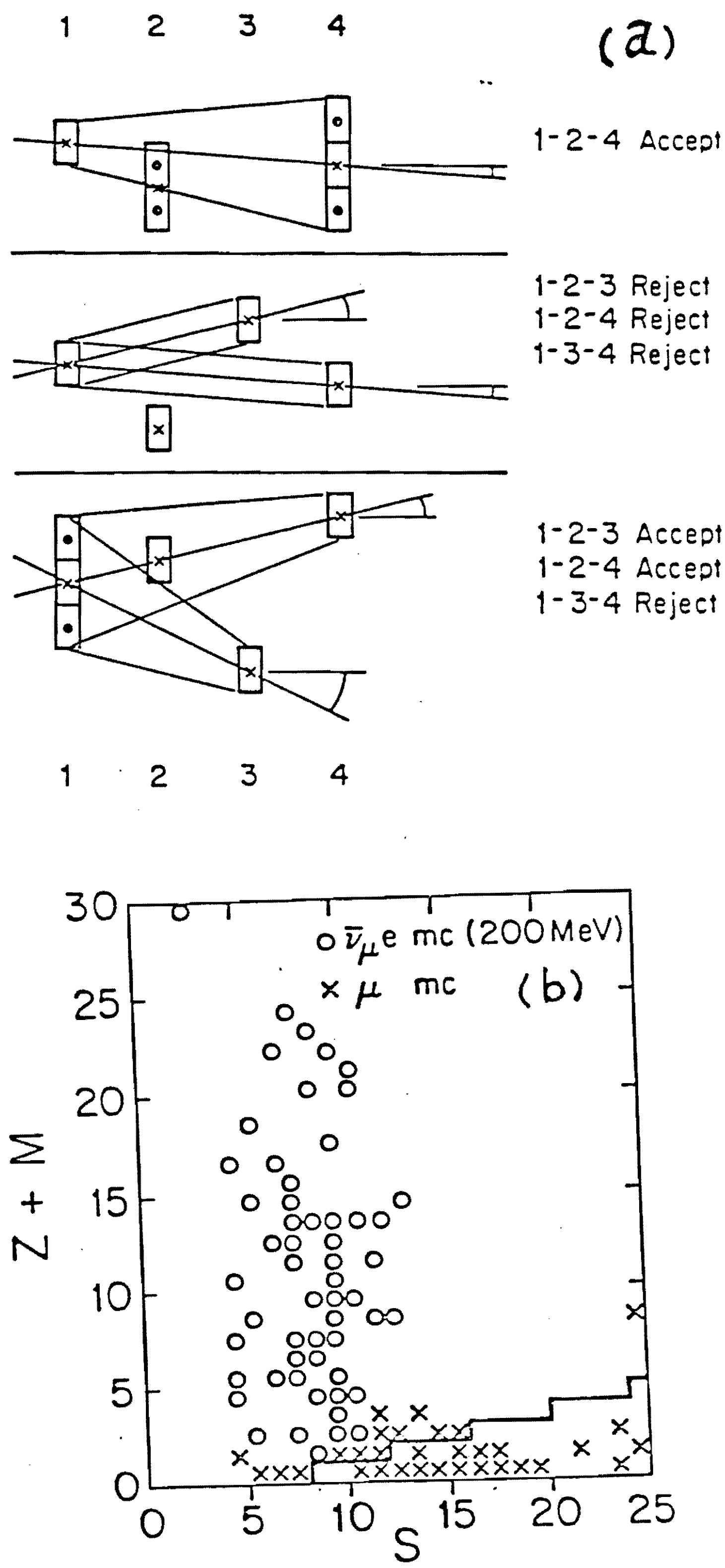

Figure 3.2.2 (a) Examples of vertex search (b) Multiple hit criterion

line. This process was iterated three more times. Four iterations were found to be sufficient to converge to a stable solution. At each iteration the new candidate was checked against all previous ones to prevent superfluity.

After the last iteration, the module upstream of the vertex was checked for an x-PDT hit within $9cm$ of the trial line or a scintillator hit within $20cm$ and a y-PDT hit within $9cm$ of the trial line. If such hits were found, the trial line was rejected. The filter also required the shower to be longer than three modules. If the shower was not found to exit the detector, the shower length in each view was required to be within four modules of each other. PDT hits associated with the trial line were not used in finding more vertices downstream. The rest of the PDT hits and all of the calorimeter hits within two modules upstream of the vertex and 15 modules downstream of the end of the trial line were now considered for association using a different road, defined below with the same conventions as in the previous paragraph:

For calorimeter cells,

$$\Delta x < 50.0cm \times N_{cells}/2 + 0.06 \times \Delta z + 8.0cm$$

or

$$\Delta x < 50.0cm \times N_{cells}/2 + 45.0cm.$$

For PDT hits,

$$\Delta x < 8.0cm \times N_{hits}/2 + 0.06 \times \Delta z + 8.0cm$$

or

$$\Delta x < 8.0cm \times N_{cells}/2 + 45.0cm.$$

After assembling all elements of the shower, angle and energy cuts were performed. The energies in the first two planes (E_{vtx1} and E_{vtx2}) were calculated by adding the energies in the calorimeter cells of those planes. Total energy, E_{tot}, was calculated by summing up all the associated calorimeters; the angle of the particle that initiated the shower was determined from the final trial lines in the two views. The following cuts were applied:

$$-0.350 < \tan\theta_{PDT} < 0.350$$

$$E_{vtx1} < 60MeV$$

$$E_{vtx2} < 60MeV$$

$$E_{tot} > 100MeV$$

The first cut got rid of large angle backgrounds, since we were searching for single electron events, which kinematically constrained to small angles. The vertex cuts got rid of multi-track events that deposit more energy in the first few modules than the single electrons. The cut on total energy limited the number of low energy showers, which are often short, difficult to identify, and dominated by backgrounds.

A candidate shower was further checked for gaps, multiple hits and containment. The shower was considered to have gaps if there were calorimeter hits downstream of the end of the trial line. The shower was considered to have multiple hits if the shower satisfied the following conditions:

$$M + S > Z$$

and

$$M + Z > S/4 - 2$$

where M is the number of planes with more than one calorimeter hit; S is the number of planes with only one calorimeter hit, and Z is the number of planes with zero calorimeter hits. A Monte Carlo study [25–26] of muon and electron tracks through the detector indicated that muons tend to have only a single calorimeter hit per plane while electrons tend to have several hits per plane (Fig. 3.2.2). The shower was considered to be contained if it did not exit the side of the fiducial volume in either view. The shower candidate was finally accepted (1) if it was contained and had gaps, or (2) if it was more than 40 modules long, had gaps, and had multiple hits, or (3) if it was not contained but had multiple hits.

The PDT filter went through every time cluster of every event. Each event with a time cluster containing a hit pattern that passed the filter criteria was recorded along with information generated by the PDT filter.

3. Vertex Cleanup:

Examination of events selected by the PDT filter revealed the presence of many electromagnetic showers with additional tracks at the vertex. The PDT filter did not contain adequate pattern recognition capabilities to reject events with activity at the vertex. During the analysis of 1981 and 1983 data, performance of the PDT filter was considered sufficient, and the selected events were eye-scanned. For the 1986 data, an algorithm was constructed to examine the vertex region in more detail.

The algorithm used information generated by the PDT filter, such as the vertex of the event. It constructed three two dimentional arrays to represent the pattern of hits near the vertex for scintillators and the x and y PDT's. If a hit was found outside a boundary imposed inside the array (Fig. 3.3.1), the program looked for the next adjacent hit pointing towards the vertex plane. If such a hit was found, the program continued the process of tracking towards the vertex plane. The event was rejected if the program reached the *vertex cell*, proving the vertex as the origin of a track. This procedure was carried out independently for the three different arrays representing three different views of the event (Calorimeters, X-PDT and Y-PDT). During these procedures the program had to handle many patterns as special cases. The special cases were mainly results of tracks going through gaps between the cells or spurious hits.

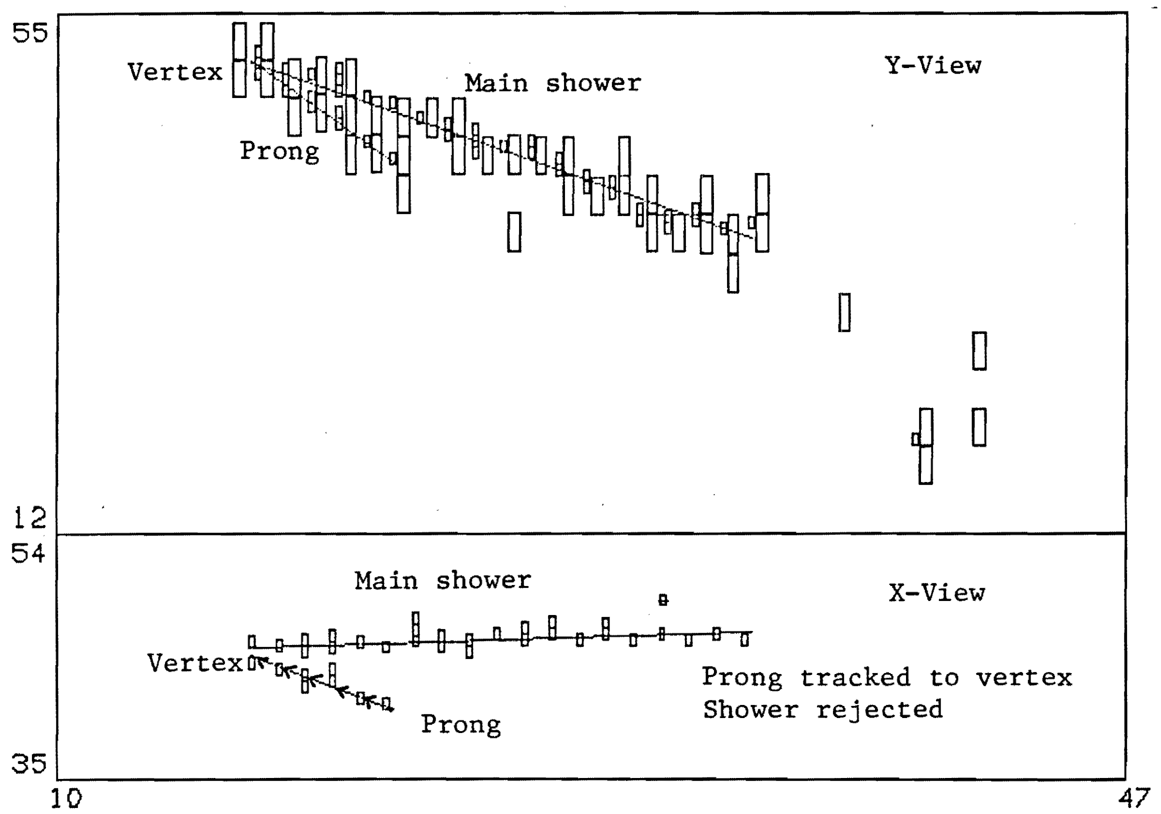

Figure 3.3.1 Vertex cleanup procedure.

Events that passed the PDT filter and vertex cleanup were eye-scanned. The vertex cleanup procedure reduced the number of events to be scanned by approximately 40% over processing with the PDT filter by itself. Data from 1981 and 1983 that were already scanned and analysed were processed through the vertex cleanup procedure to check its efficiency. Less than 2.0% of the showers from the previous data were rejected by the vertex cleanup process. The rejected showers had overlapping long tracks that went through the shower vertex.

4. NUE track fitting

Two dimensional track fitting with the PDT hits was performed first. Stepping through each plane, combinations of three PDT hits from five consecutive planes were formed. The first combination in a straight line was considered an upstream end of a track. The track fitting algorithm followed the line downstream to associate PDT's with the track. Thus both views in all time clusters were checked for tracks. The scintillators were used to match PDT hits in a track with a time cluster. Tracks from both views were matched in three dimensions using the vertex position and length; three dimensional tracks were formed.

For better knowledge of the track, PDT drift distances were used to fit the 2 dimensional tracks previously found. The drift distance was obtained from the difference between PDT trigger time and the trigger time of the nearest associated scintillator. The drift distance was related to the drift time using a table, which was calculated using straight muons that go through the detector. Each drift distance has an ambiguity as to which side of the PDT wire the particle passed. A tree algorithm was used to resolve the ambiguity and determine the proper combination of drift distances for the best line fit. After fitting all the tracks again, NUE found tracks emanating from a common vertex and marked the vertices as multiprong events.

All tracking and vertex information generated by the track fitting algorithm was stored on a DST. The events from the DST's were later analysed for quasi-elastic interactions, which provided us with a normalization for the data.

Chapter 4.

Electromagnetic Showers

The PDT filter working through NUE identified 300386 electron candidates from the neutrino data and 108607 from the antineutrino data. These events were written to 44 (6250 BPI) magnetic tapes which were used for later analysis.

1. *The Eye Scan:*

The shower events on the output tapes from NUE were first taken through the vertex cleanup procedure. This procedure selected 165010 neutrino events and 63007 antineutrino events which were used to prepare the eyescan. Because of the difficulty and complexity of pattern recognition for electromagnetic showers with software and the need for high signal acceptance, an eyescan by physicists was considered practical.

Events that passed the vertex cleanup procedure and had a PDT shower angle, θ_{PDT}, of less than $0.2 rad$ were selected for eyescanning. Events with PDT shower angle greater than $0.2 rad$ consisted mostly of muons and multiprong interactions. The requirement on this angle reduced the number of events for eyescanning to 79380 for the neutrino sample and 31005 for the antineutrino sample. A line printer plot was made of each event to be scanned. The plots were output onto micro fiche for fast easy viewing (Fig. 4.1.1). Monte Carlo simulated events were randomly inserted among real events at a level of 4% as a control on eyescanning efficiency. In a separate file a record was kept of each event on micro fiche. The record was updated when the event was chosen by a physicist.

The Monte Carlo events inserted in the eyescan were overlaid onto events randomly selected from the data. The Monte Carlo events were positioned in time to correspond to one of the time buckets of the beam with the same 30ns FWHM distribution within the bucket. Energy and timing inefficiencies were added to the Monte Carlo events to closely emulate real events.

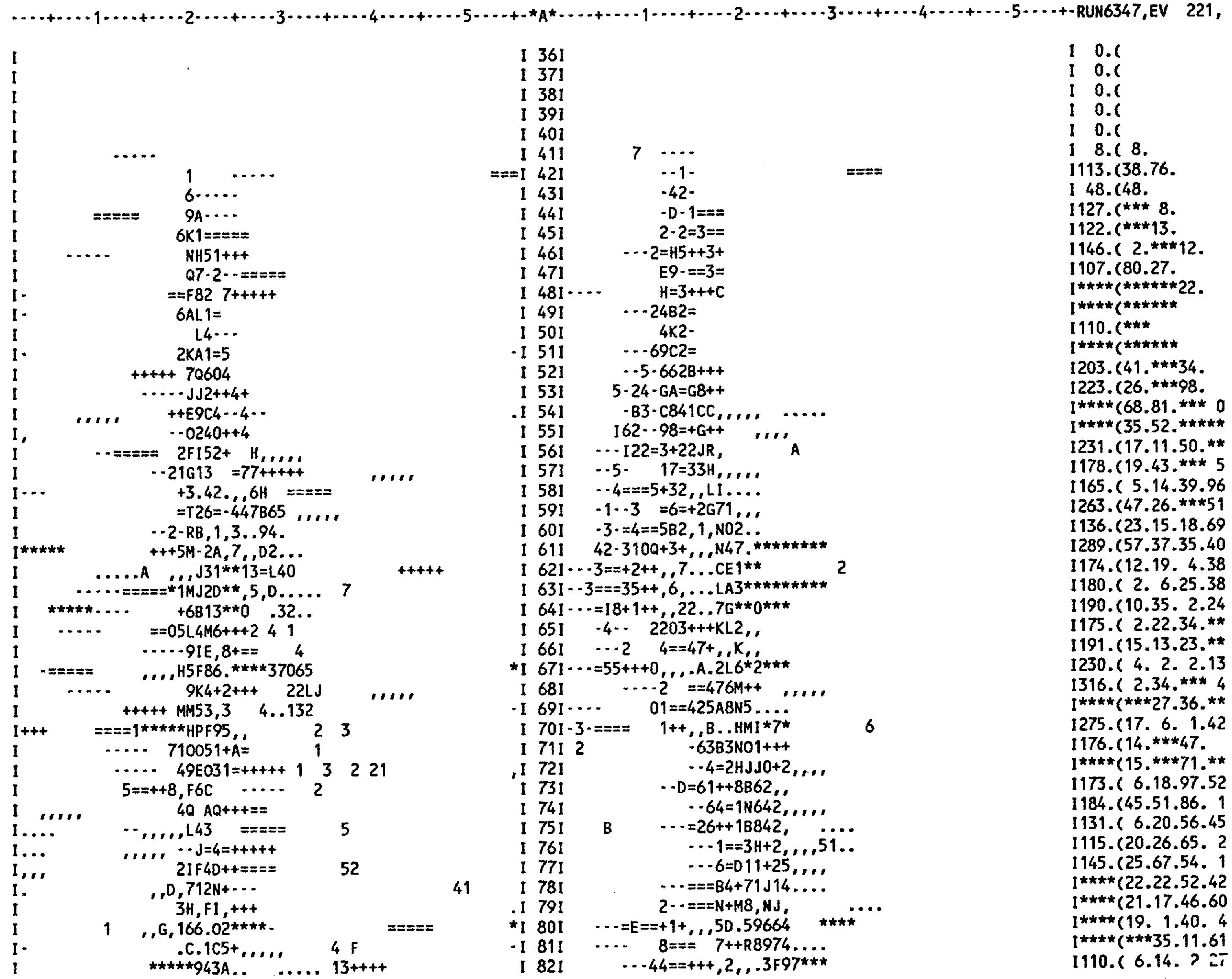

Figure 4.1.1 Line printer plot of a shower candidate. Plots were put onto micro fiche for convenience. The numbers represent PDTs in each view of the detector and the short rows represent calorimeters.

A physicist viewed the events on a micro fiche projector and marked selected events on a list. The physicist was given no information about which hits the PDT filter had chosen as a shower candidate. His task was to find any electromagnetic showers in an event frame. If the event frame contained no showers the event was rejected. The scanning rules (appendix 1) were designed to find single electromagnetic showers that had no associations with other interactions in the same time cluster. It was required that the shower did not point back to another interaction and that there were no extra tracks originating from the vertex of the shower. Accepted shower candidates were grouped in two categories: "electron or gamma" or "stub".

"Electron or gamma" candidates were showers judged as being possible signal events with no association to other activity in the time cluster. "Stub" candidates were showers with clear association with an upstream energy deposit in the scintillators. "Stub" events were cases where the shower was caused by a photon from the decay of a π^0 that was produced by an interaction at the position of the upstream scintillator hits. All of the events were scanned by at least one physicist with constant checks on the scanning efficiency. One third of the events were scanned by two physicists. All the events selected as "electron or gamma" or "stub" were plotted again for a second eyescan. The second scan was done by one physicist, but one third of the events were looked at by two as a check on the efficiency. The rules for the second scan are in appendix 1; events were again grouped in the same two categories. The "electron or gamma" sample contained the signal events and was used for the final analysis. The "stub" sample was used for background studies.

All of the scanning took approximately six months. Scanning and computer processing of the data was performed concurrently. The data reduction is summarized in table 4.1.1. The uniformity of the computer processing and scanning was tested by forming the ratio of electron candidates and muon candidates found during the normalization analysis (see Chapter 5). The e/μ ratio was found to be

Analysis step	1986 ν_μ	1986 $\bar{\nu}_\mu$
P.O.T.	1.0589×10^{19}	1.2692×10^{19}
PDT filter	300386	108607
Vertex cleanup	165010	63007
$\theta_{PDT} < 0.2$	79380	31005
1st eye scan	8199	3566
2nd eye scan	3432	1572
analysis cuts	589	403
e/γ cut	345	258
$\theta^2 < 0.03$	221	195

Table 4.1.1 Data reduction

normally distributed with the mean at 0.090 ± 0.044 (0.064 ± 0.025) for neutrino (antineutrino) data.

2. Final Cuts

The event sample obtained by scanning contained all interactions that looked like electromagnetic showers in the detector. The sample obviously contained background events that had to be eliminated using energy and angle information. The event signatures expected for signal and the important backgrounds are listed below:

Neutrino "electron or gamma" sample –

1) $\nu_\mu e \rightarrow \nu_\mu e$: signal event, low energy in the vertex cell, minimum ionizing, low total energy, very forward in angle.

2) Shower due to a photon from the decay of π^0: twice minimum ionizing, low total energy, uniformly distributed for small angles.

3) Shower due to the electron from $\nu_e + n \longrightarrow e + p$: high energy in the vertex cell, minimum ionizing, high total energy, uniformly distributed for small angles.

Antineutrino "electron or gamma" sample –

1) $\bar{\nu}_\mu e \longrightarrow \bar{\nu}_\mu e$: signal event, low energy in the vertex cell, minimum ionizing, low total energy, very forward in angle.

2) Shower due to a photon from the decay of π^0: twice minimum ionizing, low total energy, uniformly distributed for small angles.

3) Shower due to the positron from $\bar{\nu}_e + p \longrightarrow e + n$: low energy in the vertex cell, minimum ionizing, high total energy, uniformly distributed for small angles.

The "electron or gamma" and the "stub " data sets were processed through a program which calculated various quantities concerning the shower to facilitate analysis. The program ran the PDT filter again to summarize the event. It located the shower found by the scanner. If it failed to find the scanner's shower, it selected the largest shower (most number of PDT hits) found by the PDT filter. The program evaluated the shower angle using a least squares fit to the drift distances in the PDTs (calculated from the drift times). The fit encompassed all possible combinations of PDT hits with weighted uncertainties based on the effects of multiple scattering. The total energy of the shower and the energy deposits in the cells of the first six planes were also determined by the program. The information was assembled in a FORTRAN data common block. The event and the common block were written to a standard format data summary tape (DST).

The total energy (computated by adding energy deposited in all the cells associated with the shower) had to be corrected by a scaling factor (see end of chapter 2) that accounted for energy lost in the inactive parts of the detector such as the walls of the calorimeters. Studies of energy deposits of muons traversing the detector determined the scaling factor to be stable within 10% during the entire data accumulation period.

The following cuts were applied to the data to further condense the size of the event sample:

1) Fiducial volume cut:

$$7 < X_{PDT} < 51$$
$$7 < Y_{PDT} < 51$$
$$7 < Z_{module} < 97$$

X_{PDT} and Y_{PDT} are the wire positions of the vertex PDT cell, and Z_{module} is the module number of the vertex. Events that failed above restrictions were eliminated. This cut eliminated front and side entering tracks and showers which were not fully contained in the detector. It eliminated front entering photons generated by interactions in the shielding in the front of the detector(see Fig. 4.2.1 and Fig. 4.2.2).

2) Energy cut:

$$210MeV < E_e < 2100MeV$$

E_e is the total energy of the shower corrected by the scaling factor. Events that failed above criteria were rejected. After some studies[18] this cut was considered most effective in reducing low and high energy backgrounds. π^0 decays and hadrons dominated at low energies and quasielastic electron neutrino interactions dominated above 1500 MeV(see Fig. 4.2.3).

3) Vertex energy cut:

$$E_{vertex} < 30MeV$$

Events with greater than 30 MeV in the first calorimeter cell were rejected. This cut addressed the background events due to hadrons and the quasielastic electron neutrino interactions. The final state hadron in these reactions tended to deposit high energy in the vertex cell. Monte Carlo studies[19] suggested that vertex energy of 30 MeV was the upper limit for the true electron signal (see Fig. 4.2.4).

The most important signature for the neutrino electron elastic scattering events was the extremely forward angle of the initial electron in showers arising

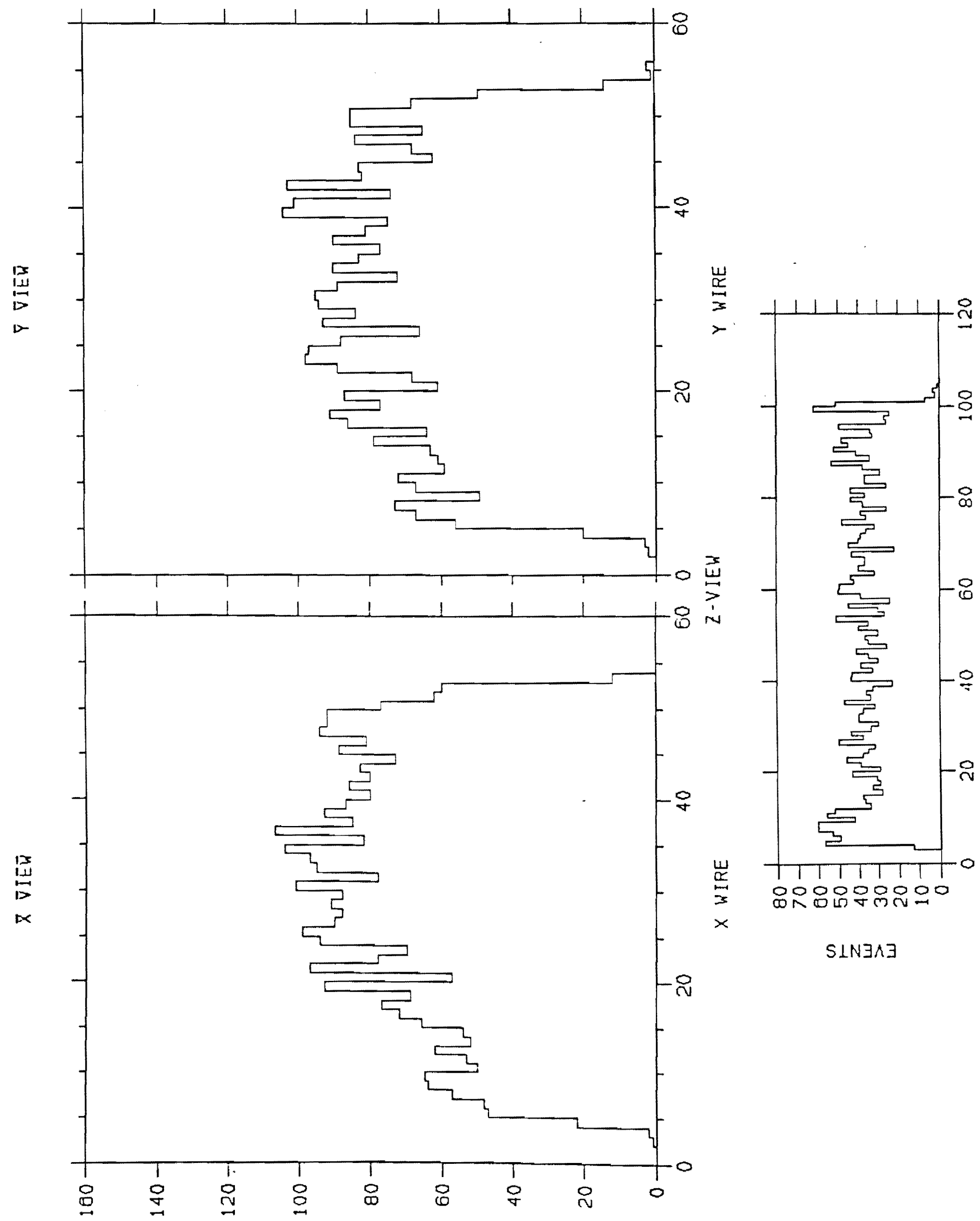

Figure 4.2.1 Vertex position distributions for the neutrino events

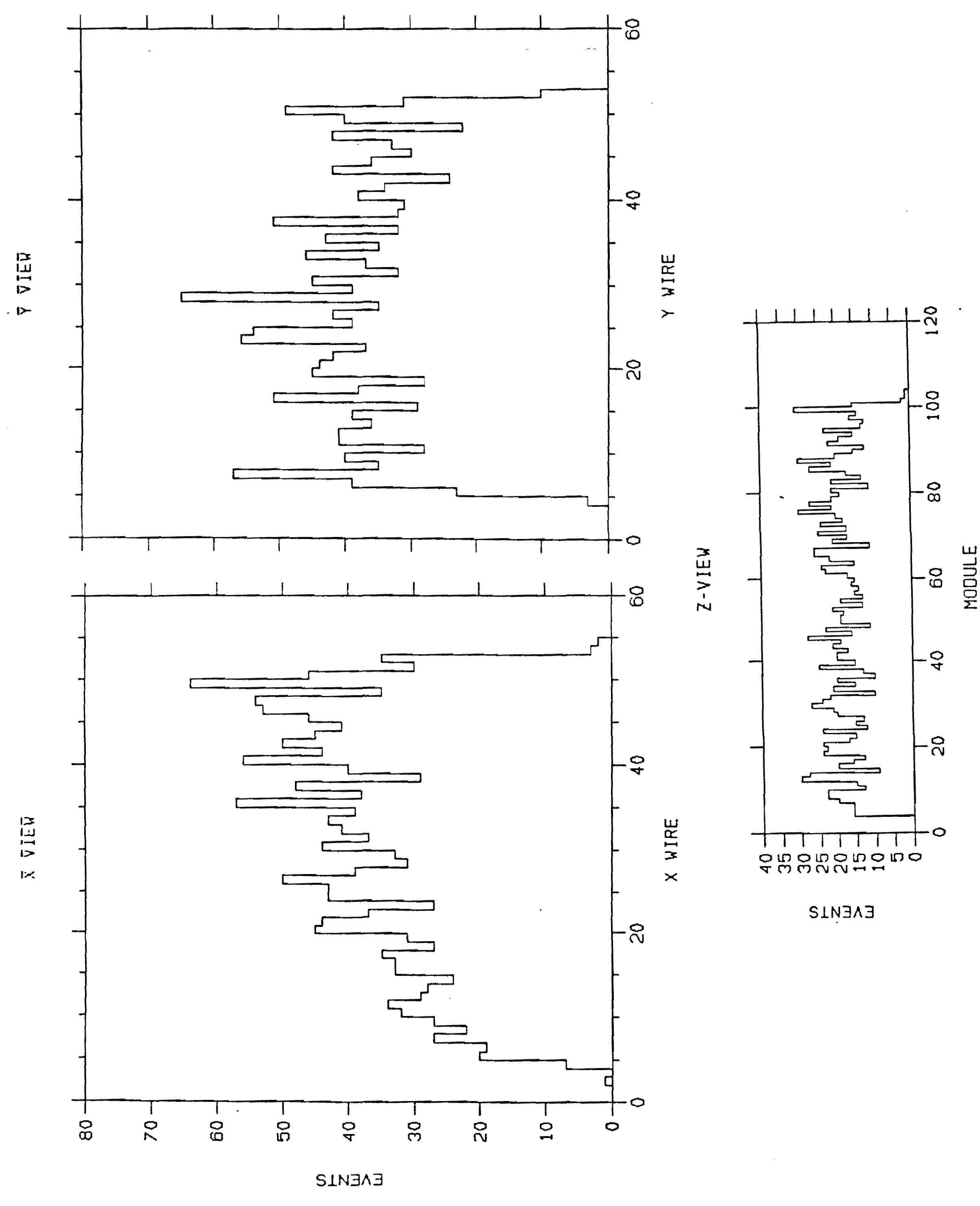

Figure 4.2.2 Vertex position distributions for the antineutrino events

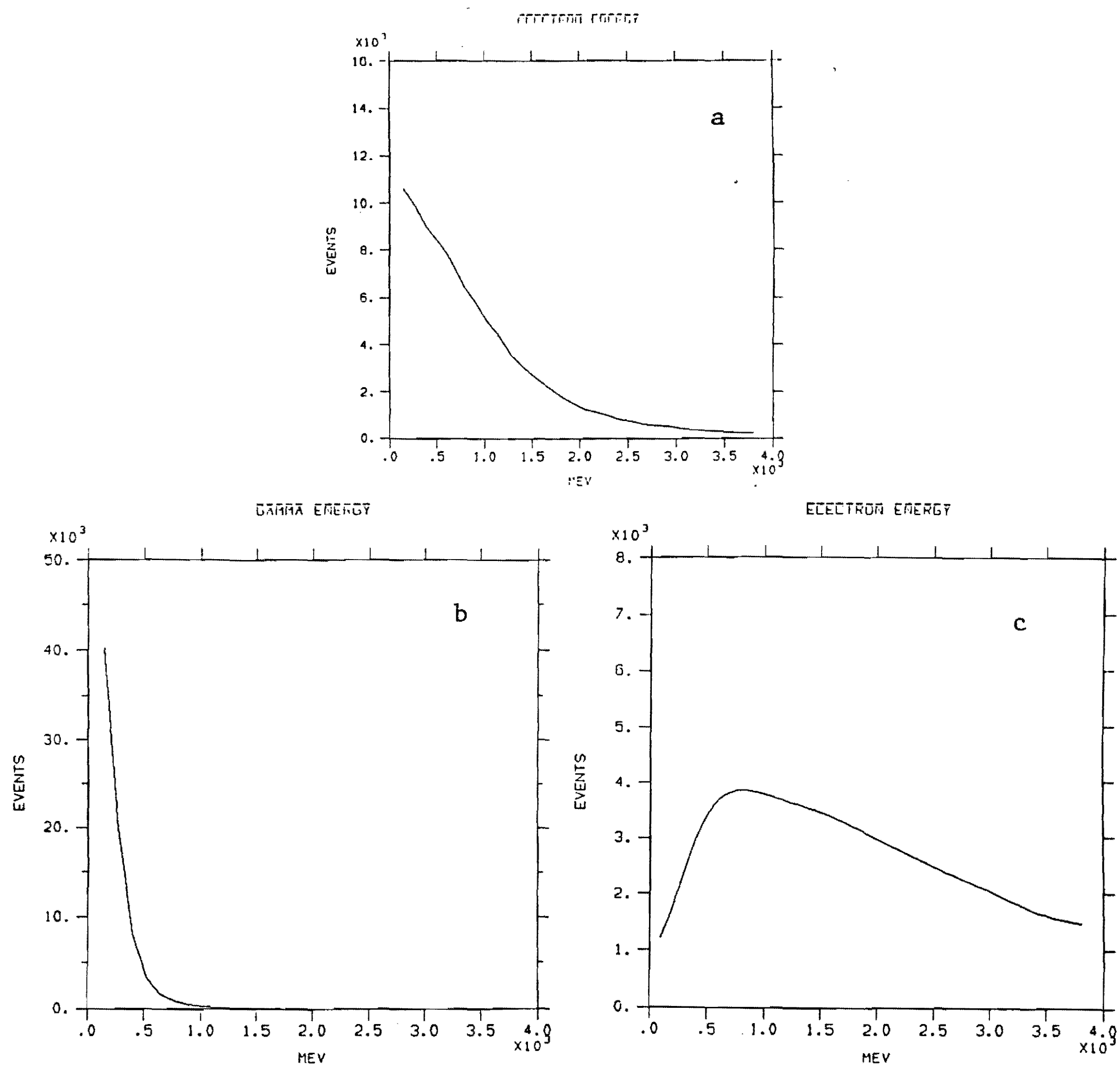

Figure 4.2.3 Monte Carlo simulations of shower energy for $\nu_\mu e \rightarrow \nu_\mu e$(a), photons from the pion in $\nu_\mu + n \rightarrow \nu_\mu + n + \pi^0$(b), and $\nu_e n \rightarrow e^- p$. Distributions for the antineutrino reactions are similar.

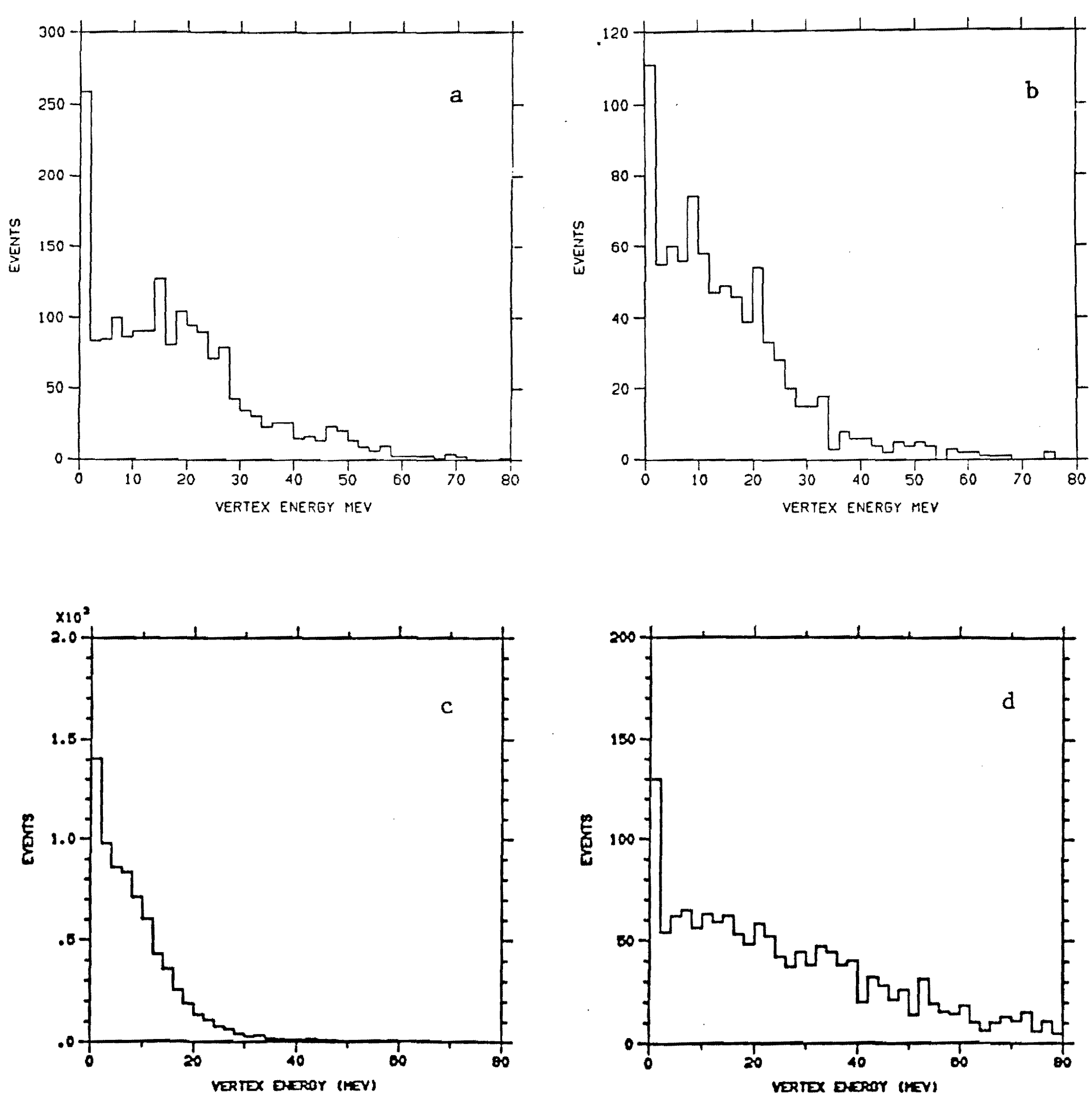

Figure 4.2.4 (a) Vertex energy for the neutrino sample. (b) Vertex energy for the antineutrino sample. (c)$\nu_\mu e \rightarrow \nu_\mu e$ Monte Carlo. (d)$\nu_e + n \rightarrow e^- + p$ Monte Carlo.

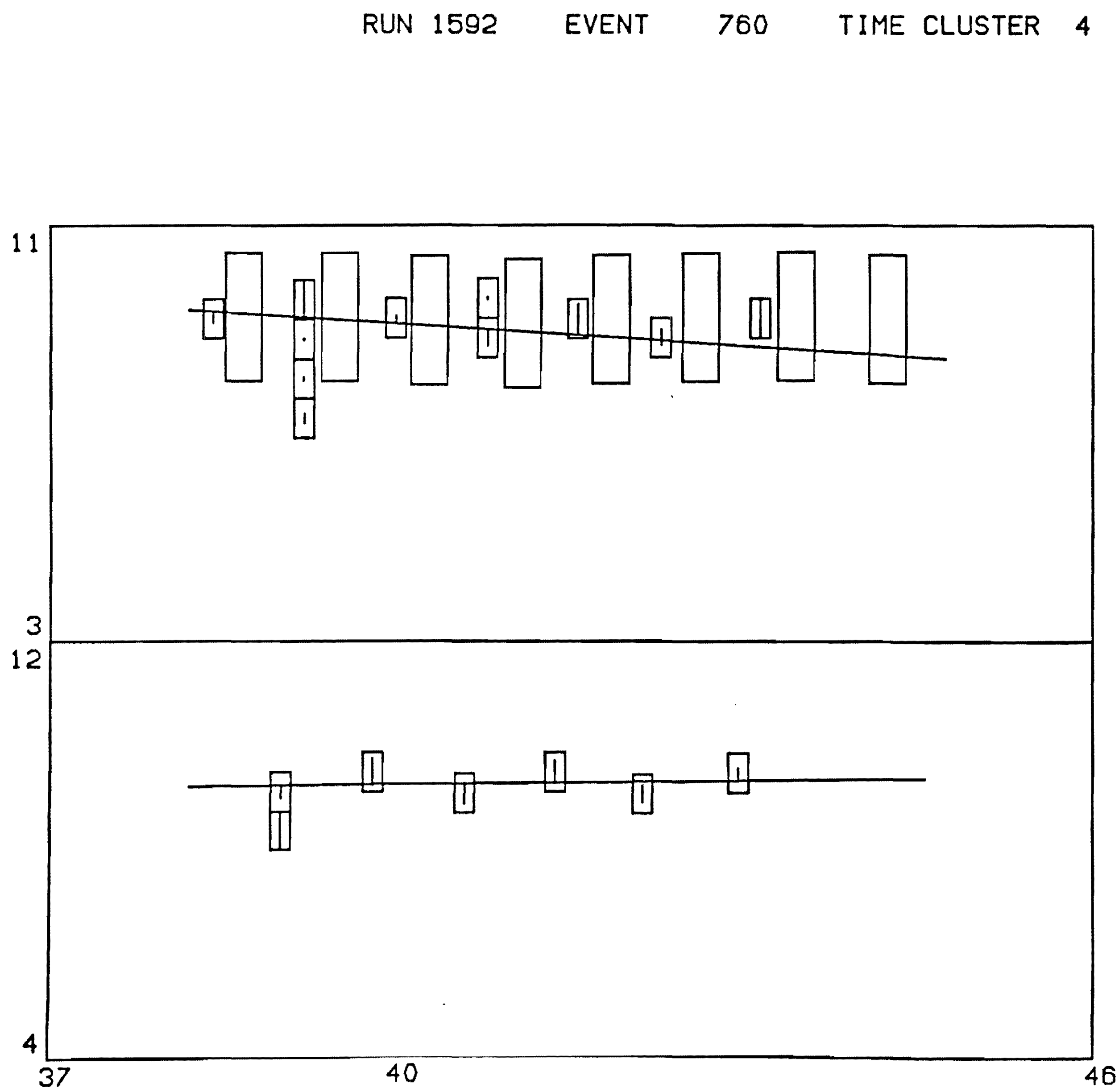

Figure 4.2.5 Interactive display for manual fitting of the angle

from them. Full exploitation of the high angular resolution of the PDTs was essential. Thus, manual fitting of the angles of the chosen events was considered appropriate. Each event was displayed on a graphics screen along with the fits obtained by the pattern recognition programs; the operator was allowed to expand any part of the event for closer examination. Using the displayed PDTs and drift distances the operator chose a fit to the track in the front part of the shower. The operator chose fits in both views of the event until he was satisfied with the goodness of the fit (see Fig. 4.2.5). The fits obtained by the pattern recognition programs were chosen if they were judged acceptable. No systematic bias was found after the manual fits.

After accurate determination of the angles, another interactive topological selection procedure was applied to reject showers from hadronic interactions and showers from overlapping photons of π^0 decays. These showers tend to be broad because they are composed of numerous particles; multiple scattering makes them deposit much more energy away from the center of the shower than electron showers of similar energy. A "maximum multiple scattering road" was applied to the showers (see Fig. 4.2.6); the road was based on the maximum scattering limits of a single electron. A line, 20 modules long, was also drawn upstream of the shower vertex. The sum of the shower energy outside the road and the sum of the energy directly upstream of the vertex were displayed. The operator rejected the event (1) if the energy outside the road was greater than 2.5% or (2) if there was greater than $10MeV$ deposited directly upstream. The operator exempted events from above criteria if he judged that the energy determinations were complicated by unassociated interactions in the same time bucket.

During NUE processing some data tapes were accidently processed more than once. NUE had also marked some events as having microprocessor errors. Events that were duplicated or had microprocessor errors were removed from the event samples. During normalization processing some runs were judged to be bad because of unusually high energy deposits which indicated calibration errors or high computer error rates which indicated malfunction in data acquisition. Events

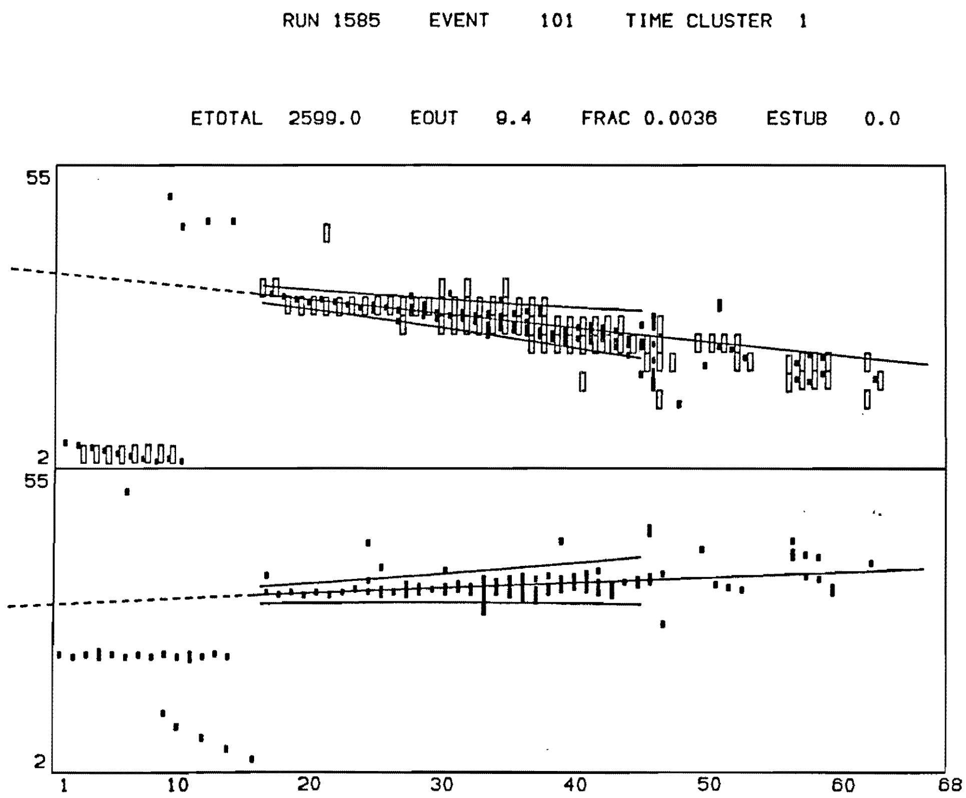

Figure 4.2.6 Graphic event display for application of the maximum multiple scattering road

belonging to bad runs were also removed from the samples; the normalization was adjusted accordingly (see chapter 5). Application of above cuts reduced the number of events to 589 for the neutrino sample and to 403 for the antineutrino sample.

The event samples, at this point, contained with great certainty either electrons or photons. The PDT and scintillator dE/dx measurements near the vertex were used to separate the "electrons" and "photons". Monte Carlo and test beam studies of single electrons and e^+e^- pairs suggested that true electrons appeared with high probability($> 90\%$) as singly ionizing and true photons appeared ($> 70\%$) as doubly ionizing. Photons that converted assymetrically with most of the energy going to one member of the e^+e^- pair, of course, appeared singly ionizing. Energy deposited in the first scintillator cell after the vertex was used as the measure of scintillator dE/dx (see figures 4.2.7 and 4.2.8). The PDTs being low mass devices have a large probability for registering no energy; their dE/dx distributions also have long tails – called Landau tails – at high dE/dx values, and so a truncated mean approach was used to determine PDT dE/dx. Both x and y PDTs on the track in the two planes after the vertex were used. If a PDT had no energy it was excluded from further calculation. Minimum of the two energies in each plane was determined, and their mean was used as the measure of PDT dE/dx. The following region was designated as the "gamma" region:

$$dE/dx[CAL] = [E_{cal2}] > 18MeV$$

and

$$dE/dx[PDT] = \frac{min(E_{x_1}, E_{y_1}) + min(E_{x_2}, E_{y_2})}{2} = [E_{av23}] > 15KeV$$

Any event not classified as "gamma" was considered an "electron". The dE/dx cut is identified as the e/γ cut. Since there were hardly any ($< 1\%$) signal events beyond $0.03rad^2$, all events with $\theta^2 > 0.03rad^2$ were discarded. The final cut reduced the number of electron events to 221 (195) and the number of photon

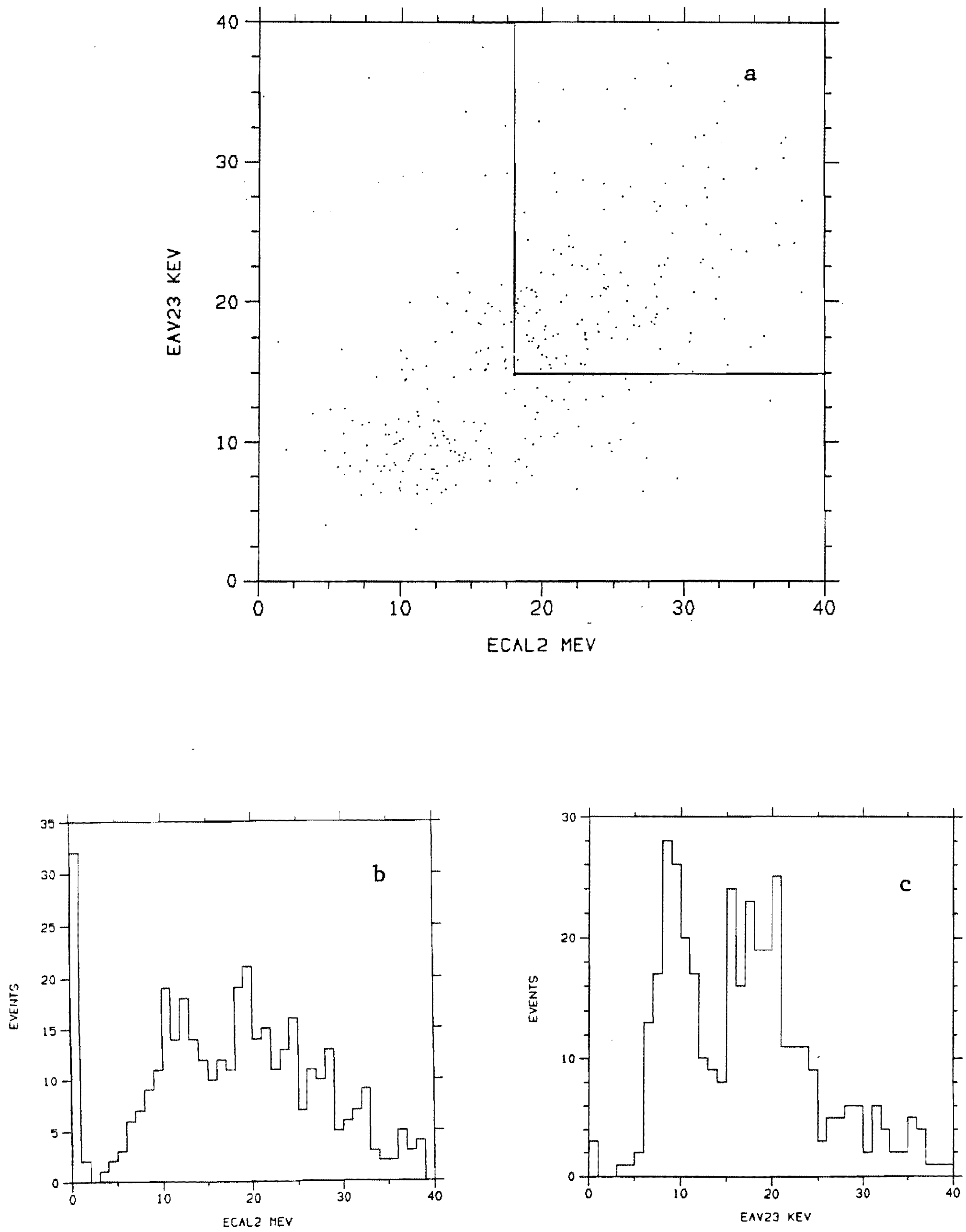

Figure 4.2.7 dE/dx distribution for neutrino data from 1986. a) Scatterplot of E_{cal2} and E_{av23}. The e/γ cut is the solid line. b) Projection for E_{cal2}. c) Projection for E_{av23}

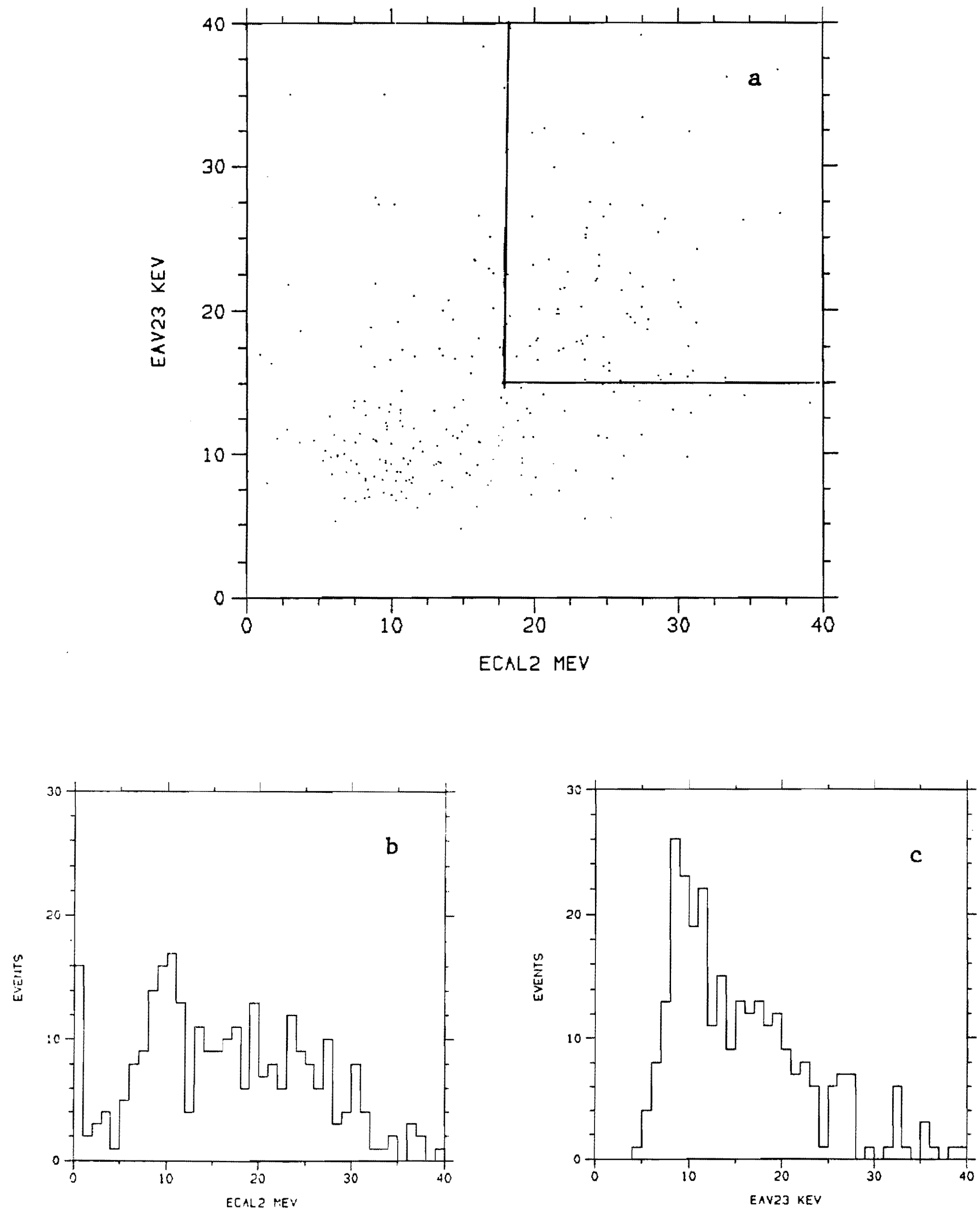

Figure 4.2.8 *dE/dx* distribution for antineutrino data from 1986. a) Scatterplot of E_{cal2} and E_{av23}. The e/γ cut is the solid line. b) Projection for E_{cal2}. c) Projection for E_{av23}

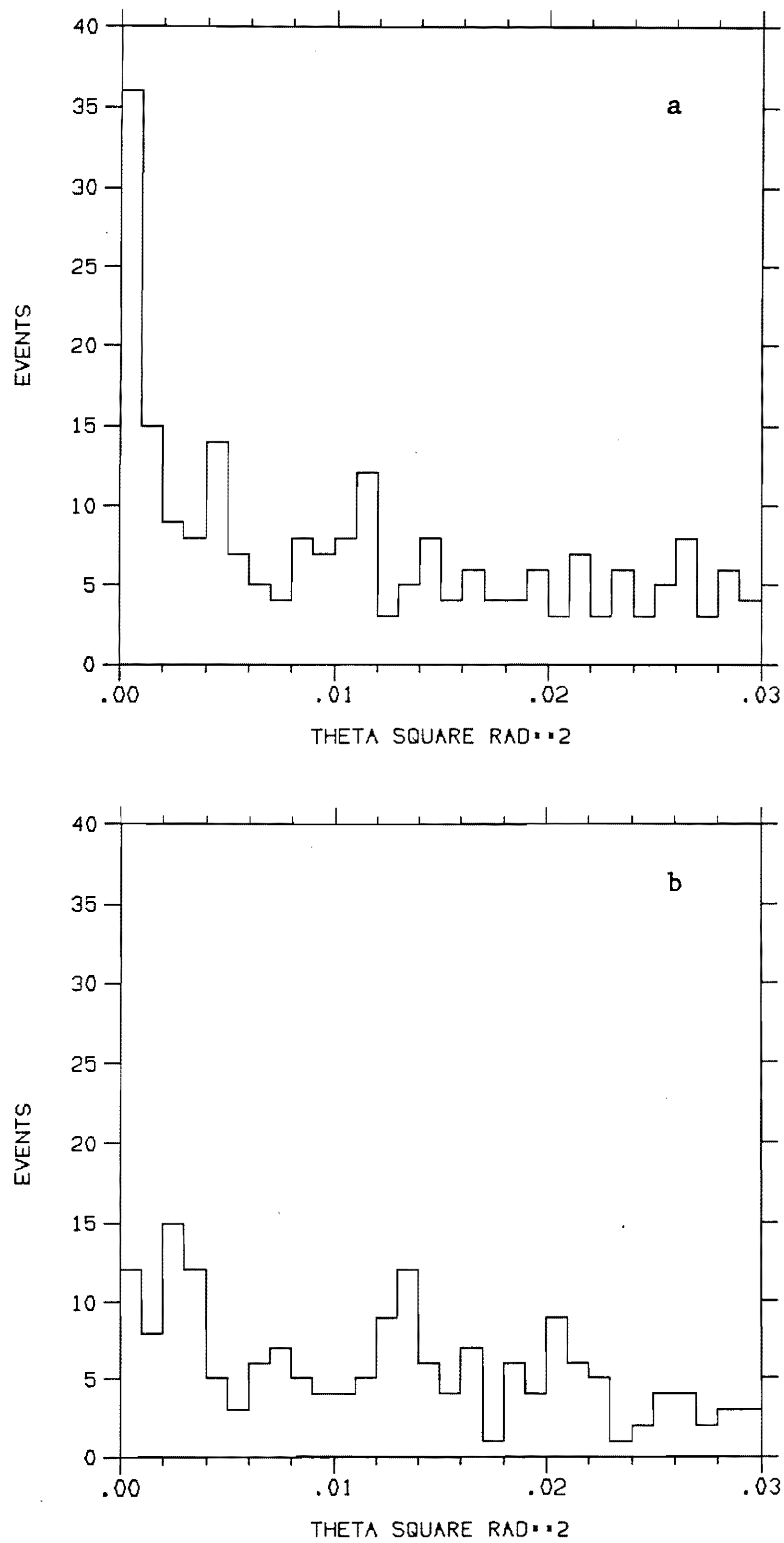

Figure 4.2.9 θ^2 distribution for neutrino data in 1986. a) Electrons identified by the e/γ cut. b) Photons identified by the e/γ cut.

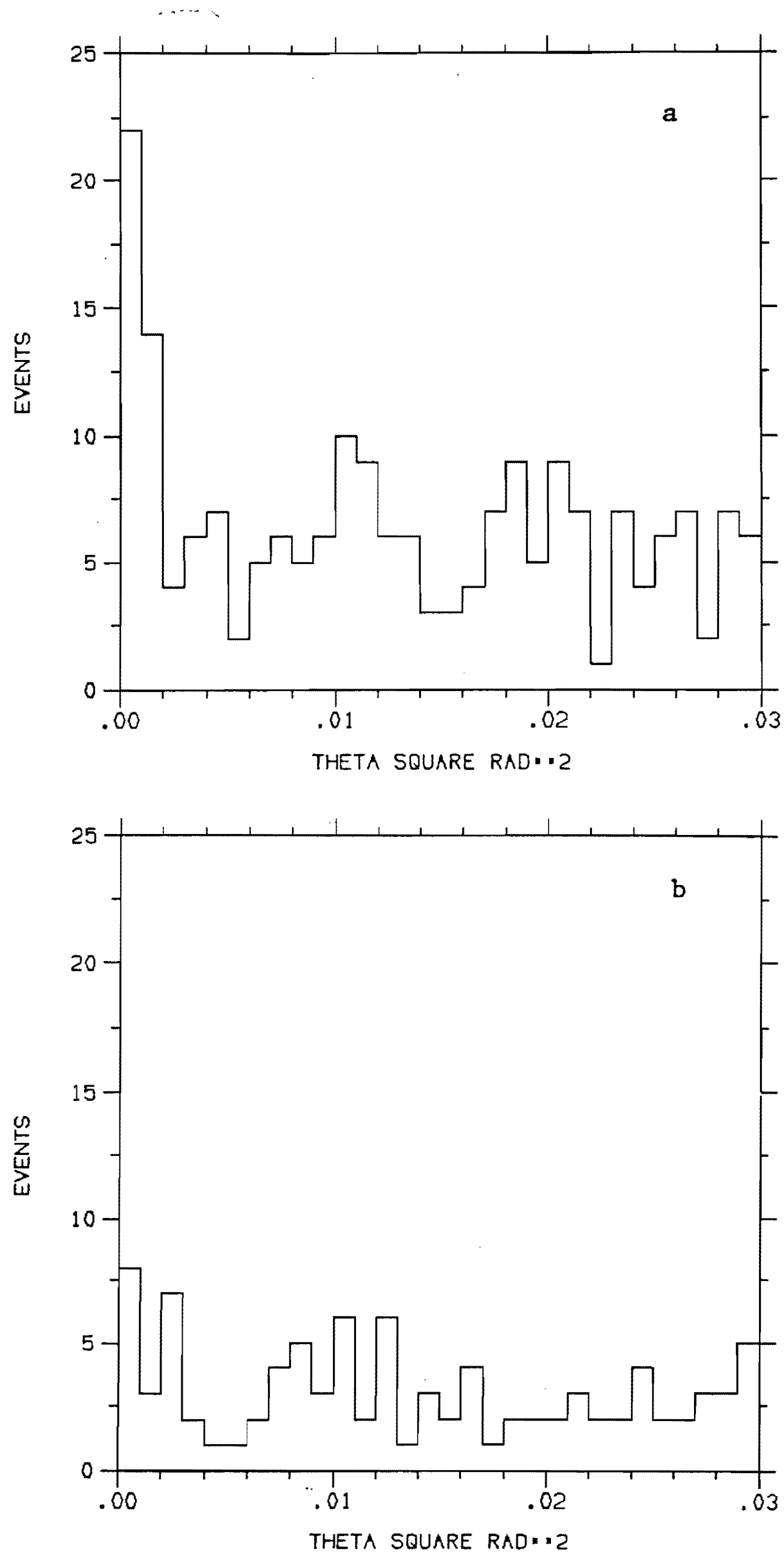

Figure 4.2.10 θ^2 distribution for antineutrino data in 1986. a) Electrons identified by the e/γ cut. b) Photons identified by the e/γ cut.

events to 174 (93) for the neutrino (antineutrino) sample. The θ^2 distributions for these events are shown in figures 4.2.9 and 4.2.10. The low angle peaks in the electron samples are striking. No sharp peaks are obvious in the photon distributions. The forward peaks in the electron distributions are due to the neutrino (antineutrino) electron elastic scattering events.

The same cuts were applied to the "stub" sample and the resulting distributions are shown in figures 4.2.11 and 4.2.12. The dE/dx distribution for the "stub" sample shows that it is composed of doubly ionizing particles, mostly photons. The θ^2 distribution for them looks similar to the background in the electron sample.

The events obtained through the analysis described in this chapter were later combined with previous data. The combined set of events was used for signal extraction and cross section determination.

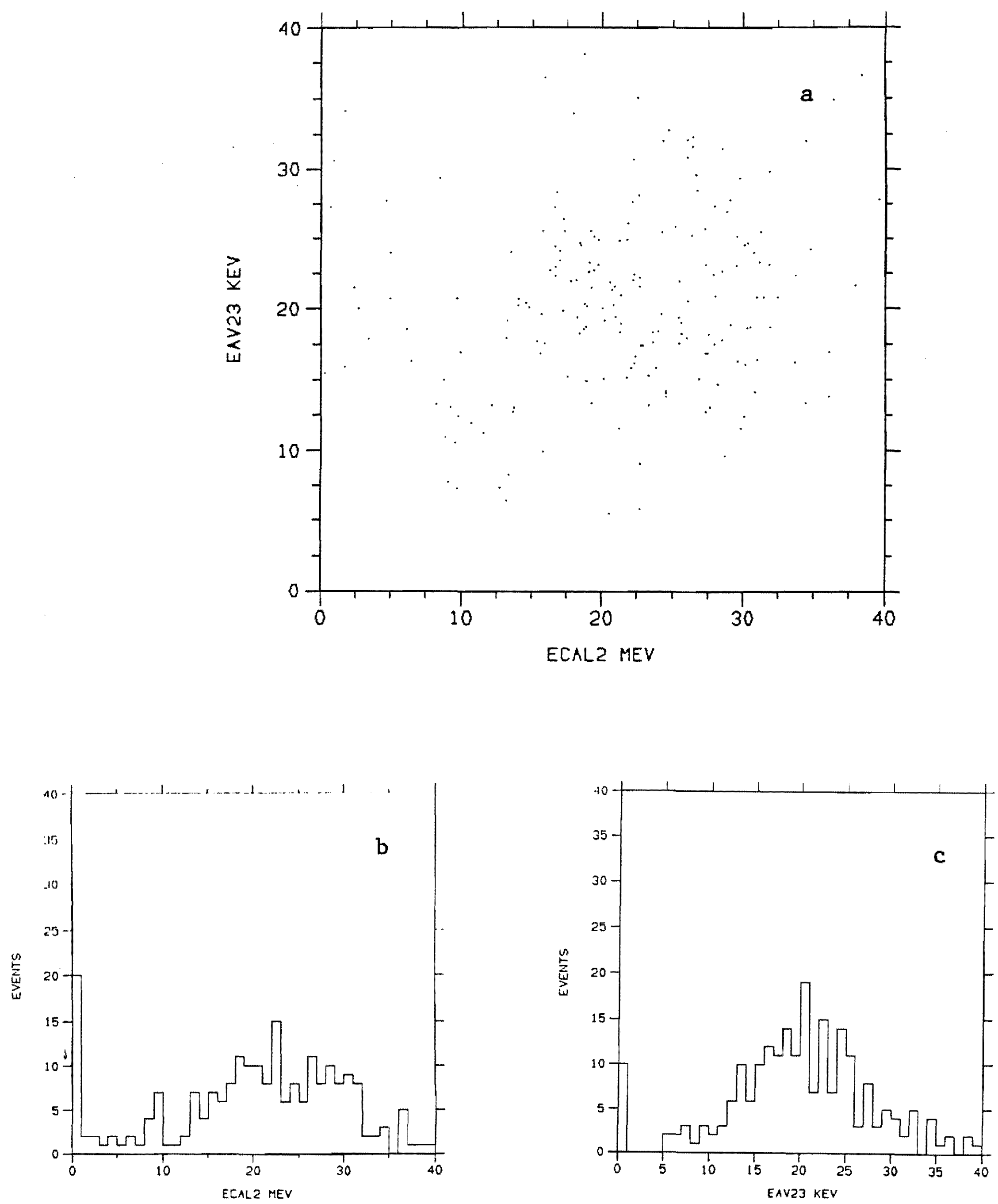

Figure 4.2.11 dE/dx distribution for stub data from 1986. a) Scatterplot of E_{cal2} and E_{av23}. b) Projection for E_{cal2}. c) Projection for E_{av23}

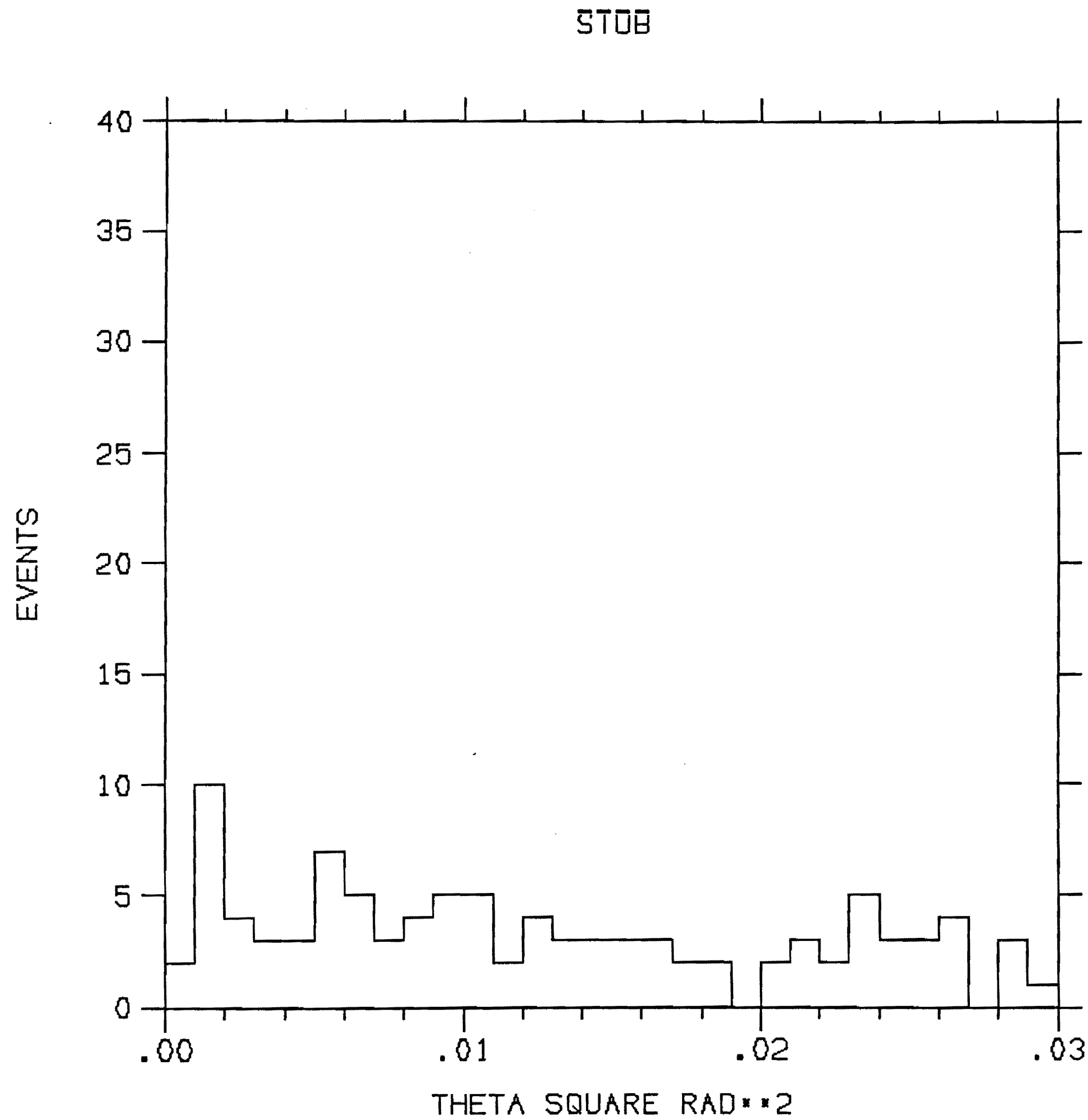

Figure 4.2.12 θ^2 distribution for stub data in 1986.

Chapter 5.

Normalization.

Measurement of the total incident neutrino/antineutrino flux was necessary for determination of $\nu_\mu e \rightarrow \nu_\mu e$ and $\bar{\nu}_\mu e \rightarrow \bar{\nu}_\mu e$ cross sections. The flux was indirectly measured by determining the reaction rates of quasielastic interactions, $\nu_\mu n \rightarrow \mu^- p$ and $\bar{\nu}_\mu p \rightarrow \mu^+ n$. These reactions had a simple topology in the detector; they have large cross sections in the energy range of this experiment; in addition, the differential cross sections [27,28] for these reactions are well understood and are independent of $\sin^2\theta_w$. These considerations led to the choice of quasielastic event rates as the normalization for this experiment.

1. Sample selection

A topological selection was used to isolate events containing long muons produced by the quasielastic interactions [29] following cuts were applied to obtain a sample of quasielastic events from the same data set that led to the elastic scattering events described in the previous chapter.

1) Events with a track longer than 20 modules, corresponding to muon energy greater than 350 MeV, were selected. This requirement made the selection insensitive to additional tracks in the same time cluster. It eliminated most charged pions since pions above this energy tend to scatter with high probability.

2) The muon track selected in (1) was required to be within 15^0 of the beam direction(see Fig. 5.1.1). This restricted the average Q^2 to be less than $0.2(GeV/c)^2$ making the proton track too short to be visible.

3) The procedure next examined scintillator multiplicity and energy distributions away from the event vertex inside a spatial cylinder (tube-cut) surrounding the track. The event was rejected if the average number of scintillators per plane was not close to unity and if the average energy per module was not consistent with dE/dx for a muon. The tube-cut got rid of showers or overlapping multi-track events.

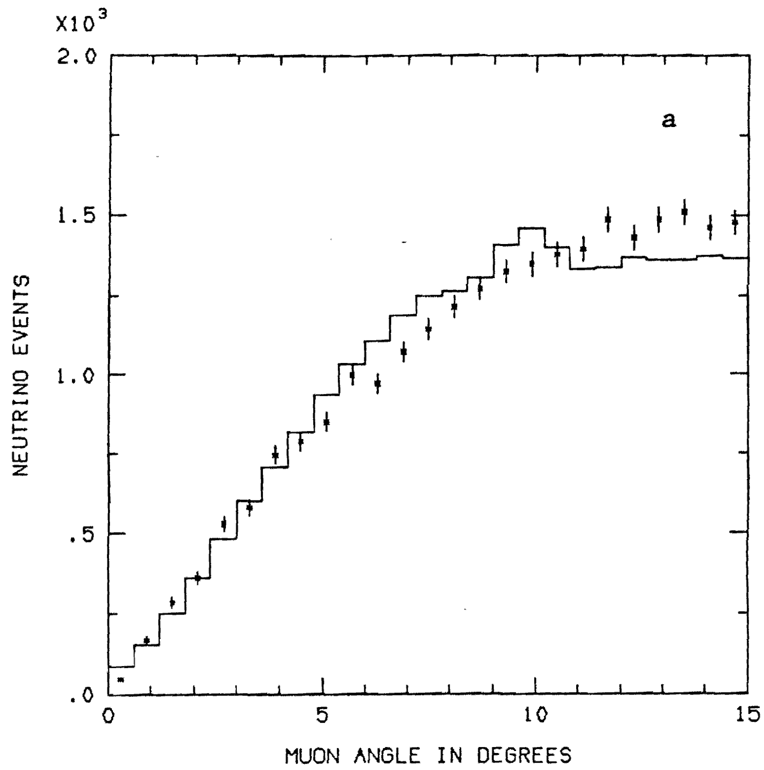

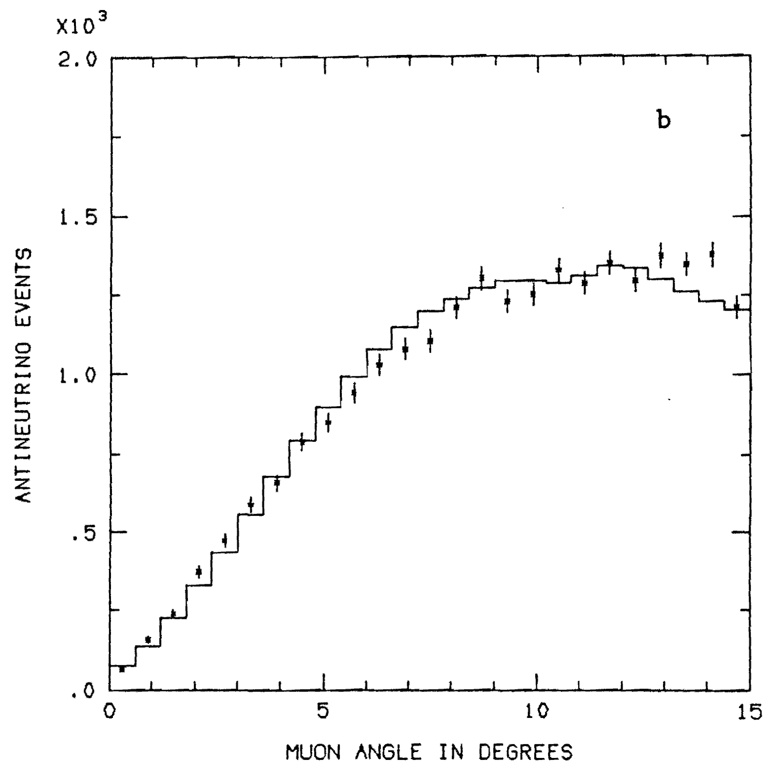

Figure 5.1.1 θ_μ for the normalization samples.(a) Neutrino data.(b) Antineutrino data. The solid histograms are Monte Carlo simulations.

Selection step	ν_μ	$\bar{\nu}_\mu$
Single track events	113201	60781
Run kills	108883	59744
Micro errors	105497	57744
Fiducial	102520	56761
$L > 20$ modules	53745	41112
$\theta_\mu < 15^0$	30186	26695
Tube cut	27007	25428

Table 5.1.1 Event selection for the quasielastic normalization

4) Event vertex was restricted to the same fiducial volume as in the electron analysis.

Table 5.1.1 summarizes the event selection. Since this sample was not limited by statistics, NUE, our primary production program, sampled only 1 out of 3 events for normalization to save computing time.

2. Backgrounds and corrections

ν_μ Channel	Fraction	in data	$\bar{\nu}_\mu$ Channel
$\mu^- p$(Signal)	0.563	0.598	$\mu^+ n$(Signal)
$\mu^- p \pi^+$	0.244	0.133	$\mu^+ n \pi^-$
$\mu^- p \pi^0$	0.068	0.063	$\mu^+ n \pi^0$
$\mu^- n \pi^+$	0.077	0.062	$\mu^+ p \pi^-$
Multi pion	0.024	0.020	Multi pion
$\mu^+ n$(Wrong sign)	0.024	0.124	$\mu^- p$(Wrong sign)

Table 5.2.1 Background fractions in the quasielastic sample

The primary backgrounds to quasielastic scattering were single pion inelastic charged-current interactions. Topological selection removed background channels exhibiting two (or more) visible charged tracks. The remaining single-pion and multipion backgrounds were calculated by Monte Carlo simulations and subtracted from the samples (see table 5.2.1). For more information about the Monte Carlo methods used in this experiment see Eric Stern's Ph. D. thesis [17]. The fraction of events in the two samples due to wrong-helicity neutrinos was calculated from the measured contaminations in the primary beams. Table 5.2.1 shows what fractions of the event sample were the different backgrounds.

Correction	ν_μ Channel	$\bar{\nu}_\mu$ Channel
Sampling fraction	1/3	1/3
Geometric acceptance	0.172	0.317
Tracking efficiency	0.85±0.02	0.86±0.05
Angle cut efficiency	0.98±0.02	0.98±0.03
Tube cut efficiency	0.974±0.010	0.986±0.010
Runs not processed	0.917	1.00
Total correction	0.128/3	0.263/3

Table 5.2.2 Quasielastic acceptance and efficiencies

The acceptances and efficiencies for the quasielastic samples are summarized in Table 5.2.2. They were determined by eye scan or by Monte Carlo calculations, and were averaged over the incident neutrino flux. The tracking efficiency was determined by eye scans of raw events entering the track-finding procedure in NUE. The tracking efficiency represents the ability of the event reconstruction program to find muon tracks in the angular range of interest. The inefficiency was due to PDT inefficiency, multiple scattering, and noise from crossing tracks. The tube cut efficiency was dominated by noise effects. It was measured by overlapping random data on Monte Carlo quasielastic events. The last factor in table 5.2.2 corrects for the data tapes that could not be analysed for normalization events due to computer processing errors, but were analysed for the electromagnetic showers.

	σ_ν	$\sigma_{\bar\nu}$	$\sigma_{\nu\bar\nu}$
Q.E. Efficiency			
Trackfinding	2%	2%	1%
Tube Cut	1%	1%	0%
Angle Cut	2%	2%	1%
Totals	2.9%	3.0%	1.4%
Misc. Factors			
Monte Carlo:			
Nuclear Scattering	1%	1%	1%
π–cross sections	10%	6%	7.5%
Multi-π cross sections	4%	3%	0%
π scattering	2%	2%	2%
Isospin mix	1%	1%	1%
M_A	1%	1%	0.5%
Pauli exclusion	2%	2%	2%
Fermi momentum	0%	1%	0%
Beam spectra	4%	2%	0%
Wrong helicity	0%	2%	0%
Totals	12.0%	8.1%	8.2%
Final Totals	12.3%	8.6%	8.3%

Table 5.2.3 Systematic errors for the quasielastic normalization

The excellent agreement between the Monte Carlo modeling and the data for the quasielastic analysis is demonstrated by Fig. 5.1.1 which shows the angular distribution of muons from the data and the Monte Carlo simulation which includes contributions from all backgrounds. The normalization samples were not limited by statistics, therefore only the systematic errors were considered important; they are shown in table 5.2.3. Some of the systematic errors were correlated between the neutrino and antineutrino nomalizations. The corrected numbers of quasielastic events were:

$$3.56 \times 10^5 Q.E. \text{ for the neutrino data}$$

and

$$1.73 \times 10^5 Q.E. \text{ for the antineutrino data.}$$

The flux averaged cross sections for the quasielastic interactions and the mean energies of the neutrino and antineutrino beams were also necessary for the final determination of the $\nu_\mu e \to \nu_\mu e$ and $\bar{\nu}_\mu e \to \bar{\nu}_\mu e$ cross sections. They were computed by numerical integration over the flux, $\phi_\nu(E_\nu)$, determined in chapter 2.

$$< \sigma_{QE} >= \frac{\int_{E_1}^{E_2} \sigma_{QE}(E_\nu)\phi_\nu(E_\nu)dE_\nu}{\int_{E_1}^{E_2} \phi_\nu(E_\nu)dE_\nu}$$

$$< E_\nu >= \frac{\int_{E_1}^{E_2} E_\nu\phi_\nu(E_\nu)dE_\nu}{\int_{E_1}^{E_2} \phi_\nu(E_\nu)dE_\nu}$$

where $E_1 = 0.2GeV$ and $E_2 = 5.0GeV$. The cross sections and flux were small below 0.2GeV, and the flux became negligible above 5.0GeV, therefore these limits in energy were considered satisfactory.

$< \sigma_{QE} >$ was found to be $(0.921 \pm 0.004) \times 10^{-38} cm^2$ for the neutrino channel and $(0.396 \pm 0.002) \times 10^{-38} cm^2$ for the antineutrino channel. $< E_\nu >$ was found to be $(1.272 \pm 0.022) GeV$ for the neutrino channel and $(1.285 \pm 0.022) GeV$ for the antineutrino channel.

Chapter 6.

E734 Neutrino Electron Scattering Data

The spectra of neutrinos and antineutrinos from 1981 and 1983 were compared to the spectra obtained in 1986 (see chapter 2 and Ref. 20). All components of the 1986 spectrum had the same shape in energy as the 1981-83 spectra. The total intensities were, nevertheless, different. The mean energy of the 1986 ν_μ ($\bar{\nu}_\mu$) beam was $1.273GeV$ ($1.285GeV$) which was compared to the value in 1981-83: $1.275GeV$ for ν_μ ($1.187GeV$ for $\bar{\nu}_\mu$). The flux averaged cross section for the quasielastic interaction used in the normalization for the 1986 ν_μ ($\bar{\nu}_\mu$) beam was $0.921 \times 10^{-38} cm^2$ ($0.396 \times 10^{-38} cm^2$) which was compared to the value in 1981-83: $0.918 \times 10^{-38} cm^2$ for neutrino the data (0.376×10^{-38} for the antineutrino data). The normalization for 1986 is described in chapter 5. The normalization for the 1981-83 data was: $6.54 \times 10^5 Q.E.$ for the neutrino data and $2.53 \times 10^5 Q.E.$ for the antineutrino data. When combined together , the mean energies and the cross sections appropriately weighted by the normalization, the normalization for the entire data set is expressed in the following numbers:

For neutrino data,

$$< E_\nu >= 1.274GeV$$

$$< \sigma_\nu(Q.E.) >= 0.919 \times 10^{-38} cm^2$$

$$N_\nu(QE) = 10.1 \times 10^5$$

and for the antineutrino data

$$< E_{\bar{\nu}} >= 1.227GeV$$

$$< \sigma_{\bar{\nu}}(Q.E.) >= 0.384 \times 10^{-38} cm^2$$

$$N_{\bar{\nu}}(QE) = 4.26 \times 10^5.$$

The systematic errors on the normalization are described in chapter 5. 35.1% (40.6%) of the neutrino (antineutrino) data was obtained in the 1986 run.

The analysis procedure used for 1986 data to obtain a sample of electromagnetic showers was identical to the procedure used for the 1981-83 data [18,19] except for the vertex cleanup procedure (see chapter 3). Instead of vertex cleanup, more eye scanning was done for the 1981-83 data. The normalization procedure was identical for all data sets.

	ν_μ		$\bar{\nu}_\mu$	
	1986	Old	1986	Old
Events	589	1545	403	959
Totals	2134		1362	
e/γ	1322		802	
$\theta^2 < 0.03$	898		572	

Table 6.1 Table shows the number of events belonging to each of the samples

Convinced that the spectra and the analysis methods were very nearly the same for all the data accumulated over the years and the errors well understood, we decided to add all the final samples of electromagnetic showers together and made likelihood fits to the resulting distributions. Table 6.1 shows the number of events from each sample and the final cuts.

1. Signal extraction for all data:

After all the analysis cuts, each shower event was characterized by four quantities: θ^2, the measured angle; E, total energy of the shower; E_{cal2}, measure of dE/dx in calorimeters, and E_{av23}, measure of dE/dx in PDTs. Distributions for these quantities are illustrated in the accompanying figures.

Likelihood fits can be made to any of these quantities, separately or simultaneously, to obtain the number of signal events. Nevertheless, since the angular, θ^2, and energy, E, distributions, obtained after the e/γ cut, showed the most obvious manifestations of the signal events, they were relied upon to extract the total number of signal events in both the neutrino and antineutrino data. To calculate

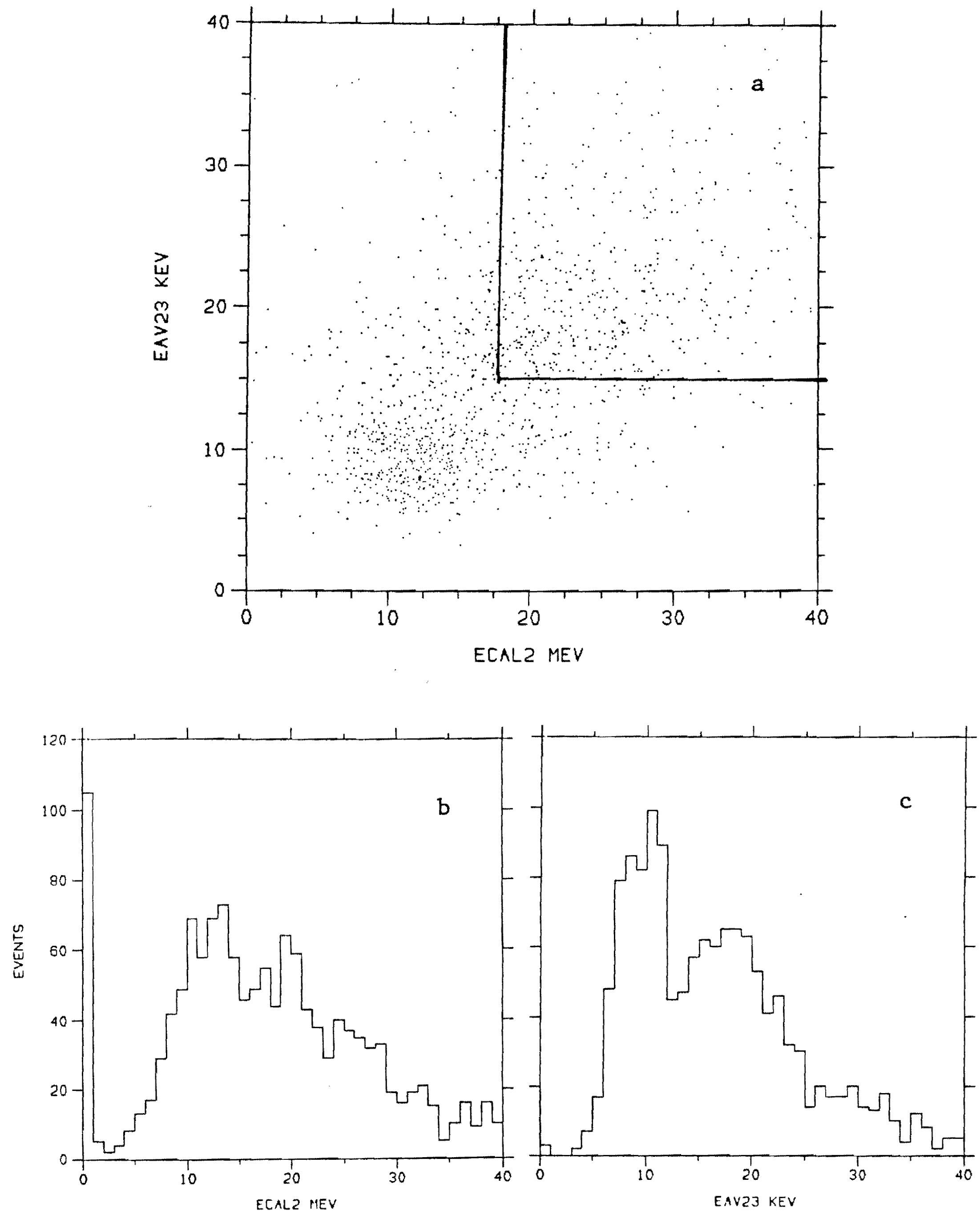

Figure 6.1.1 *dE/dx distributions for all neutrino data.* a) Scatterplot of E_{cal2}, measure of dE/dx in calorimeters and E_{av23}, measure of dE/dx in PDTs. The e/γ cut is displayed by the solid line. b) Projection for E_{cal2}. c) Projection for E_{av23}

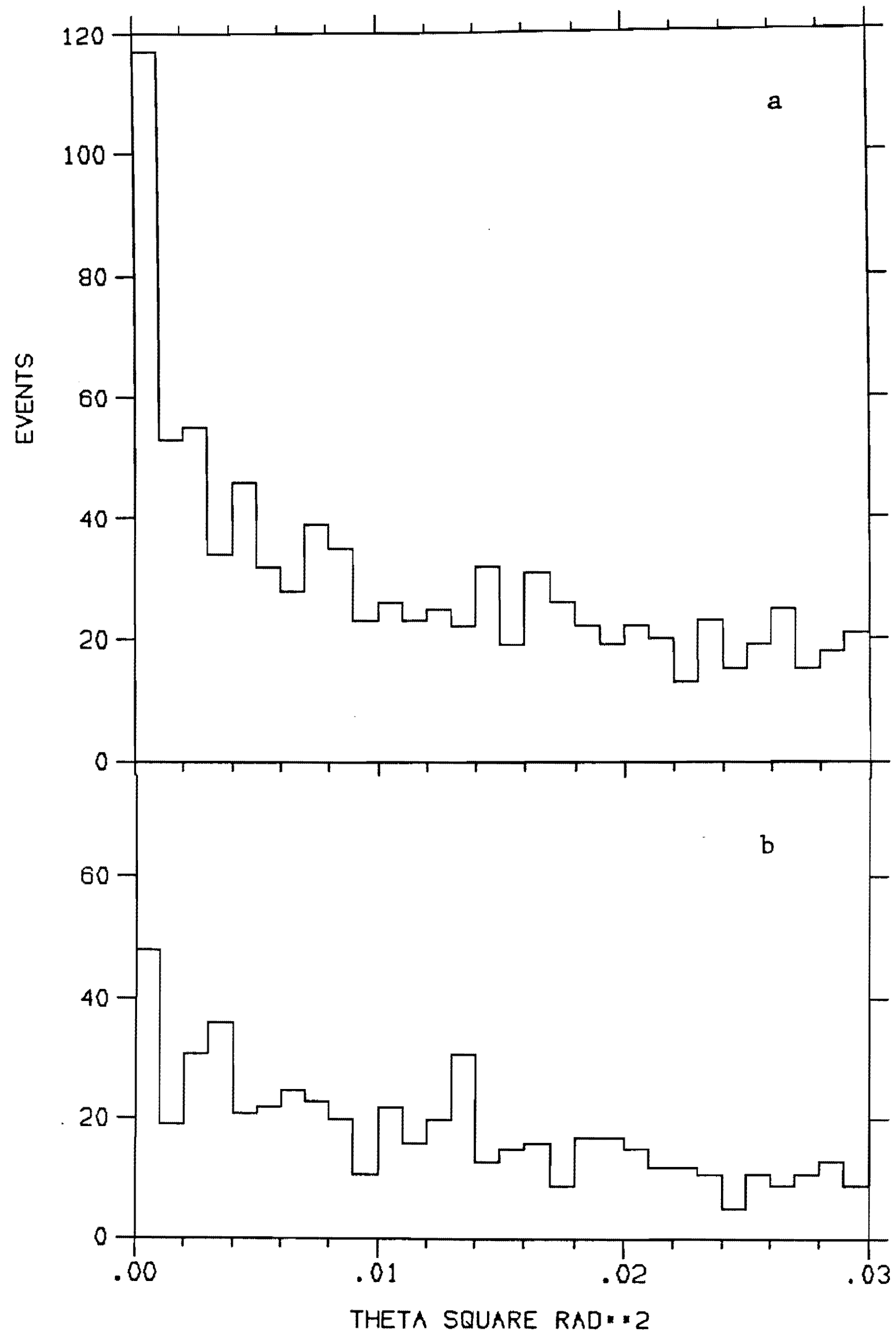

Figure 6.1.2 θ^2 distributions for all neutrino data. a) Electrons identified by the e/γ cut. b) Photons identified by the e/γ cut

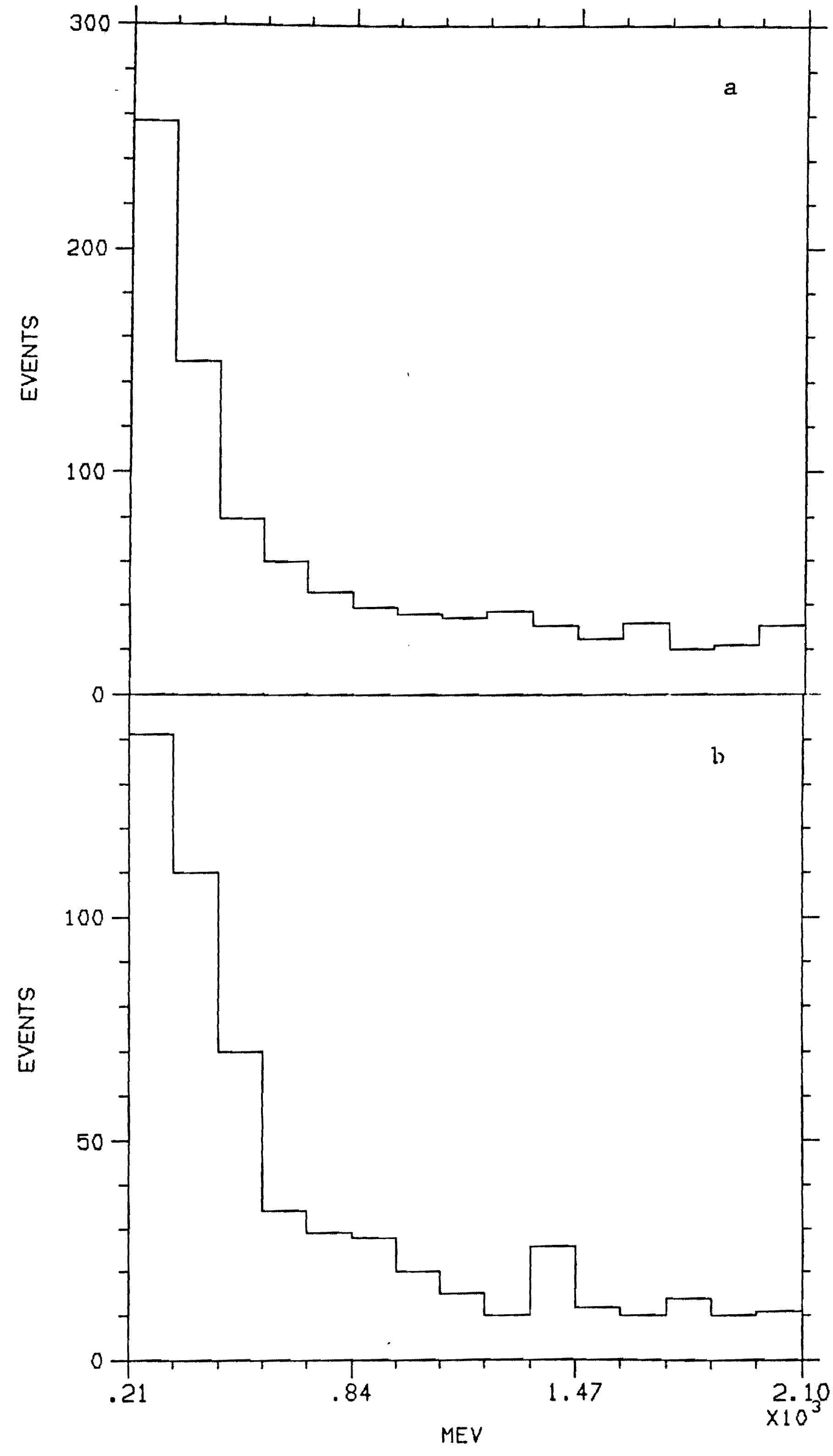

Figure 6.1.3 Energy distributions for all neutrino data. a) Electrons identified by the e/γ cut. b) Photons identified by the e/γ cut

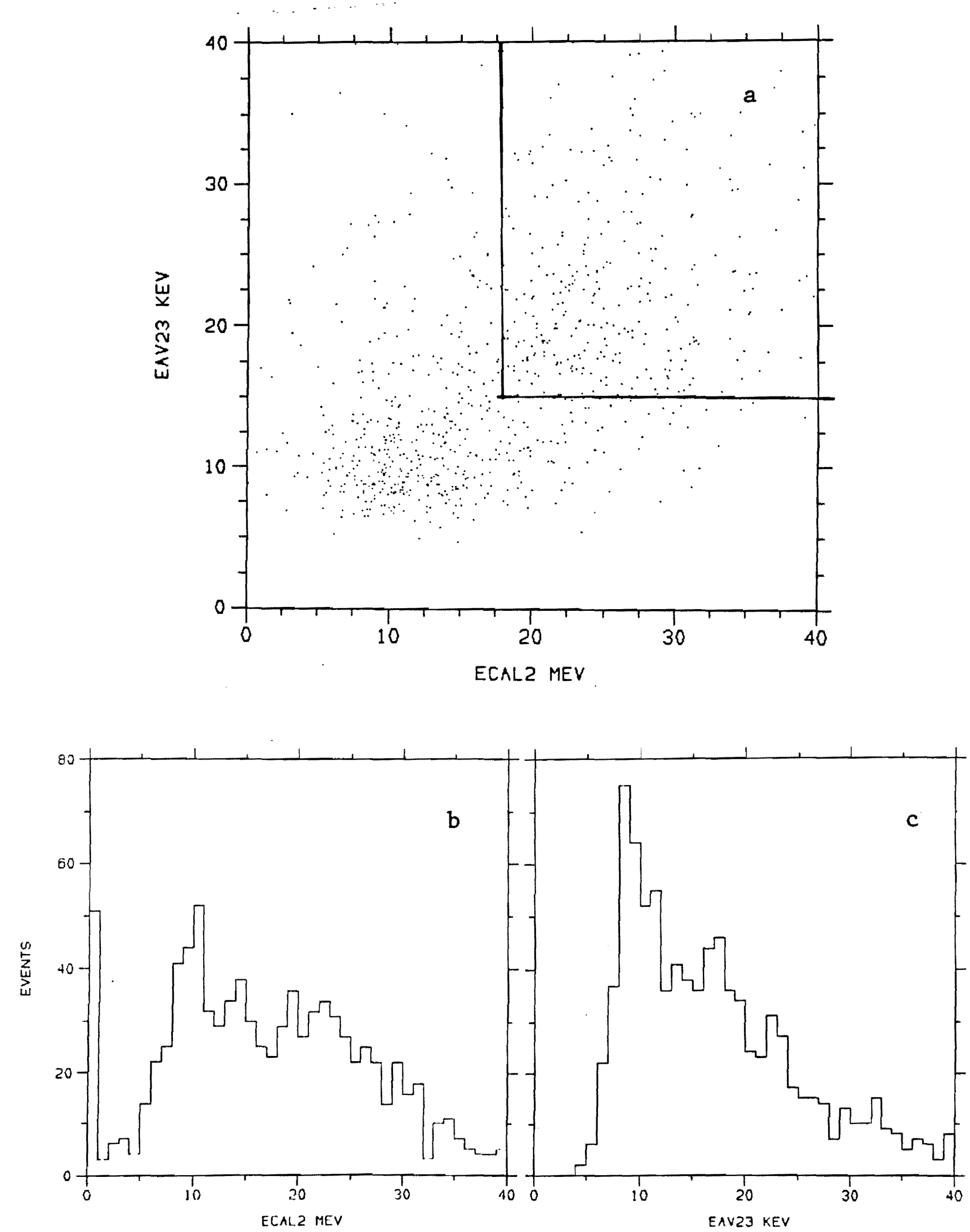

Figure 6.1.4 dE/dx distributions for all antineutrino data. a) Scatterplot of E_{cal2}, measure of dE/dx in calorimeters and E_{av23}, measure of dE/dx in PDTs. The e/γ cut is displayed by the solid line. b) Projection for E_{cal2}. c) Projection for E_{av23}

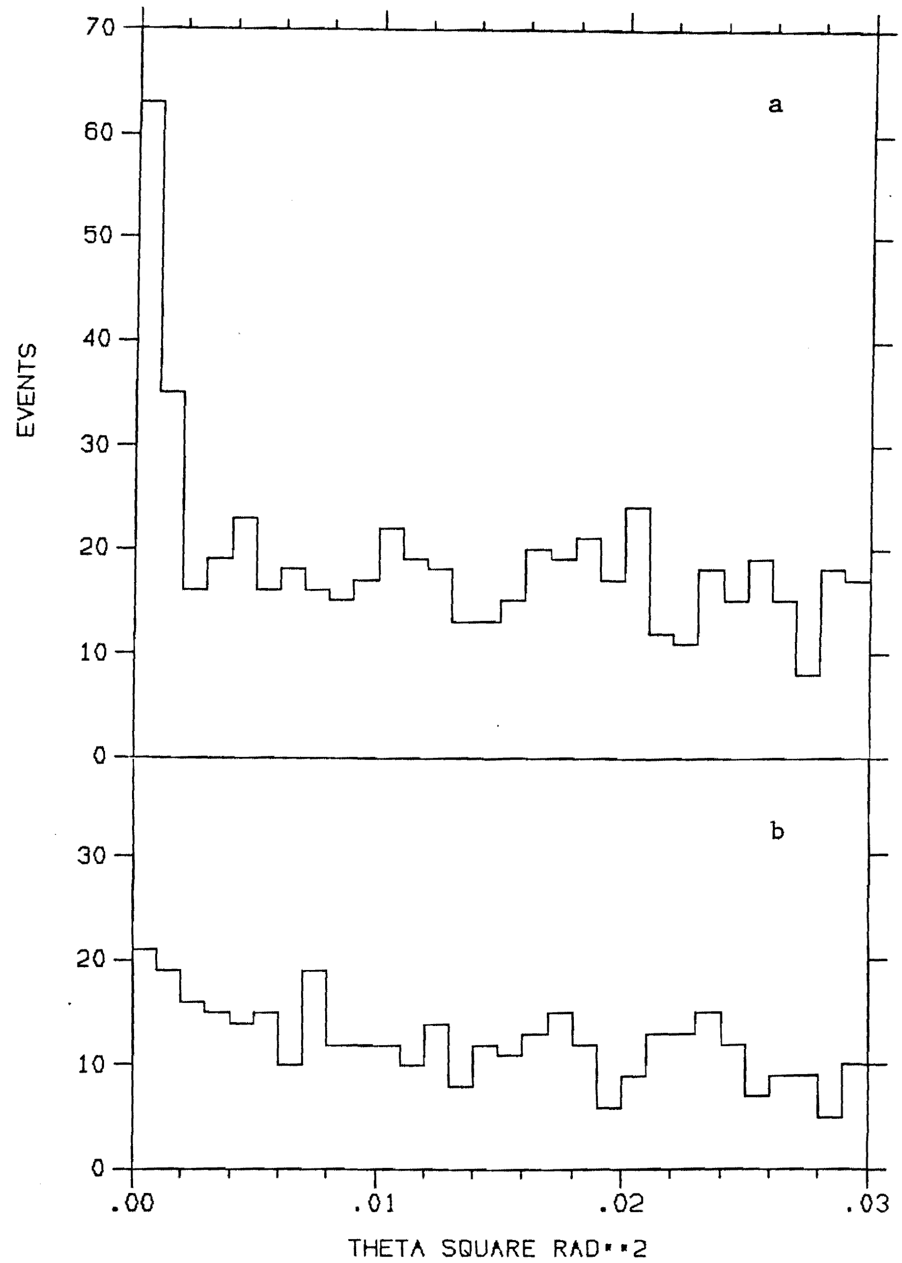

Figure 6.1.5 θ^2 distributions for all antineutrino data. a) Electrons identified by the e/γ cut. b) Photons identified by the e/γ cut

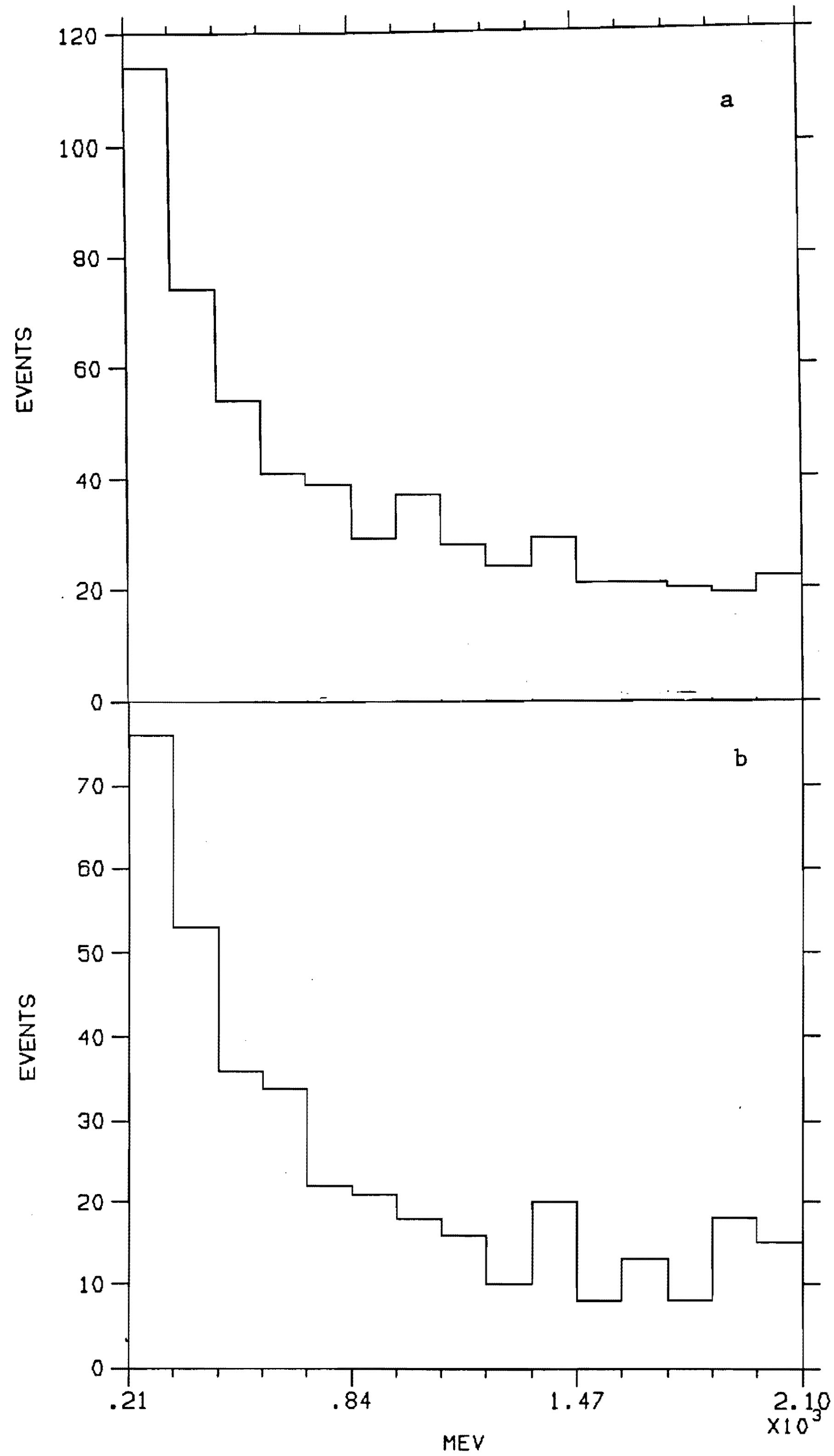

Figure 6.1.6 Energy distributions for all antineutrino data. a) Electrons identified by the e/γ cut. b) Photons identified by the e/γ cut

the number of signal events under the peak in the θ^2 distribution, it was necessary to know the exact distribution of the background. The θ^2 distribution was divided in two parts for background studies. The region above $0.01 rad^2$ did not contain much of the signal ($< 7\%$); therefore it was considered the background region and the region below was the signal region. The energy and dE/dx distributions of the background region were consistent with the assumption that it was mostly made of either photons from pion decays or electrons or positrons from the electron neutrino quasielastics, $\nu_e n \rightarrow ep$ for the neutrino data and $\bar{\nu}_e p \rightarrow en$ for the antineutrino data. Presence of low energy hadrons was studied by eye scan[18] and by looking at events that had the mean number of PDT hits per plane less than 1.3, since low energy hadrons were not expected to shower[19]. The fraction of low energy hadronic events in the background was negligible for the final sample, and the θ^2 distribution of these events did not differ significantly from the distribution due to π^0 decays.

(1) The $\pi^0 \rightarrow \gamma\gamma$ background: The π^0s produced in coherent ($\nu N \rightarrow \nu N \pi^0$) and incoherent ($\nu n \rightarrow \nu n \pi^0$ and $\nu p \rightarrow \nu p \pi^0$) neutral current interactions were the main cause of this background[30]. Monte Carlo studies indicated that the coherent production contributed only 1/6 of the total π^0 background. Also the energy and θ^2 distributions of photons from all three channels were so similar for our regions of interest that the $\nu n \rightarrow \nu n \pi^0$ channel was considered an adequate representation for all. The photons produced from the π^0 decays were flatly distributed in θ^2 below $0.03 rad^2$ and were less than $1000 MeV$ in energy, but the angular resolution of the PDT filter in conjunction with the $0.20 rad$ cut on the PDT filter angle resulted in a sloped θ^2 distribution. PDT filter angular resolution in each view of the detector was calculated to be $\frac{40.0 \pm 5.0 mrad}{\sqrt{E/GeV}}$ by Monte Carlo simulations. The much finer determination of the angle (see chapter 4) was done after the $0.20 rad$ cut on the PDT filter angle. The PDT filter resolution and the $0.20 rad$ cut combined to reject events that were below $0.20 rad$ causing a decreased efficiency for events at large angles[19]. The θ^2 distribution of background due to π^0s was thus determined to be sloped for both neutrino and antineutrino data. Monte Carlo generator (see

appendix 2) events were generated and the background distributions were obtained by taking account of all smearing effects in the detector and measurements.

(2) Background due to electron neutrino quasielastics (e^-p and e^+n): These backgrounds were also analysed using generator level Monte Carlo simulations and smearing due to the detector resolution. The θ^2 distribution for the electron/positron from these events had a dip in the forward direction (Fig. 6.1.7). For $\theta^2 > 0.01$ the distribution showed the same slope behaviour – due to the PDT filter – as the π^0 background. The dip in the forward direction was because of the Pauli exclusion principle: most of the nucleons in the detector were bound in low energy quantum states inside nuclei (Carbon); the forward events were low Q^2 events – the energy transfered by the lepton to the nucleon was small – and so the final state nucleon for these events also had low energy; if a particle produced in a reaction would end up in a quantum state already fully occupied, then the reaction is forbidden; therefore the cross section for the low Q^2 quasielastic events was reduced. Details of the modeling of Pauli suppression are in Eric Stern's Ph.D. thesis (see Ref. 17 and Ref. 27). The shape of the θ^2 distribution was affected mainly by the acceptance in Q^2 (i.e. which region of Q^2 was present in the final sample of events). For the neutrino channel, since the proton left visible energy at the vertex, the vertex cut of $30MeV$ was responsible for the nonuniform acceptance in Q^2. This was investigated by making cuts on the energy of the final state proton. For the antineutrino channel, lack of sufficient modeling for the neutron in the detector made such investigation impossible; assumption of uniform acceptance, finally used, was only approximately correct because during eye scanning some events were rejected, the neutron becoming visible by interacting in the detector (Fig. 6.1.8). The θ^2 distribution was also weakly dependent on the axial vector mass, M_A, and the nuclear scattering model – the final state nucleon scattered off other nucleons in the nucleus sometimes causing several nucleons to escape from the nucleus and appear as tracks near the vertex[17].

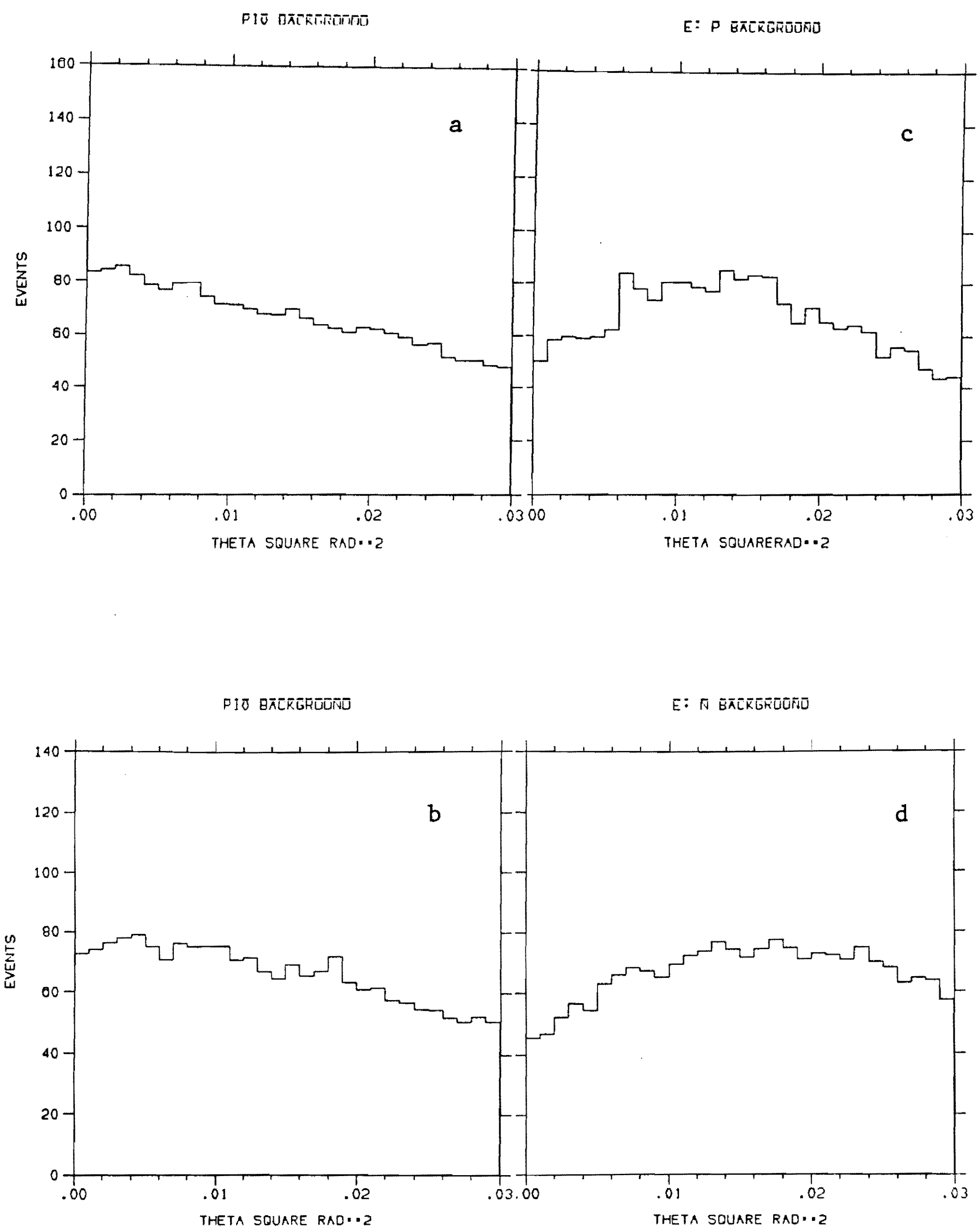

Figure 6.1.7 The four background distributions after taking account of all smearing effects. (a) $\nu_\mu n \rightarrow \nu_\mu n \pi^0$ (b) $\bar{\nu}_\mu n \rightarrow \bar{\nu}_\mu n \pi^0$ (c) $\nu_e n \rightarrow e^- \ p$ (d) $\bar{\nu}_e p \rightarrow e^+ \ n$

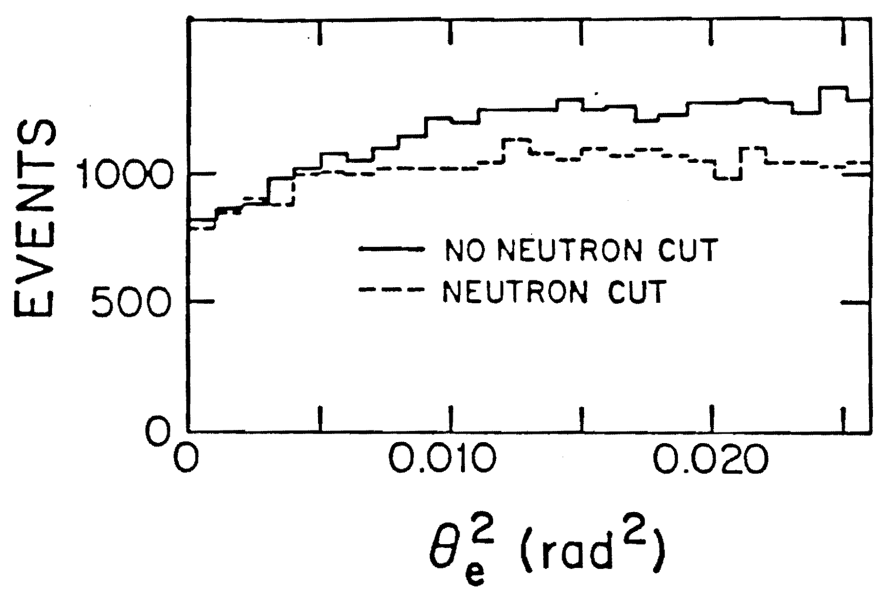

Figure 6.1.8 Study of the θ^2 distribution of $\bar{\nu}_e p \to en$ by making cuts on the energy of the neutron

The θ^2 distribution of the two backgrounds thus established, it was judged most desirable to use the measured energy distribution of the data above $0.01 rad^2$, the background region, as the model for all of the background.

The true background distributions were some combination of the distributions from the two backgrounds. It was necessary to determine the fraction of the background contributed by each of the background channels. The electron neutrino beam fluxes, determined in chapter 2, were used to calculate the fraction of the background due to the quasielastics. The acceptance for these events was computed by a full Monte Carlo simulation of these events in the detector and by taking the events through all the electron analysis cuts. The calculation was done by integrating the flux folded by the cross sections and multiplying by the total acceptance. The fraction of e^-p's (e^+n) expected in the neutrino (antineutrino) data, f_{ep} (f_{en}), was 0.23 ± 0.12 (0.41 ± 0.15). The errors on these numbers were large due to uncertainties in acceptance. Therefore, when the final fits to the electron data were made, the ep/en fraction was varied within its experimental errors to obtain the best fit to the $E - \theta^2$ distribution.

The final numbers of elastic scattering signal events were obtained by a maximum likelihood fit in two variables, θ^2 and energy. Signal and background distributions were fit to the data using a log-likelihood function. The signal event distributions were generated from the full Monte Carlo which took account of resolution, acceptance, inefficiency effects and effects due to noise from unrelated events in the same time cluster. Unrelated events were events chosen at random from the raw data. They were overlaid on the Monte Carlo events to simulate detector noise and inefficiencies. The θ^2 distributions for the backgrounds were generated by producing the events at the Monte Carlo generator level, smearing them according to the resolution of the detector, and making the electron analysis cuts, as described in the previous paragraphs. The energy distribution for both channels in the background was modeled from the energy distribution of the data for $\theta^2 > 0.01 rad^2$, the background region where the number of signal events was expected to be small. The likelihood function for the two dimensional distribution was obtained by assuming the probability distribution for each bin to be Poissonian.

$$\Phi = \prod_{ij} P_{\bar{n_{ij}}}(n_{ij})$$

where $P_{\bar{n}}(n)$ is the Poisson distribution:

$$P_{\bar{n}}(n) = \frac{e^{\bar{n}}\bar{n}^n}{n!}.$$

The log-likelihood function is expressed as:

$$ln\Phi = \sum_{ij} -\bar{n}_{ij} + n_{ij}ln(\bar{n}_{ij}) - ln(n_{ij}!)$$

where n_{ij} is the number of events in element ij for the data and $\bar{n}_{ij}$ is the expected number of events in the element:

$$\bar{n}_{ij} = N_s S_{ij} + N_b((1 - f_{(ep/en)})G_i + f_{(ep/en)}Q_i)E_j$$

where N_s is the number of signal events and N_b is the number of background events. S_{ij}, G_i, Q_i, E_j are normalized distributions that model the signal, photons from pion decay, quasielastics, and the energy distribution of the background, respectively. The indices, i and j, run over bins in the two variables, θ^2 and energy.

The maximum likelihood fits were performed by minimizing the negative of the log-likelihood (maximizing the total probability) using the FORTRAN minimization package, MINUIT[31]. The number of signal events, N_s, and the number of background events, N_b, was allowed to vary to give the best fit. The quasielastic fraction was also varied within its experimental errors, determined from studies of the electron neutrino flux. The best fits were obtained for $f_{ep} = 0.09$ and $f_{en} = 0.55$. The fits are displayed in figures 6.1.9, 6.1.10, 6.1.11, and 6.1.12. The number of signal events were:

$$N_s(\nu_\mu e \to \nu_\mu e) = 159.5 \pm 17.3[stat] \pm 3.7[syst]$$

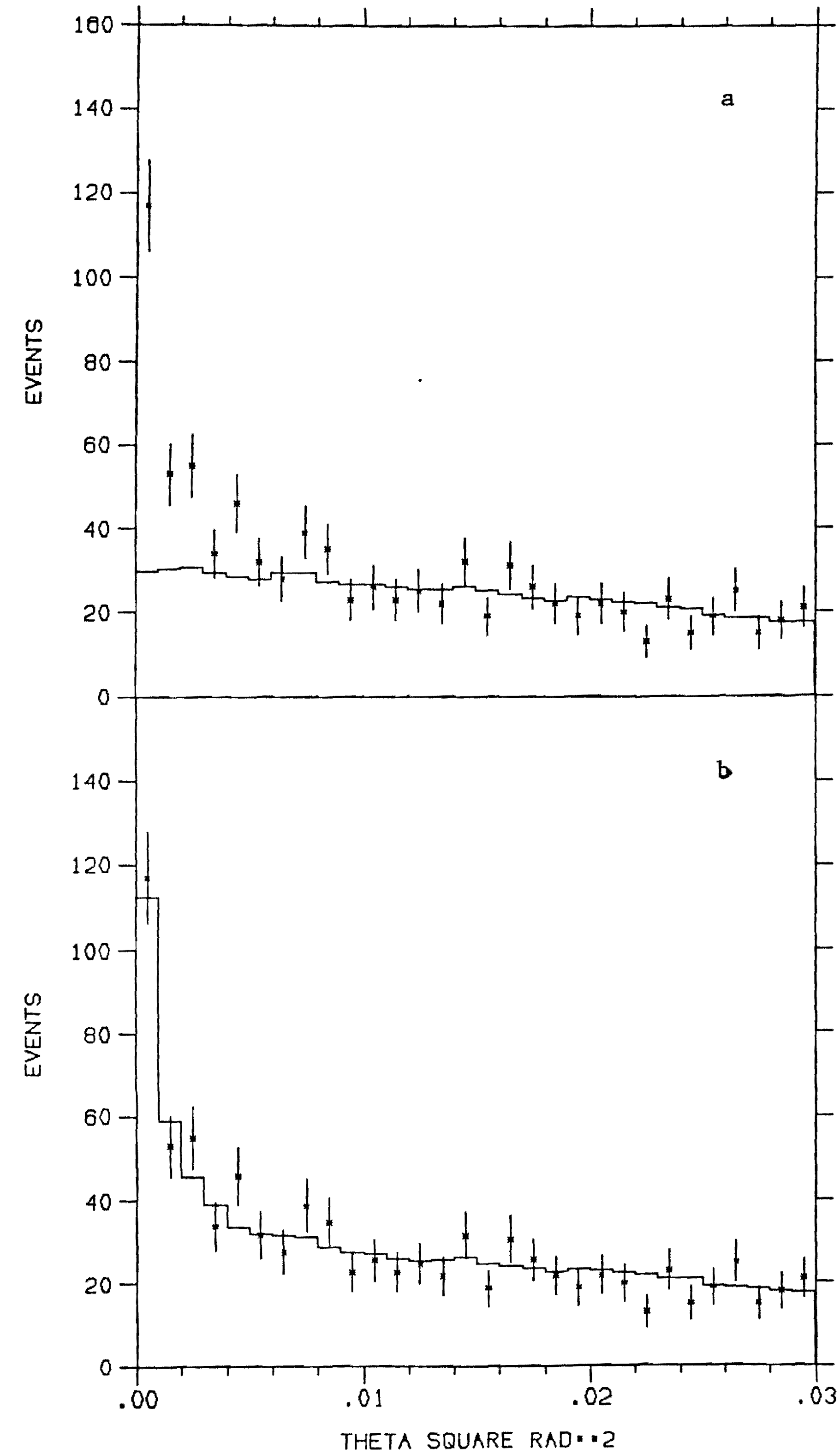

Figure 6.1.9 Fit to the θ^2 distribution for the ν_μ data. (a) Total background only. (b) Background and signal

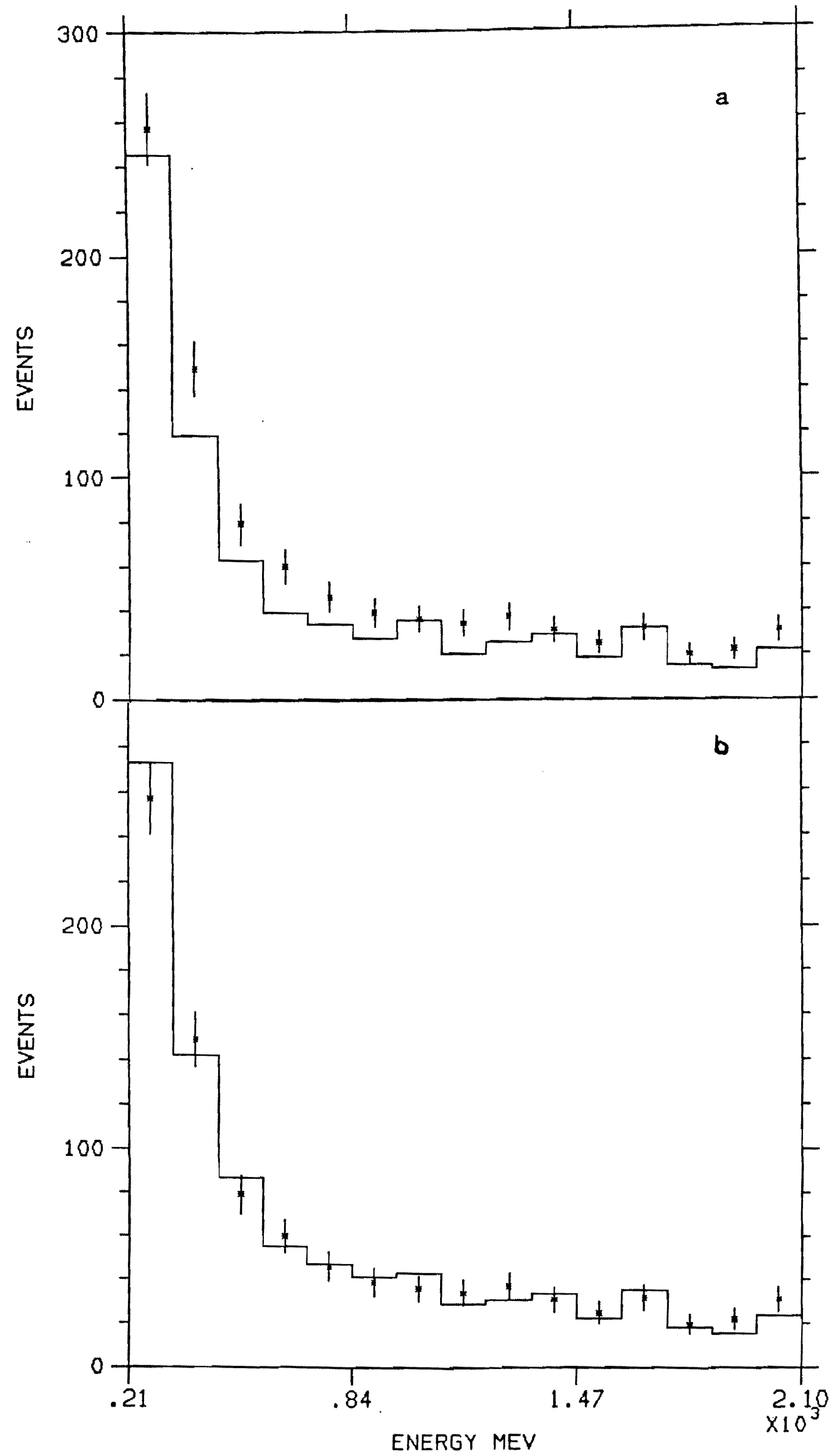

Figure 6.1.10 Fit to the energy distribution for the ν_μ data. (a) Total background only. (b) Background and signal

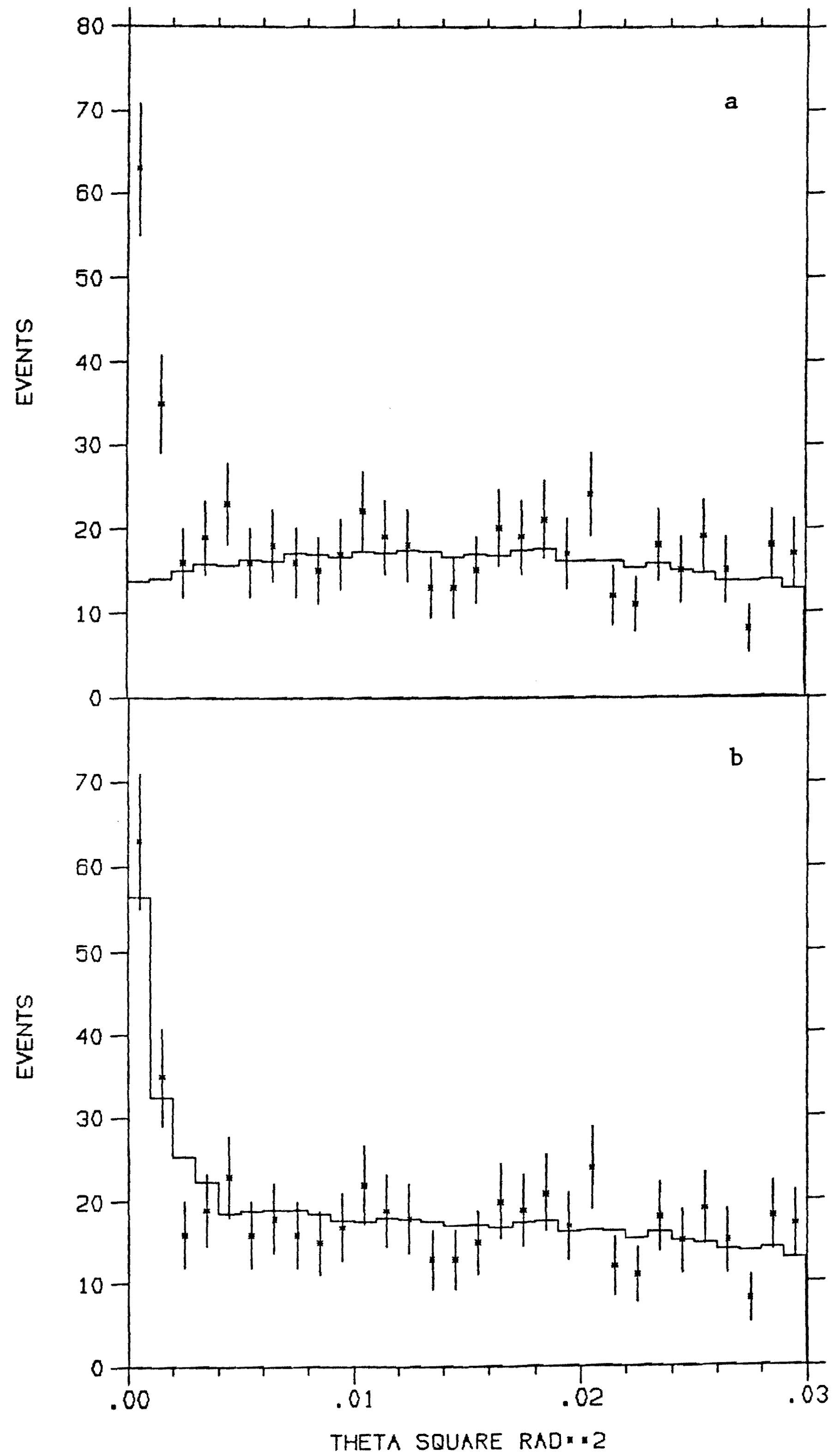

Figure 6.1.11 Fit to the θ^2 distribution for the $\bar{\nu}_\mu$ data. (a) Total background only. (b) Background and signal

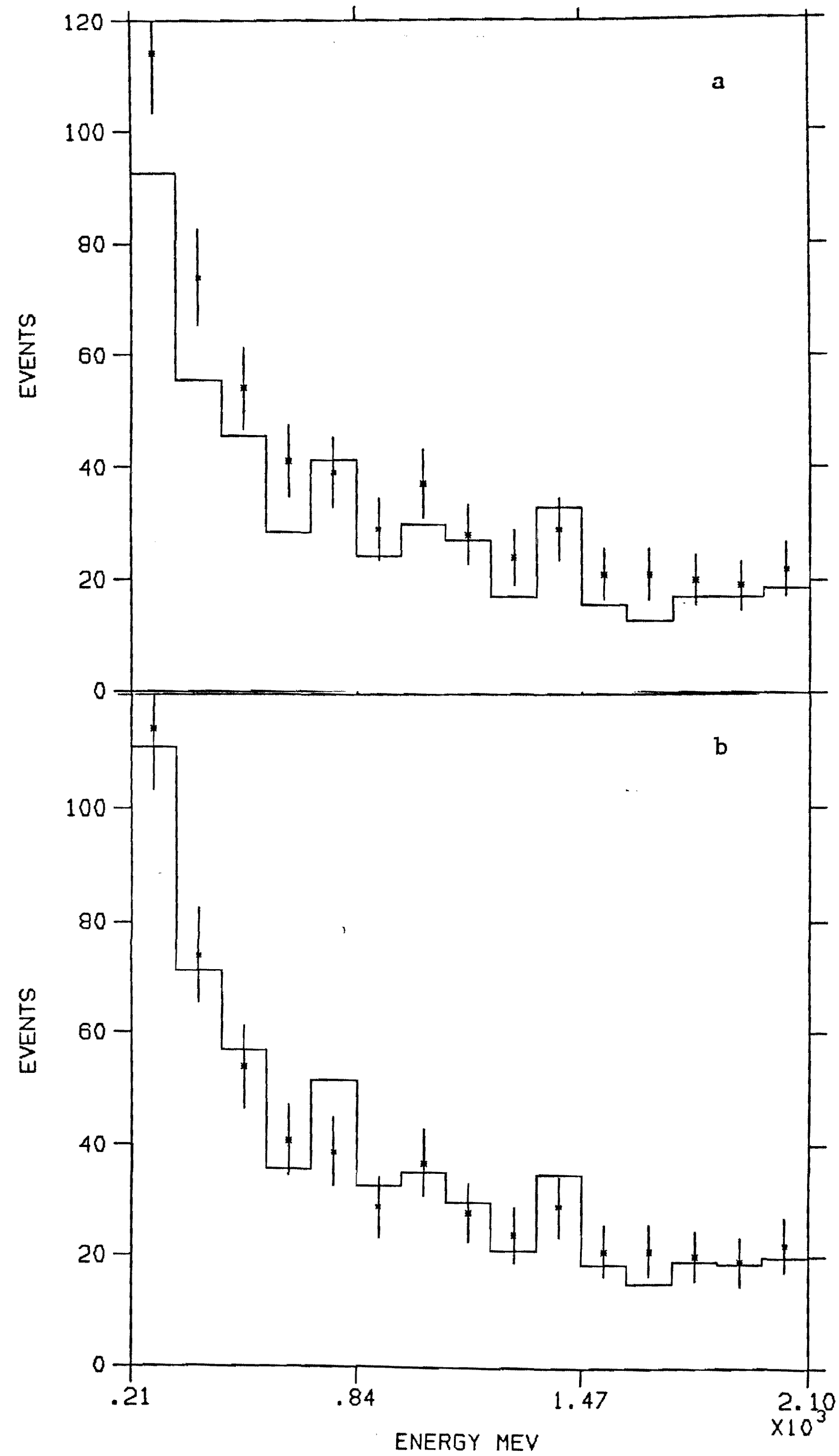

Figure 6.1.12 Fit to the energy distribution for the $\bar{\nu}_\mu$ data. (a) Total background only. (b) Background and signal

	ν_μ channel	$\bar{\nu}_\mu$ channel
Signal	$159.5 \pm 17.3[stat]$	$96.7 \pm 13.2[stat]$
$f_{ep/en}$	2.2%	4.5%
Slope	0.6%	0.8%
$Q^2(e^-p, e^+n)$	0.3%	1.2%
e^-p, e^+p model	0.2%	1.1%
Totals	2.3%	4.9%
Result	$159.5 \pm 17.3 \pm 3.7$	$96.7 \pm 13.2 \pm 4.7$

Table 6.1.1 Systematic errors in signal extraction

and

$$N_s(\bar{\nu}_\mu e \rightarrow \bar{\nu}_\mu e) = 96.7 \pm 13.2[stat] \pm 4.7[syst]$$

The systematic errors for signal extraction had four sources: the fraction of the background that was quasielastics, the Q^2 region of the quasielastics, the slope effect due to the PDT filter, and details of the modeling of the quasielastics which included choice of M_A and nuclear scattering. A number of different fits were made by changing the modeling of the background; parameters that affected the shape of the distributions were varied within their errors. Table 6.1.1 shows the various contributions to the total systematic error. The total systematic error is computed by adding the various contributions in quadrature.

A number of different fits were also made with different choices for the bins. The fits had some dependence on the binning in θ^2 and energy, but this dependence was considered entirely statistical. Bin width that corresponded to two standard deviations in angular resolution was chosen as the best representation of data.

2. Acceptances and efficiencies

The number of signal events had to be corrected for losses due to the various cuts in the analysis. Many of the cuts were overlapping; for example, the PDT filter rejected events with less than $100MeV$ energy, and later events with less than $210MeV$ were rejected. Therefore, the largest losses in the analysis were considered first. A list of each of the losses follows:

(1) Acceptance ($A_{210 \to 2100}$) : The energy cut was the largest loss. The loss due to this cut was evaluated by generating a large number of generator level Monte Carlo events, smearing them by the detector resolution, and applying the energy cut. The acceptance was the fraction of events that passed this cut. The acceptance factor depended weakly on the value of the Weinberg angle. Therefore when the value of $\sin^2\theta_w$ was finally evaluated the functional dependence of the acceptance was used. For convenience the acceptance was normalized to that for $\sin^2\theta_w = 0.225$ which was:

for neutrino data,

$$A_{210 \to 2100} = 0.710 \pm 0.001 \pm 0.030$$

for antineutrino data,

$$A_{210 \to 2100} = 0.710 \pm 0.001 \pm 0.010$$

The statistical error reflects the number of Monte Carlo events used for the determination.

(2) Software filters and PDT filter angle cut: For the 1986 data there were three steps in the software filter: the PDT filter, the vertex cleanup procedure, and the $\theta < 0.20rad$ cut on the PDT filter angle. Detector inefficiencies and noise due to unrelated events caused the software filter to reject some genuine electron events. Also, though the signal events were expected to have angles much less than $0.20rad$, the PDT filter sometimes miscalculated the angle due to unrelated tracks in the same time cluster. The efficiency of the software in finding electron shower events was calculated by passing Monte Carlo generated electron events. These were events generated with the full Monte Carlo which contained models for the PDT and calorimeter inefficiencies. In addition, randomly selected data

events from two different running periods were overlaid on the Monte Carlo events. The efficiency for the software filter was the fraction of events selected from events that were within the energy cut and the fiducial volume. The calculation was done for various combinations of the two sets of overlay events and detector element inefficiencies to understand the systematic error. The efficiency from the PDT filter and the vertex cleanup procedure were combined. It was evaluated to be: for the neutrino data,

$$\epsilon_{PDT+VERT} = 0.843 \pm 0.015 \pm 0.018$$

and for the antineutrino data,

$$\epsilon_{PDT+VERT} = 0.934 \pm 0.014 \pm 0.017.$$

The efficiency due to the $0.20rad$ cut was evaluated to be: for the neutrino data,

$$\epsilon_{\theta<0.2} = 0.987 \pm 0.004 \pm 0.004$$

and for the antineutrino data,

$$\epsilon_{\theta<0.2} = 0.974 \pm 0.009 \pm 0.010.$$

Above numbers are only for the 1986 data. These efficiencies had to be combined with the efficiencies obtained for the data from 1981-83[18,19]. The efficiencies were weighted according to the normalization (see chapter 5), and added together; the errors were propagated. The vertex cleanup procedure was not used for analysis of the data from 1981-83. The PDT filter and the $0.20rad$ cut was, nonetheless, the same for both data; therefore the systematic error from the PDT filter and the angle cut were correlated between the two data sets.

Table 6.2.1 shows how the efficiencies were combined. The sofware inefficiency for the entire data set was: for the neutrino data,

$$\epsilon_{soft} = 0.852 \pm 0.007 \pm 0.013$$

	1986	Old	σ_{86-old}
Fraction of	0.35	0.65	
total data	0.41	0.59	
ϵ_{PDT}	†	$0.882 \pm 0.005 \pm 0.012$	Full
		0.933 ± 0.015	correlation
$\epsilon_{PDT-VERT}$	$0.843 \pm 0.015 \pm 0.018$	N.A.	
	$0.934 \pm 0.014 \pm 0.017$		
$\epsilon_{\theta<0.20}$	$0.987 \pm 0.004 \pm 0.004$	$0.978 \pm 0.003 \pm 0.003$	Full
	$0.974 \pm 0.009 \pm 0.010$	$0.982 \pm 0.001 \pm 0.02$	correlation
ϵ_{soft}	$0.832 \pm 0.015 \pm 0.018$	$0.863 \pm 0.006 \pm 0.012$	0.012
	$0.910 \pm 0.016 \pm 0.019$	$0.916 \pm 0.015 \pm 0.02$	0.020
ϵ_{soft}	ν_μ $0.852 \pm 0.007 \pm 0.013$		
All data	$\bar{\nu}_\mu$ $0.914 \pm 0.011 \pm 0.020$		

Table 6.2.1 Software filter inefficiencies. The upper number in each row is for neutrino data; the lower is for antineutrino data. † combined in $\epsilon_{PDT-VERT}$

and for the antineutrino data,

$$\epsilon_{soft} = 0.914 \pm 0.011 \pm 0.020.$$

(3) Eyescan efficiency: For the 1986 data full Monte Carlo events, generated as described in the previous paragraph and taken through the analysis procedure as if real events, were randomly inserted between real events and printed on the micro fiche which were doubly scanned by physicists. The scanning efficiency (ϵ_{eye1}) was determined as the fraction of the Monte Carlo events found by the scanners. A second scan, super-scan, was conducted on the reduced sample. The super-scan was conducted separately by three physicists, two on one third of the data and one for the whole set. For purposes of this thesis, the efficiency of the single person super-scanning the complete reduced set was used as the efficiency of the super-scan (ϵ_{eye2}).

for neutrino data,

$$\epsilon_{eye1} = 0.993 \pm 0.001$$

$$\epsilon_{eye2} = 0.992 \pm 0.002$$

and for antineutrino data,

$$\epsilon_{eye1} = 0.975 \pm 0.004$$

$$\epsilon_{eye2} = 0.989 \pm 0.005$$

where the errors are entirely statistical. The scan for all the data was carried out in the same manner; therefore the scanning efficiencies from the 1986 data and the 1981-83 data were weighted according to the quasielastic normalization and combined to yield the scanning efficiencies for all of the data. The efficiencies from the first and the second scan were also combined. For all the neutrino data,

$$\epsilon_{eye} = 0.980 \pm 0.0022$$

and for all the antineutrino data,

$$\epsilon_{eye} = 0.950 \pm 0.0063$$

(4) The vertex energy cut: This was a small correction which was computed by the full Monte Carlo simulation of electron events. For all neutrino data,

$$\epsilon_{Evtx<30} = 0.978 \pm 0.002 \pm 0.007$$

and for all antineutrino data,

$$\epsilon_{Evtx<30} = 0.996 \pm 0.004 \pm 0.00$$

(5) The e/γ cut: This cut was investigated in a previous study[18] by Monte Carlo and by using test beam electron events. The test beam determination was considered more reliable. For all electron data,

$$\epsilon_{e/\gamma} = 0.91 \pm 0.01 \pm 0.02$$

(6) The road cut: The road cut was investigated in previous studies[18,19] by passing the full Monte Carlo events through the interactive road cut and determining the fraction accepted by the operator. Some events failed because of unrelated tracks from the overlay events or detector inefficiencies. For all neutrino data,

$$\epsilon_{Road} = 0.924 \pm 0.010 \pm 0.011$$

and for all antineutrino data,

$$\epsilon_{Road} = 0.950 \pm 0.010 \pm 0.010$$

(7) $\theta^2 < 0.03 rad^2$ cut: There was a small correction due to this angle cut. Most elastically scattered events were well below $0.03 rad^2$, but some events were rejected because of the angular resolution. Monte Carlo generator events with high statistics were generated, and the angle was smeared according to the known angular resolution. The cut was made on the smeared angle, and the fraction of the events accepted was determined. Since the angular resolution depended on the energy, various energy and angular resolution models were tried. For all neutrino data,

$$\epsilon_{\theta^2 < 0.03} = 0.993 \pm 0.001 \pm 0.031$$

and for all antineutrino data,

$$\epsilon_{\theta^2 < 0.03} = 0.993 \pm 0.001 \pm 0.030$$

(8) The wrong helicity contamination: A fraction of the elastic scattering events were due to the wrong helicity neutrinos in the beam (i.e. $\bar{\nu}_\mu$ in the ν_μ beam and ν_μ in the $\bar{\nu}_\mu$ beam). The wrong helicity flux was measured by the magnetic spectrometer (see chapter 2). The number of elastic scattering events due to the wrong helicity beam is obtained by calculating the flux averaged cross section. Since the elastic scattering cross sections have a linear dependence on energy, the flux averaged cross sections were simply a constant times the mean energy of the

beam. Thus the following formula was obtained for the contamination: For the neutrino data,

$$f_{wh} = \frac{f_{\bar{\nu}\nu}}{f_{\bar{\nu}\nu} + (1 - f_{\bar{\nu}\nu})\frac{<E_{\nu}>R}{<E_{\bar{\nu}\nu}>}}$$

and for the antineutrino data

$$f_{wh} = \frac{f_{\nu\bar{\nu}}}{f_{\nu\bar{\nu}} + (1 - f_{\nu\bar{\nu}})\frac{<E_{\bar{\nu}}>}{<E_{\nu\bar{\nu}}>R}}$$

where $f_{\nu\bar{\nu}}$ ($f_{\bar{\nu}\nu}$) is the contamination of ν ($\bar{\nu}$) in the $\bar{\nu}$ (ν) beam.

The wrong helicity contamination depends on the elastic scattering cross sections, in particular on R, the ratio of the cross sections. Since we are trying to measure the cross sections and the ratio, this dependence should be carried to the end of the analysis; nevertheless the corrections due to the wrong helicity beam were not large, and so the value of R (1.2) computed at the world average value of $\sin^2\theta_w$ (0.226 ± 0.004) [8] was used. The results were:

for the 1986 neutrino data,

$$f_{wh} = 0.029 \pm 0.005$$

and for the 1986 antineutrino data,

$$f_{wh} = 0.110 \pm 0.019$$

The results from the 1986 and 1981-83 data sets were combined by weighting them by the respective normalizations to get: for all neutrino data,

$$f_{wh} = 0.021 \pm 0.0 \pm 0.003$$

and all antineutrino data,

$$f_{wh} = 0.110 \pm 0.0 \pm 0.010$$

All of the error was systematic, arising from the uncertainties in acceptance for the spectrometer.

(9) The wrong flavor contamination: A fraction of the electron events were due to the wrong flavor neutrinos in the beam (i.e. ν_e in the ν_μ beam and $\bar{\nu}_e$ in the $\bar{\nu}_\mu$ beam). The background is due to $\nu_e e \rightarrow \nu_e e$ and $\bar{\nu}_e e \rightarrow \bar{\nu}_e e$. Both of these reactions can occur through either charged or neutral current in the Standard Model; therefore their cross sections are larger than $\nu_\mu e \rightarrow \nu_\mu e$ and $\bar{\nu}_\mu e \rightarrow \bar{\nu}_\mu e$ cross sections. The fraction, (f_{wf}), of electron events due to $\nu_e e$ or $\bar{\nu}_e e$ was estimated by assuming Standard Model cross sections with $\sin^2\theta_w = 0.225$ and by assuming the energy of the electron neutrinos to be about the same as the muon neutrinos. The flux of the wrong flavor neutrinos in the beam was estimated from data (Chapter 2).

For the neutrino data,

$$f_{wf} = 0.036 \pm 0.0 \pm 0.009$$

and for the antineutrino data,

$$f_{wf} = 0.021 \pm 0.0 \pm 0.010$$

All of the error is systematic, mainly from uncertainties in the flux.

The corrected total number of electron events were obtained by dividing the total number events observed by the total correction which is computed in table 6.2.2.

$$corr = \frac{A_{210-2100} \sum_i \epsilon_i}{(1 - f_{wh})(1 - f_{wf})}$$

The corrected total number of $\nu_\mu e \rightarrow \nu_\mu e$ events was:

$$N(\nu_\mu e \rightarrow \nu_\mu e) = 311.0 \pm 34.2[stat] \pm 20.4[syst]$$

The corrected total number of $\bar{\nu}_\mu e \rightarrow \bar{\nu}_\mu e$ events was:

$$N(\bar{\nu}_\mu e \rightarrow \bar{\nu}_\mu e) = 159.8 \pm 22.1[stat] \pm 11.1[syst]$$

$A_{210\to 2100}$	$0.710 \pm 0.001 \pm 0.030$ $0.710 \pm 0.001 \pm 0.010$
ϵ_{soft}	$0.852 \pm 0.007 \pm 0.013$ $0.914 \pm 0.011 \pm 0.020$
ϵ_{eye}	0.980 ± 0.0022 0.950 ± 0.0063
$\epsilon_{Evtx<30}$	$0.978 \pm 0.002 \pm 0.007$ $0.996 \pm 0.004 \pm 0.0$
$\epsilon_{e/\gamma}$	$0.91 \pm 0.01 \pm 0.02$ $0.91 \pm 0.01 \pm 0.02$
ϵ_{Road}	$0.924 \pm 0.010 \pm 0.011$ $0.950 \pm 0.010 \pm 0.010$
$\epsilon_{\theta^2<0.03}$	$0.993 \pm 0.001 \pm 0.031$ $0.993 \pm 0.001 \pm 0.030$
$(1 - f_{wh})$	$0.979 \pm 0.0 \pm 0.003$ $0.890 \pm 0.0 \pm 0.010$
$(1 - f_{wf})$	$0.964 \pm 0.0 \pm 0.009$ $0.979 \pm 0.0 \pm 0.010$
Total *corr*	ν_μ $0.477 \pm 0.009 \pm 0.031$ $\bar{\nu}_\mu$ $0.580 \pm 0.012 \pm 0.031$

Table 6.2.2 Acceptances and efficiencies for all data. The upper number for each item is for the neutrino data and the lower number is for the antineutrino data.

Table 6.2.3 shows the systematic errors arising from the signal extraction and all the factors that contribute to the total efficiency. Since much of the analysis was the same for neutrino and antineutrino data, some of the systematic error was correlated. The correlated error was calculated by examining each contribution to the systematic error and if the analysis process contributing the error was

Systematic error	σ_ν	$\sigma_{\bar{\nu}}$	$\sigma_{\nu\bar{\nu}}$
Signal	2.3%	4.9%	–
$A_{210\rightarrow 2100}$	4.2%	1.4%	2.4%
ϵ_{soft}	1.5%	2.2%	1.8%
ϵ_{eye}	None	None	
$\epsilon_{Evtx<30}$	0.7%	0.0%	–
$\epsilon_{e/\gamma}$	2.2%	2.2%	2.2%
ϵ_{Road}	1.2%	1.1%	1.1%
$\epsilon_{\theta^2<0.03}$	3.1%	3.0%	3.0%
$(1 - f_{wh})$	0.3%	1.1%	–
$(1 - f_{wf})$	0.9%	1.0%	–
Total	6.6%	7.0%	4.9%

Table 6.2.3 Systematic errors for $\nu_\mu e \rightarrow \nu_\mu e$ and $\bar{\nu}_\mu e \rightarrow \bar{\nu}_\mu e$. The systematic correlation is also illustrated.

identical for both data sets, the systematic error was considered fully correlated; if the analysis process was not identical the error was considered not correlated.

Chapter 7.

Results and Conclusions

1. The Cross Section

From the corrected number of electron events the cross section for neutrino/antineutrino electron elastic scattering was calculated using the quasielastic normalization from Chapter 5. The cross section, expressed in a model independent way, is:

$$\sigma(E_\nu) = \rho^2 \frac{G_F^2 m_e E_\nu}{2\pi}[(g_V \pm g_A)^2 + \frac{1}{3}(g_V \mp g_A)^2]$$

where g_V and g_A are the vector and axial vector couplings of the electron, respectively. The upper sign in the formula is for $\nu_\mu e \to \nu_\mu e$, and the lower sign is for $\bar{\nu}_\mu e \to \bar{\nu}_\mu e$ scattering. $g_V = -1/2 + 2\sin^2\theta_W$ and $g_A = -1/2$ are the predictions of the Standard Model. We eliminate the dependence on neutrino energy and define a cross section per unit energy:

$$\sigma' = \frac{\sigma(E_\nu)}{E_\nu}.$$

The cross section in terms of the observed quantities is:

$$\sigma(E_\nu) = \frac{N_e}{n_e \phi_\nu(E_\nu)}$$

where N_e is the number of $\nu_\mu e \to \nu_\mu e$ or $\bar{\nu}_\mu e \to \bar{\nu}_\mu e$ events observed in the detector, n_e is the number of target electrons in the fiducial volume of the detector, and $\phi_\nu(E_\nu)$ is the neutrino flux incident on the detector. The total flux was determined from the normalization reaction of which the cross section is well known[27]. The flux is expressed as:

$$\phi_\nu(E_\nu) = \frac{N_{QE}}{n_{n/p}\sigma_{QE}(E_\nu)}$$

where N_{QE} is the number of quasi-elastic events observed in the detector, and $n_{n/p}$ is the number of target nucleons – neutrons for the neutrino quasielastics and protons for the antineutrino quasielastics – in the fiducial volume of the detector. The elastic scattering cross section can now be expressed as:

$$\sigma(E_\nu) = \frac{N_e}{N_{QE}} \frac{n_{n/p}}{n_e} \sigma_{QE}(E_\nu).$$

The energy integrated expression of the cross section is:

$$\int \sigma(E_\nu)\phi(E_\nu)dE_\nu = \frac{N_e}{N_{QE}} \frac{n_{n/p}}{n_e} \int \sigma_{QE}(E_\nu)\phi(E_\nu)dE_\nu.$$

After integration the cross section per unit energy is expressed as:

$$\sigma' = \frac{N_e}{N_{QE}} \frac{n_{n/p}}{n_e} \frac{< \sigma_{QE} >_\phi}{< E_\nu >_\phi}$$

$$< \sigma_{QE} >_\phi = \int \sigma_{QE}(E_\nu)\phi(E_\nu)dE_\nu$$

$$< E_\nu >_\phi = \int E_\nu \phi(E_\nu)dE_\nu.$$

Study of the detector chemistry (chapter 2) determined the neutron to electron ratio to be $n_n/n_e = 0.811$; n_p/n_e is, of course, 1.0. All the quantities in the expression for the cross section are known; combining them and their errors gives the following values:

$$\frac{\sigma_{\nu_\mu e \to \nu_\mu e}}{< E_\nu >} = (1.80 \pm 0.20[stat] \pm 0.25[syst]) \times 10^{-42} cm^2/GeV.$$

$$\frac{\sigma_{\bar{\nu}_\mu e \to \bar{\nu}_\mu e}}{< E_\nu >} = (1.17 \pm 0.16[stat] \pm 0.13[syst]) \times 10^{-42} cm^2/GeV.$$

The acceptance factor, $A_{210 \to 2100}$, for the electron events was dependent on the particular value of g_V and g_A. To determine g_V and g_A and $\sin^2\theta_W$ properly, the functional dependence of $A_{210 \to 2100}$ must be included in the least χ^2 fits which extract $\sin^2\theta_W$ and the relational form of g_V and g_A. The functional form of the acceptance was:

for the neutrino data,

$$A^{\nu}_{210 \to 2100} = \frac{\int \int_{210 < E_e < 2100} dy dE_\nu \phi_\nu(E_\nu) E_\nu [(g_V + g_A)^2 + (1-y)^2 (g_V - g_A)^2]}{\int_0^1 \int_0^\infty dy dE_\nu \phi_\nu(E_\nu) E_\nu [(g_V + g_A)^2 + (1-y)^2 (g_V - g_A)^2]}$$

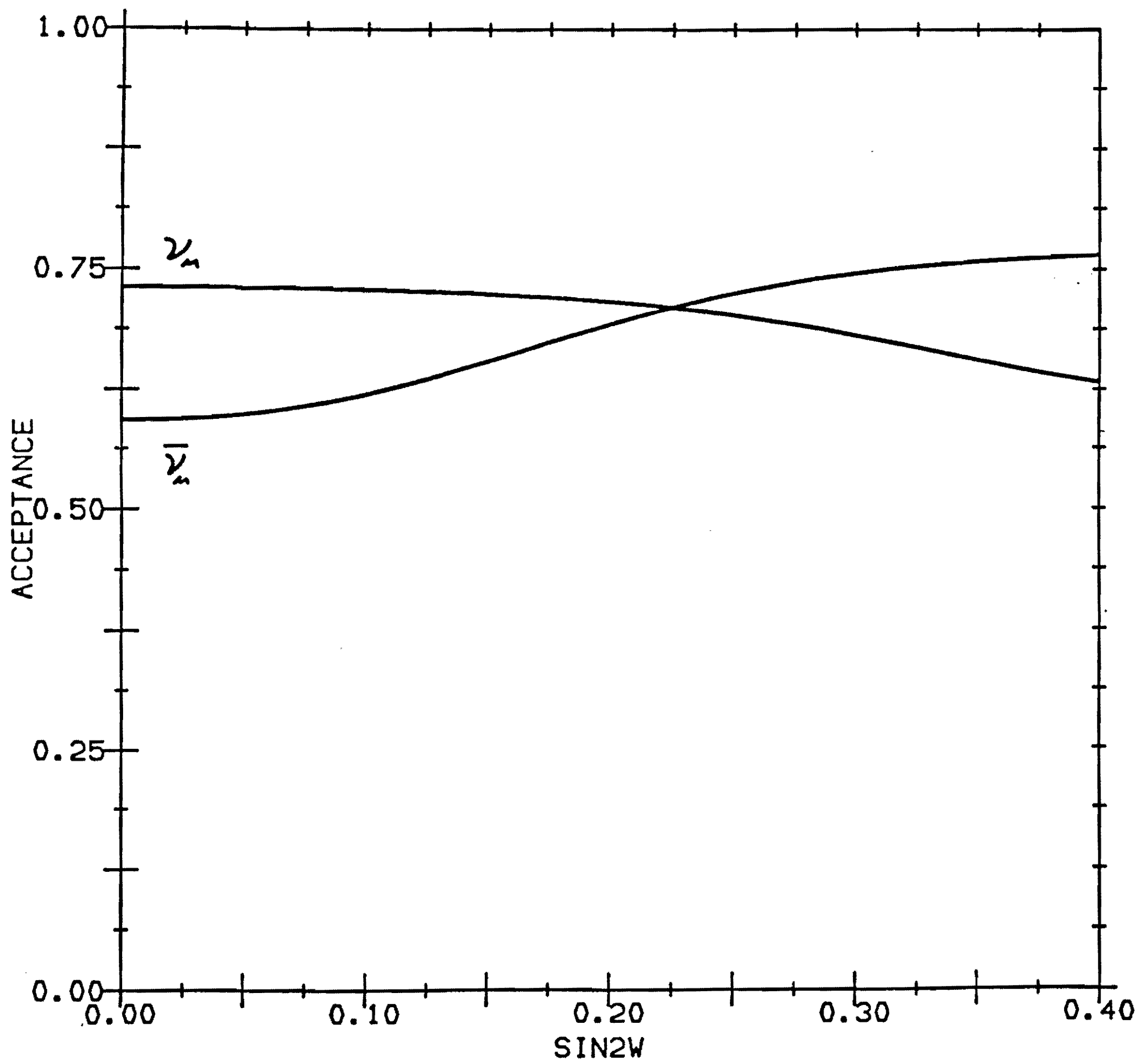

Figure 7.1.1 The acceptance, $A_{210\rightarrow2100}$, as a function of $\sin^2\theta_W$

and for the antineutrino data,

$$A^{\bar{\nu}}_{210\to2100} = \frac{\int \int_{210<E_e<2100} dydE_{\bar{\nu}}\phi_{\bar{\nu}}(E_{\bar{\nu}})E_{\bar{\nu}}[(g_V-g_A)^2+(1-y)^2(g_V+g_A)^2]}{\int_0^1 \int_0^\infty dydE_{\bar{\nu}}\phi_{\bar{\nu}}(E_{\bar{\nu}})E_{\nu}[(g_V-g_A)^2+(1-y)^2(g_V+g_A)^2]}$$

Figure 7.1.1 illustrates the functional dependence. An acceptance correction factor was determined by normalizing the energy acceptance value to the acceptance value determined by Monte Carlo at $\sin^2\theta_W = 0.225$:

$$A_{corr}(g_V,g_A) = \frac{A_{210\to2100}(g_V,g_A)}{A_{210\to2100}(\sin^2\theta_W = 0.225)}.$$

For accelerator energies ($E_\nu >> m_e$) and $y = E_e/E_\nu$; therefore the acceptance correction factors by numerical integration over the neutrino beam fluxes were:

$$A^{\nu}_{corr}(g_V,g_A) = \frac{1.0272(g_V+g_A)^2 + 0.2796(g_V-g_A)^2}{(g_V+g_A)^2 + 1/3(g_V-g_A)^2}$$

$$A^{\bar{\nu}}_{corr}(g_V,g_A) = \frac{1.0953(g_V-g_A)^2 + 0.2850(g_V+g_A)^2}{(g_V-g_A)^2 + 1/3(g_V+g_A)^2}$$

By using the acceptance correction factors and the measured cross sections, the relational form of g_V and g_A was determined from a least χ^2 fit. The χ^2 function is expressed as

$$\chi^2 = \frac{(\sigma^{Th}(g_V,g_A) - \sigma^{Exp}/A_{corr}(g_V,g_A))^2}{(\delta\sigma^{Exp}/A_{corr}(g_V,g_A))^2}$$

where $\sigma^{Th}(g_V,g_A)$ is the theoretical prediction and σ^{Exp} is the experimental determination of the cross section. $\delta\sigma^{Exp}$ is the error on the experimental determination of the cross section and $A_{corr}(g_V,g_A)$ is the acceptance correction factor. The relational forms are ellipses (see Fig. 7.1.2) and the 68% confidence level ($\Delta\chi^2 = 1$) interval is the region between the two ellipses in the figure. With the predictions for g_V and g_A from the Standard Model incorporated in the χ^2 function, the electroweak mixing parameter, $\sin^2\theta_W$, was determined:

from the $\nu_\mu e \to \nu_\mu e$ cross section,

$$\sin^2\theta_W = 0.195^{+0.026}_{-0.020}[stat]^{+0.033}_{-0.025}[syst]$$

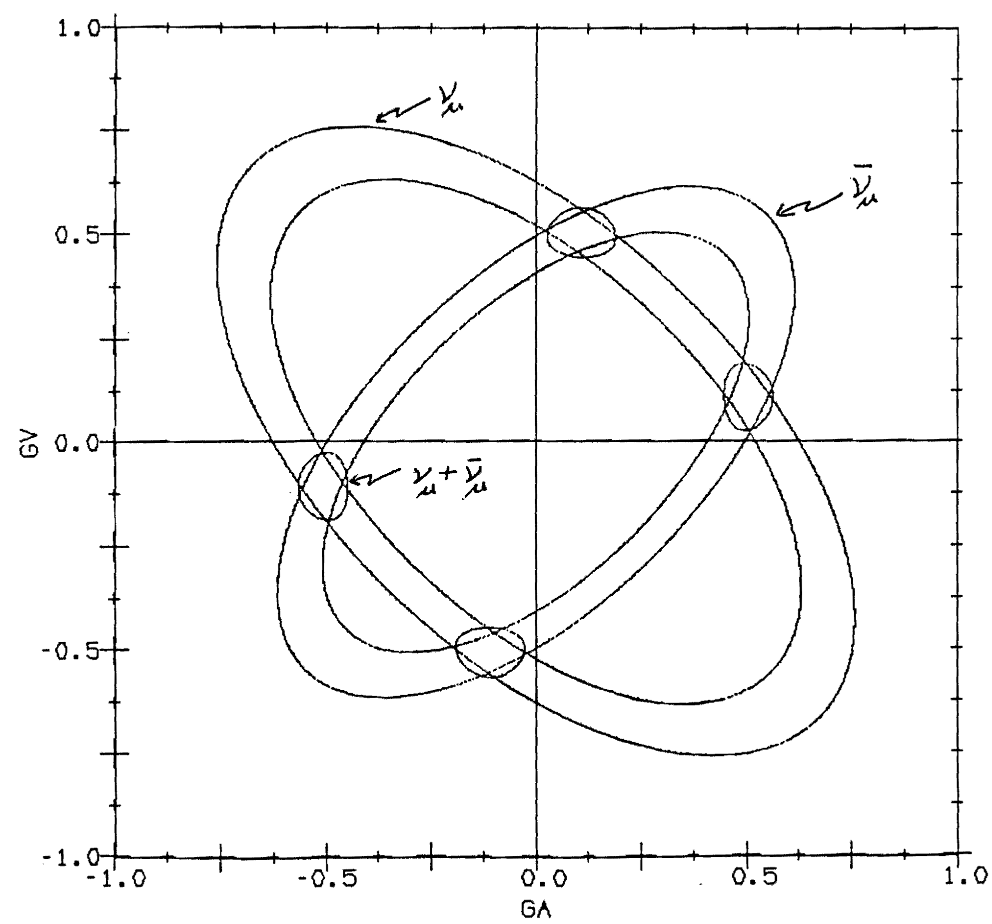

Figure 7.1.2 68% confidence level plot of g_V vs. g_A for the cross section for $\nu_\mu e \rightarrow \nu_\mu e$ and $\bar{\nu}_\mu e \rightarrow \bar{\nu}_\mu e$ scattering and also the combined fit.

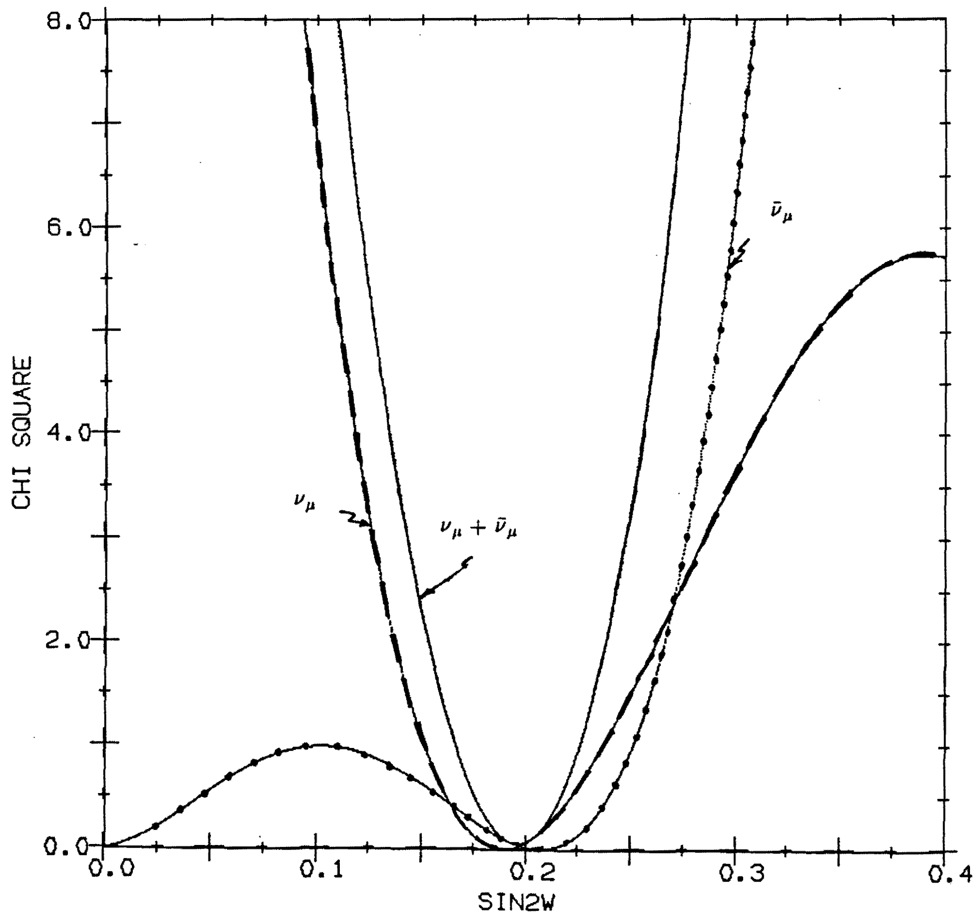

Figure 7.1.3 χ^2 plots for the fits to $\sin^2 \theta_W$

and from the $\bar{\nu}_\mu e \rightarrow \bar{\nu}_\mu e$ cross section,

$$\sin^2\theta_W = 0.200^{+0.032}_{-0.203}[stat]^{+0.027}_{-0.203}[syst]$$

where the statistical and systematic errors were treated separately. The resulting errors are at the 68% confidence level ($\Delta\chi^2 = 1$). The χ^2 plots of the fits for $\sin^2\theta_W$ are shown in Fig. 7.1.3.

2. The Ratio

The results for neutrino electron elastic scattering were combined with results for antineutrino electron elastic scattering to get a better determination of g_V and g_A by expressing results as the ratio of two cross sections:

$$R = \frac{\sigma(\nu_\mu e \rightarrow \nu_\mu e)}{\sigma(\bar{\nu}_\mu e \rightarrow \bar{\nu}_\mu e)}.$$

The ratio is independent of the Z^0 coupling constant, ρ; it only depends on the weak coupling constants of the electron. Since the determination of each cross section was performed in a similar fashion, many systematic effects cancel, thereby reducing the error in the final determination. The acceptable solutions for g_V and g_A are constrained to within the intersection of the separate solutions for each cross section determination (Fig. 7.1.2). Finally, the error on $\sin^2\theta_W$ is less sensitive to the error on the ratio than on the individual cross sections (Fig. 7.2.1).

The ratio can be expressed in terms of g_V and g_A by the Standard Model as

$$R = \frac{(g_V + g_A)^2 + 1/3(g_V - g_A)^2}{(g_V - g_A)^2 + 1/3(g_V + g_A)^2}$$

and in terms of $\sin^2\theta_W$ as

$$R = 3\frac{1 - 4\sin^2\theta_W + \frac{16}{3}\sin^4\theta_W}{1 - 4\sin^2\theta_W + 16\sin^4\theta_W}.$$

The ratio is determined from a least χ^2 fit. The χ^2 function is expressed as:

$$\chi^2 = \frac{(\sigma_{\nu_\mu e} - \sigma_{\bar{\nu}_\mu e}R)^2}{\delta\sigma^2_{\nu\nu} - 2\delta\sigma^2_{\nu\bar{\nu}}R + \delta\sigma^2_{\bar{\nu}\bar{\nu}}R^2}$$

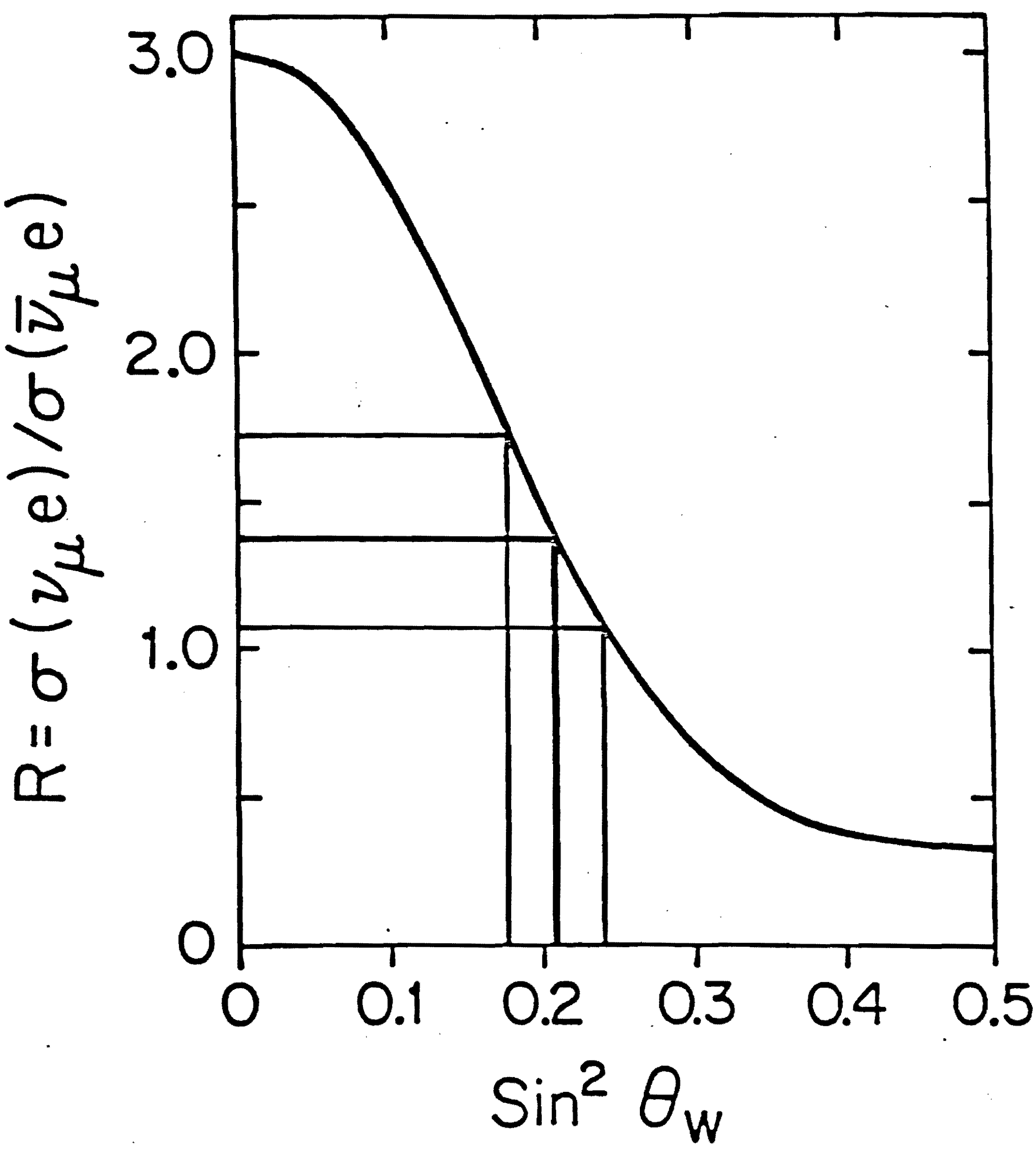

Figure 7.2.1 The Ratio v. $\sin^2\theta_W$

where $\sigma_{\nu_\mu e}$ and $\sigma_{\bar{\nu}_\mu e}$ are the measured cross sections for $\nu_\mu e \rightarrow \nu_\mu e$ and $\bar{\nu}_\mu e \rightarrow \bar{\nu}_\mu e$ scattering, respectively; $\delta\sigma_{\nu\nu}$ and $\delta\sigma_{\bar{\nu}\bar{\nu}}$ are the experimental errors associated with the measured $\nu_\mu e \rightarrow \nu_\mu e$ and $\bar{\nu}_\mu e \rightarrow \bar{\nu}_\mu e$ cross sections, respectively; $\delta\sigma_{\nu\bar{\nu}}$ is the correlated (systematic) error associated with the two cross section determinations. The results for the ratio from the χ^2 fit is:

$$R = 1.53^{+0.30}_{-0.25}[stat]^{+0.18}_{-0.17}[syst]$$

where the error limits correspond to $\Delta\chi^2 = 1$. If the Weinberg-Salam predictions of $g_V = -1/2 + 2\sin^2\theta_W$ and $g_A = -1/2$ are incorporated, the electroweak mixing parameter is determined to be:

$$\sin^2\theta_W = 0.199^{+0.020}_{-0.019}[stat]^{+0.013}_{-0.013}[syst].$$

The χ^2 plots of the fits to the cross sections and the ratio for $\sin^2\theta_W$ are shown in Fig. 7.1.3.

The weak neutral current coupling constants of the electron, g_V and g_A were determined from a least squares fit in the form

$$\chi^2 = \begin{pmatrix} \Delta x & \Delta y \end{pmatrix} \begin{pmatrix} t_{xx} & t_{xy} \\ t_{xy} & t_{yy} \end{pmatrix} \begin{pmatrix} \Delta x \\ \Delta y \end{pmatrix}$$

$$\Delta x = \sigma^{Th}_{\nu_\mu e} - \sigma^{Exp}_{\nu_\mu e}$$

$$\Delta y = \sigma^{Th}_{\bar{\nu}_\mu e} - \sigma^{Exp}_{\bar{\nu}_\mu e}$$

$$\begin{pmatrix} t_{xx} & t_{xy} \\ t_{xy} & t_{yy} \end{pmatrix} = \begin{pmatrix} \epsilon^2_\nu & \epsilon^2_{\nu\bar{\nu}} \\ \epsilon^2_{\nu\bar{\nu}} & \epsilon^2_{\bar{\nu}} \end{pmatrix}^{-1}$$

The elements ϵ_ν and $\epsilon_{\bar{\nu}}$ are the total errors associated with the neutrino and anti-neutrino cross sections, respectively. The element $\epsilon_{\nu\bar{\nu}}$ is the correlated error between the neutrino and antineutrino cross sections. By performing the matrix multiplication, the form of the χ^2 becomes:

$$\chi^2 = (\sigma^{Th}_{\nu_\mu e} - \sigma^{Exp}_{\nu_\mu e})^2 t_{xx} + 2(\sigma^{Th}_{\nu_\mu e} - \sigma^{Exp}_{\nu_\mu e})(\sigma^{Th}_{\bar{\nu}_\mu e} - \sigma^{Exp}_{\bar{\nu}_\mu e})t_{xy} + (\sigma^{Th}_{\bar{\nu}_\mu e} - \sigma^{Exp}_{\bar{\nu}_\mu e})^2 t_{yy}.$$

MINUIT[31] was used to minimize the χ^2 to determine the best values for g_V and g_A in the theoretical expression for the respective cross sections; the functional dependence of the the acceptance term, $A_{210\rightarrow 2100}$, on g_V and g_A was used (as discussed in the previous section). The 68% confidence interval ($\Delta\chi^2 = 1.65$ for two degrees of freedom) from the combined fit to the two cross sections is shown in Fig. 7.2.2. The fit results in four possible solutions for g_V and g_A. Results from $e^+e^- \rightarrow l^+l^-$ experiments [32] eliminate two of the possible solutions and results from a $\bar{\nu}_e$ reactor experiment [33] eliminate the third possible solution. From the remaining minimized χ^2 solution, the results are:

$$g_V = -0.102^{+0.039}_{-0.040}[stat]^{+0.029}_{-0.028}[syst]$$

$$g_A = -0.503^{+0.024}_{-0.022}[stat]^{+0.029}_{-0.027}[syst]$$

For the above fits to g_V and g_A, the Z^0 coupling, ρ, was set to the Standard Model value, $\rho = 1$. Since ρ is simply a multiplicative factor in both cross sections, the χ^2 function is not very sensitive to changes in ρ because g_V and g_A can also be scaled; therefore ρ was not used as a parameter in the fits.

3. The Differential Cross Section

The theoretical differential cross section for $\nu_\mu e \rightarrow \nu_\mu e$ (upper sign) and $\bar{\nu}_\mu e \rightarrow \bar{\nu}_\mu e$ (lower sign) scattering is expressed in terms of g_V and g_A:

$$\frac{d\sigma}{dy} = \frac{G_F^2 m_e}{2\pi} E_\nu((g_V \pm g_A)^2 + (g_V \mp g_A)^2(1-y)^2)$$

where $y = (E_e - m_e)/E_\nu$. The cross section can be thought of as made of two components: the first component is independent of y, and the second component varies as $(1-y)^2$. Furthermore, since y and θ^2 are related through kinematics(chapter 1), the first and second term in the cross section correspond to two different θ^2 distributions(Fig. 7.3.1). The second term is less sharply peaked in the forward direction because the cross section is suppressed as y approaches 1. The values of g_V and g_A determine the relative contributions of the two components to the final distributions.

Relatively poor shower energy resolution, compared to the angular resolution, and the uncertainty in neutrino energy due to the wide band spectrum

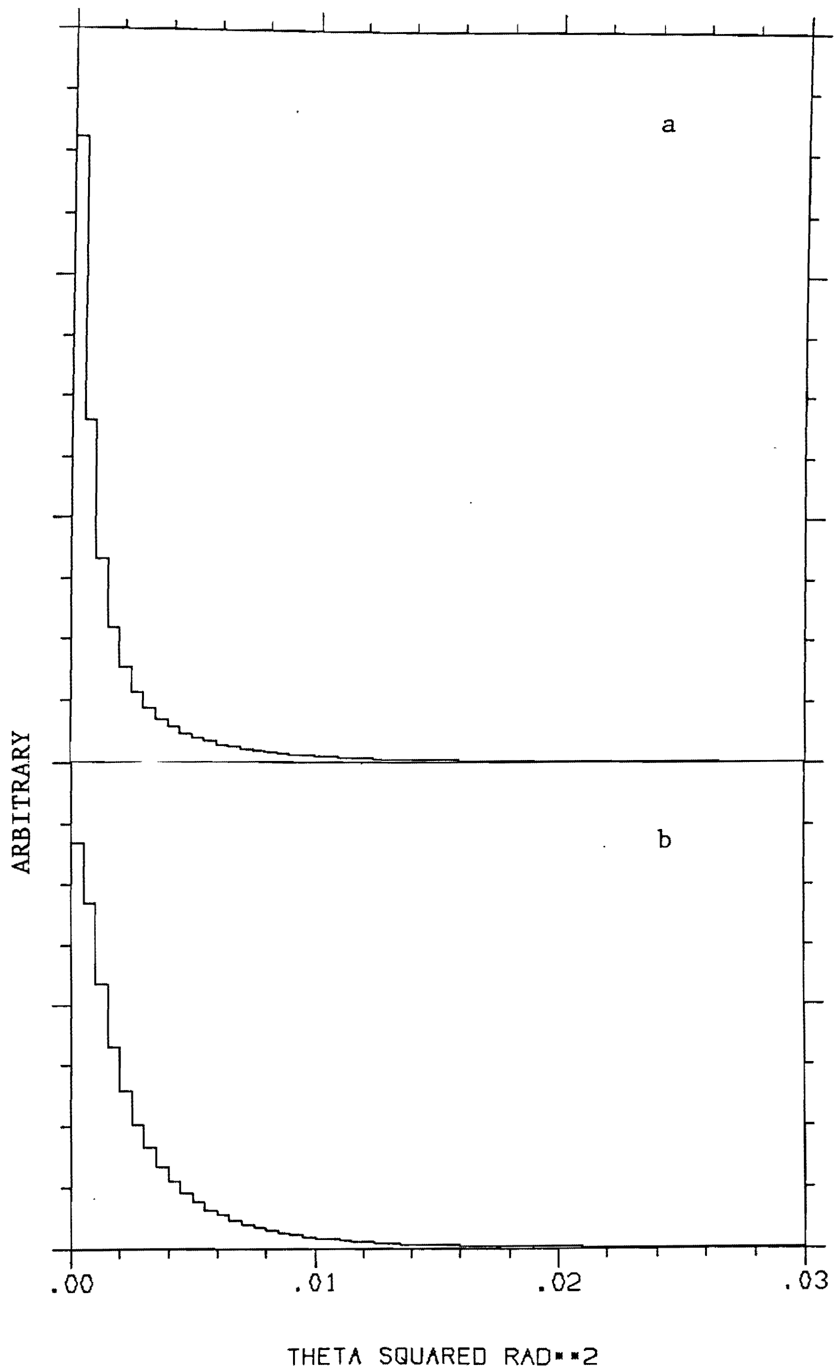

Figure 7.3.1 θ^2 distributions for the two components in the differential cross section for $\nu_\mu e \rightarrow \nu_\mu e$ scattering; distributions for $\bar{\nu}_\mu e \rightarrow \bar{\nu}_\mu e$ scattering are similar. The distributions depend only on the spectrum of neutrinos; the value of $\sin^2\theta_w$ determines the relative contribution of the two distributions in the true distribution. (a) θ^2 distribution for the flat term. (b) θ^2 distribution for the $(1-y)^2$ term.

precluded determination of y for each event. Nevertheless, the excellent θ^2 resolution enabled us to make fits to the θ^2 distributions. The θ^2 distributions were binned in 60 bins in order that each bin had the width of one standard deviation in the signal region. A likelihood fit was made to the θ^2 distributions using the following function as the parent distribution:

$$n_i = \frac{G_F^2 m_e}{2\pi} F_{norm}((g_V \pm g_A)^2 A_1 f_i + (g_V \mp g_A)^2 A_2 \frac{y_i}{3}) + N_b b_i$$

$$F_{norm} = \frac{N_{QE} < E_\nu >}{< \sigma(QE) >}$$

where the index i runs over the θ^2 bins, F_{norm} is the quasielastic normalization; f_i, y_i, and b_i are the normalized θ^2 distributions corresponding to the first term, second term, and the background in the distribution, respectively; A_1 and A_2 are the acceptances for the first and second terms; N_b is the total number of background events. The upper sign in the formula is for $\nu_\mu e \to \nu_\mu e$ and the lower sign is for $\bar{\nu}_\mu e \to \bar{\nu}_\mu e$ data.

A negative log likelihood function was calulated by assuming Poisson statistics in each bin; the FORTRAN package MINUIT was used to minimize the negative log likelihood function by varying g_V, g_A, and N_b. The function was computed and minimized separately for the neutrino and the antineutrino data; a simulataneous fit was also performed by adding the two functions and minimizing the result. 68% likelihood intervals were obtained for the parameters, g_V, g_A, and N_b, by allowing a function change of 0.5 from the minimum value. By using the Standard Model predictions for g_V and g_A in terms of $\sin^2\theta_w$ and minimizing with respect to $\sin^2\theta_w$, a 68% likelihood interval was obtained for $\sin^2\theta_w$.

The best fits to the θ^2 distributions are illustrated in figures 7.3.2, 7.3.3, 7.3.4, and 7.3.5. The likelihood contours for the separate fits to the neutrino and the antineutrino data and also the combined fit are illustrated in Fig. 7.3.6. Results for the couplings and $\sin^2\theta_w$ are below:

$$g_V = -0.107^{+0.035}_{-0.036}[stat]^{+0.029}_{-0.028}[syst]$$

$$g_A = -0.514^{+0.023}_{-0.023}[stat]^{+0.029}_{-0.027}[syst]$$

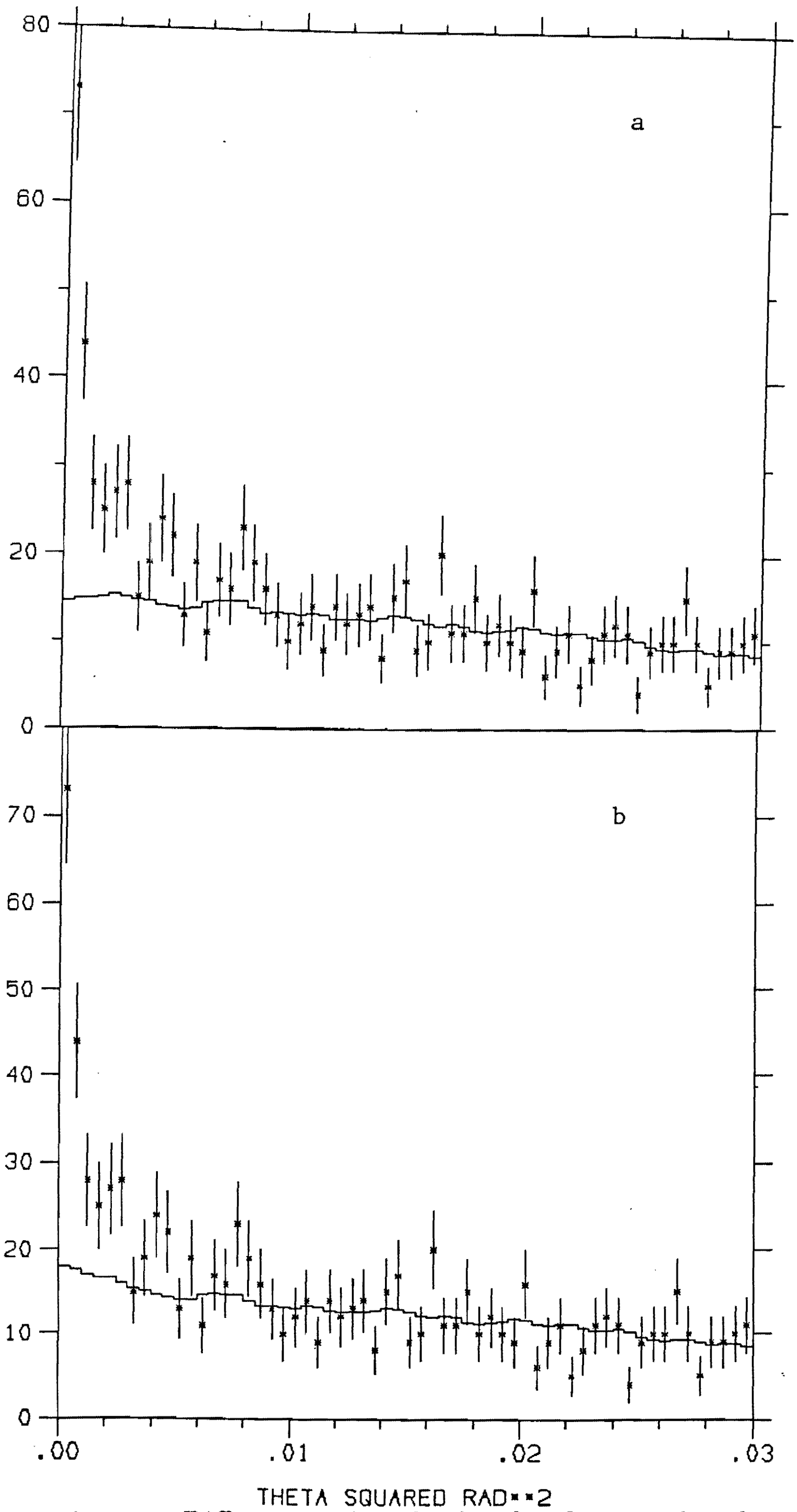

Figure 7.3.2 Differential distribution for the neutrino data. (a) Data (error bars) with background (solid curve). (b) Data with the background and the $(1-y)^2$ term

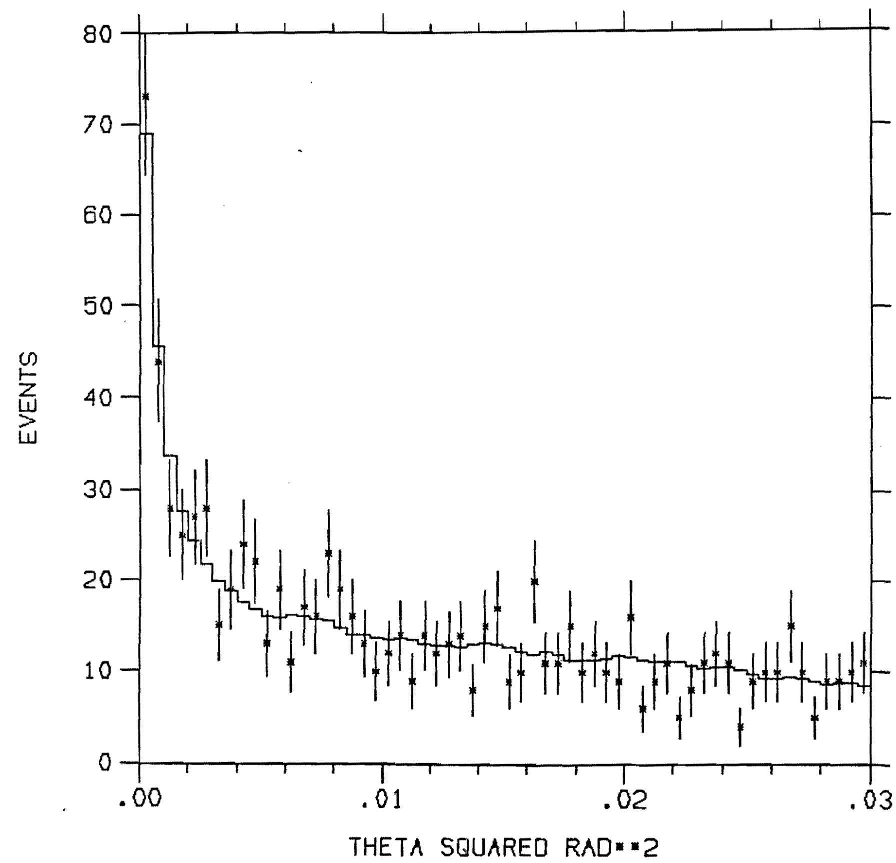

Figure 7.3.3 Differential distribution of the neutrino data with the complete fit including the flat, $(1-y)^2$, and the background terms.

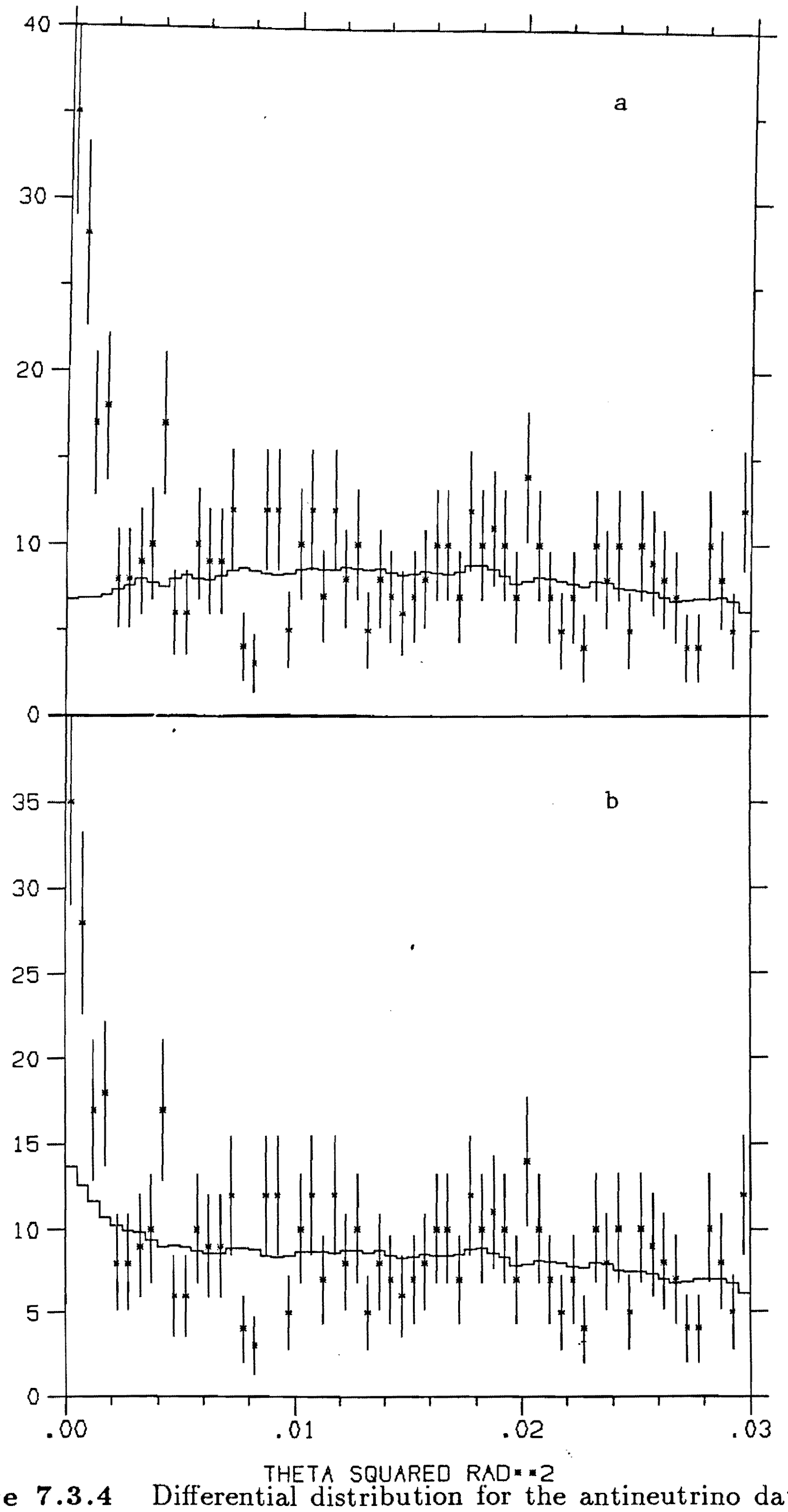

Figure 7.3.4 Differential distribution for the antineutrino data. (a) Data (error bars) with background (solid curve). (b) Data with the background and the $(1-y)^2$ term

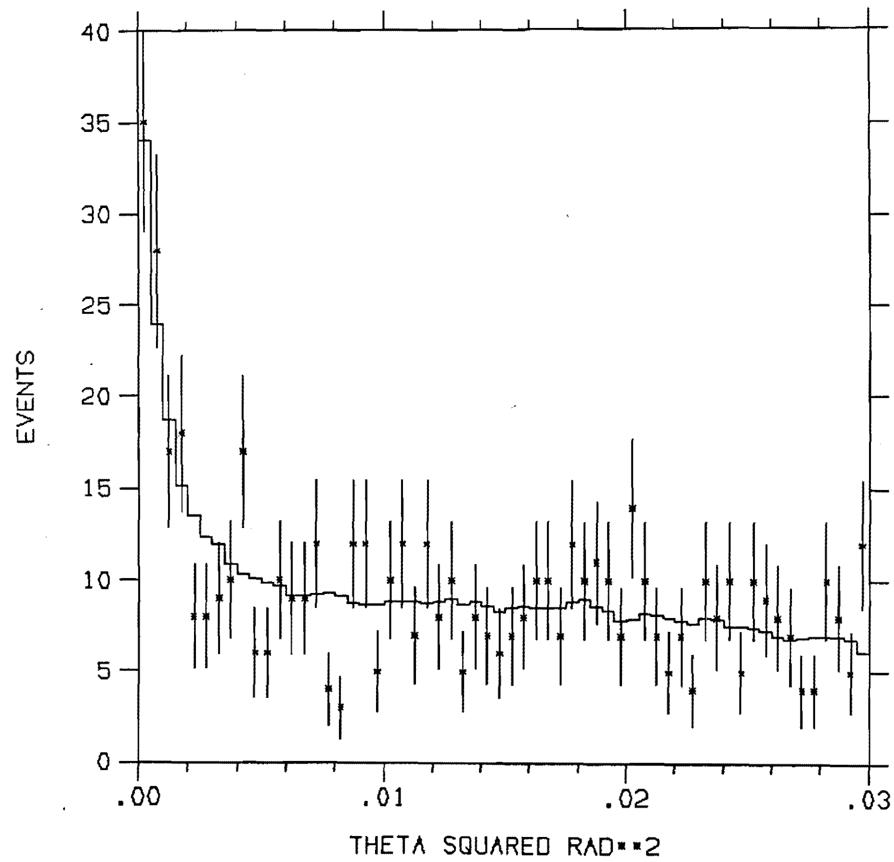

Figure 7.3.5 Differential distribution of the antineutrino data with the complete fit including the flat, $(1-y)^2$, and the background terms.

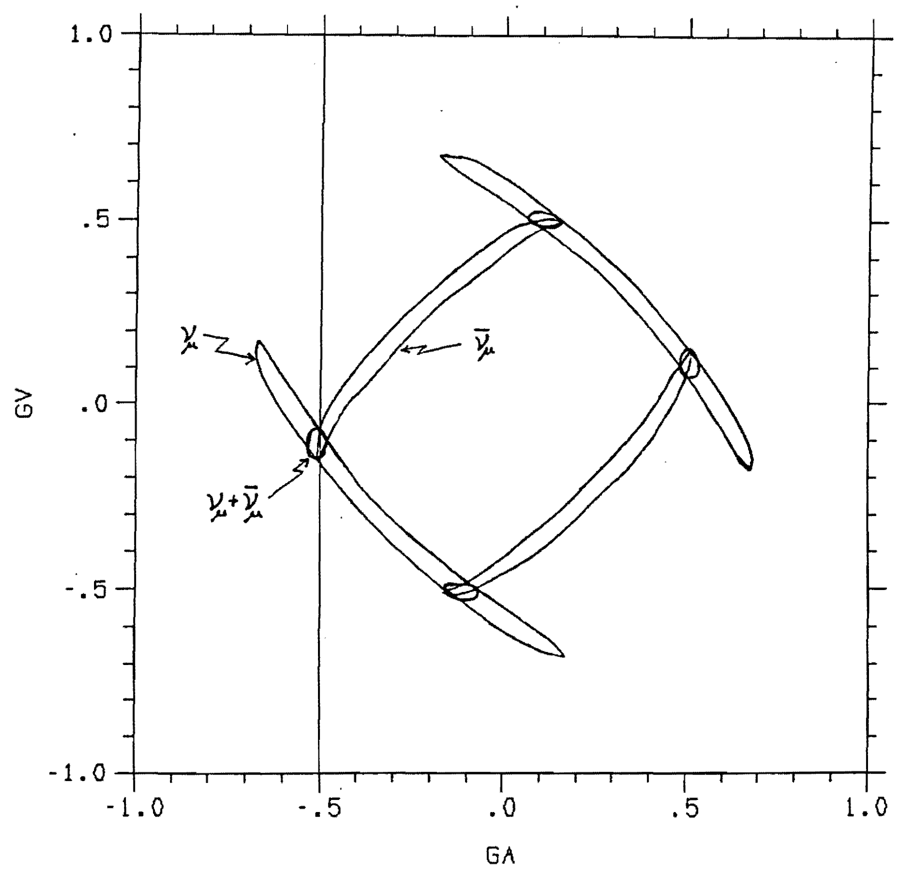

Figure 7.3.6 Likelihood contours for the fits to the neutrino and antineutrino data and also the combined fit. The region outside the contours is excluded. The projections of the contours give 68% likelihood intervals for g_V and g_A.

$$\sin^2\theta_w = 0.195^{+0.018}_{-0.018}[stat]^{+0.013}_{-0.013}[syst]$$

There is good agreement between this determination and the determination obtained from the total cross sections. Futhermore, the total number of events obtained from the above fits ($168 \pm 18 \nu_\mu e \to \nu_\mu e$ and $99 \pm 15 \bar{\nu}_\mu e \to \bar{\nu}_\mu e$ events) agrees with the previous determination within the errors. These are the best determinations of the coupling constants from this experiment. The statistical errors are dominated by the small number of observed events, and the systematic errors are dominated by the uncertainty in normalization.

4. Electromagnetic Effects

Many gauge theories [34,35] propose possible electromagnetic properties for the neutrino. The properties may manifest themselves in the form of a magnetic moment or a charge radius. The properties can be tested for as modifications to the theoretical predictions of the cross sections for neutrino interactions.

Deviations of the cross sections for $\nu_\mu e \to \nu_\mu e$ and $\bar{\nu}_\mu e \to \bar{\nu}_\mu e$ scattering from the predictions of the Standard Model for a Weinberg angle determined from non-neutrino experiments can be considered as limits on the existence of electromagnetic effects for the muon neutrino. These limits were established by performing least squares fits of the electromagnetic predictions to the experimental determination of the cross sections where the free parameters were the magnitudes of the proposed magnetic moment, f, and charge radius, $< r^2 >$, for the muon neutrino. The best results are obtained by performing a fit to both cross sections and utilizing the correlated systematic errors.

The neutrino magnetic moment is understood to manifest itself as an additive modification to the total cross section for $\nu_\mu e \to \nu_\mu e$ and $\bar{\nu}_\mu e \to \bar{\nu}_\mu e$ scattering

$$\sigma^{Th} = \sigma^{WS}(\sin^2\theta_W) + \frac{\pi\alpha^2}{m_e^2} f^2[\ln(E_\nu/E_e^{min}) - 1 + E_e^{min}/E_\nu]$$

$$\frac{\pi\alpha^2}{m_e^2} = 2.49 \times 10^{-25} cm^2.$$

where $\sigma^{WS}(\sin^2\theta_W)$ is the Weinberg-Salam cross section prediction without electromagnetic modifications, f is the strength of the magnetic moment for the muon neutrino in units of Bohr magnetons, and $E_e^{min} = 0.2GeV$ is the experimental low energy cut-off on the recoil electron energy. For purposes of this test, the Weinberg-Salam cross section, $\sigma^{WS}(\sin^2\theta_W)$ was evaluated at

$$\sin^2\theta_W = 0.230 \pm 0.004[stat] \pm 0.008[syst].$$

This particular value [36] of $\sin^2\theta_W$ represents the best non-neutrino determination, and therefore it is unbiased by possible neutrino electromagnetic effects.

The form of the χ^2 function was:

$$\chi^2 = (\sigma^{Th}_{\nu_\mu e} - \sigma^{Exp}_{\nu_\mu e})^2 t_{xx} + 2(\sigma^{Th}_{\nu_\mu e} - \sigma^{Exp}_{\nu_\mu e})(\sigma^{Th}_{\bar{\nu}_\mu e} - \sigma^{Exp}_{\bar{\nu}_\mu e})t_{xy} + (\sigma^{Th}_{\bar{\nu}_\mu e} - \sigma^{Exp}_{\bar{\nu}_\mu e})^2 t_{yy}$$

where t_{xx}, t_{xy}, t_{yy} were elements of the inverted error matrix. The error on $\sin^2\theta_W$ was propagated into the error matrix, but it did not influence the result. The expression for the χ^2 was numerically minimized by a convergent step algorithm which established the 90% confidence level limit for the magnitude of the magnetic moment, f. The 90% confidence level limit ($\Delta\chi^2 = 1.65$) for the magnetic moment of the muon neutrino is:

$$f < 0.85 \times 10^{-9} Bohr\ magnetons.$$

A plot of χ^2 as a function of f^2 is shown in Fig. 7.4.1.

Neutrinos may interact with photons in higher order processes and thus aquire a charge radius. This can be observed in the cross sections for $\nu_\mu e \rightarrow \nu_\mu e$ and $\bar{\nu}_\mu e \rightarrow \bar{\nu}_\mu e$ scattering as a modification to the electroweak mixing parameter, $\sin^2\theta_W$, caused by interference terms due to replacement of the Z^0 by a photon. See Appendix C for a description of how the charge radius contributes to the cross section. The theoretical predictions for the cross sections can be expressed as:

$$\sigma^{Th} = \sigma^{WS}(\sin^2\theta_W + \delta)$$

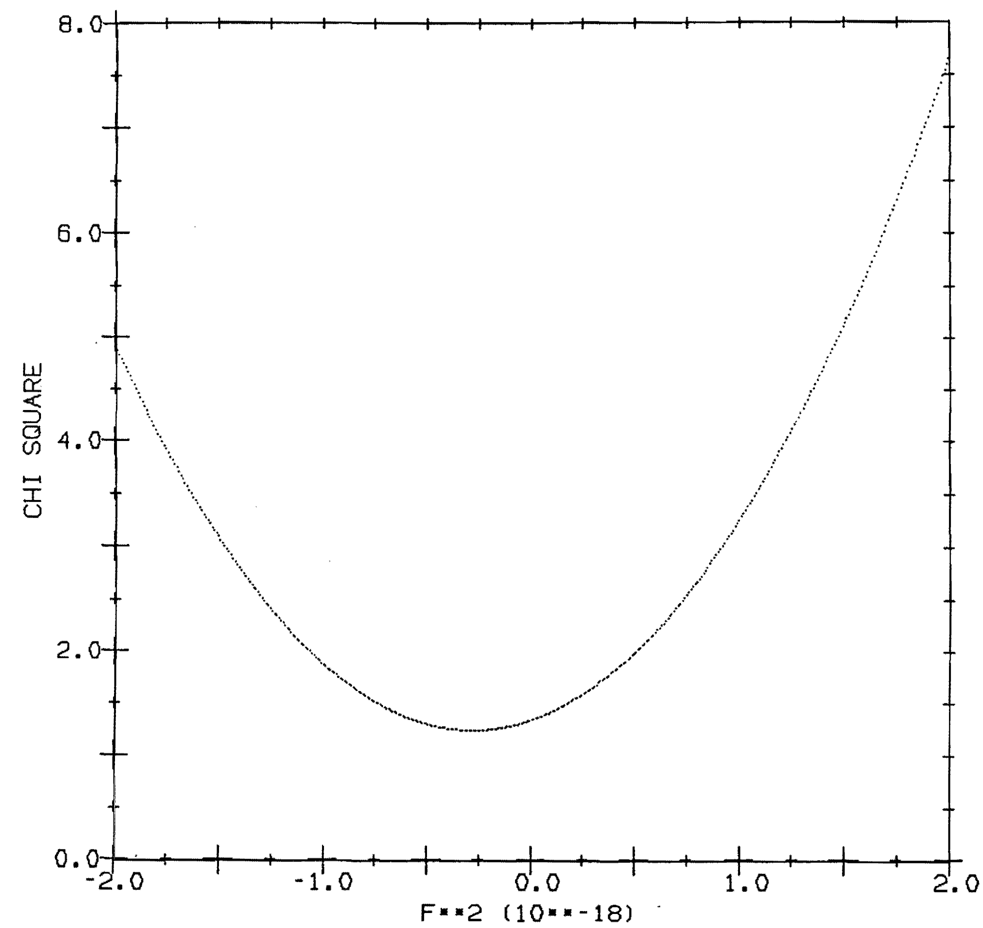

Figure 7.4.1 Plot of χ^2 vs. the square of the magnetic moment, f^2

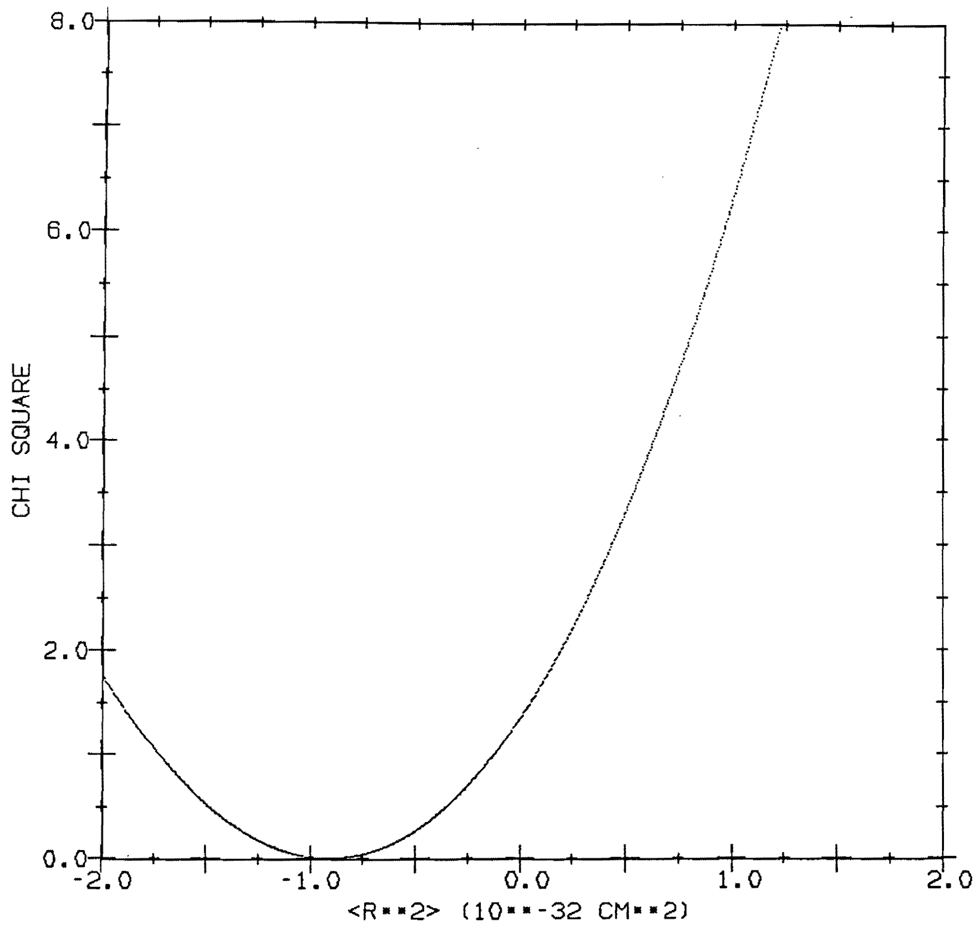

Figure 7.4.2 Plot of χ^2 v. charge radius, $< r^2 >$

$$\delta = \frac{\sqrt{2}\pi\alpha}{3G_F} < r^2 >= 3.37 \times 10^{30} cm^{-2} < r^2 > .$$

The best non-neutrino value of $\sin^2\theta_w$ was used. Using the same form of the χ^2 function as before, 90% confidence limits ($\Delta\chi^2 = 2.65$) were established for the charge radius. If the charge radius is allowed to be negative, a limit can also be obtained for the negative value.

$$(< r^2 >) < 0.24 \times 10^{-32} cm^2$$
$$(< r^2 >) > -2.11 \times 10^{-32} cm^2$$

5. Conclusion

Group	Beam	Total	Signal	$\sigma/E[\times 10^{-42} cm^2/GeV]$
GGM	CERN PS	1	0.7	$< 3(90\%CL)$
AC-PD	CERN PS	11	7.1	1.1 ± 0.6
GGM	CERN SPS	9	8.6	$2.4^{+1.2}_{-0.9}$
VMNOP	FNAL	46	34	1.4 ± 0.3
FMMN	FNAL	11	5.7	
E734	BNL AGS	76	51 ± 9	$1.6 \pm 0.29 \pm 0.26$*
BNL-COL	FNAL 15'	22	20.5	1.6 ± 0.4
CHARM	CERN SPS	195	83 ± 16	$1.8 \pm 0.3 \pm 0.4$
E734	BNL AGS	716	107 ± 16	$1.85 \pm 0.25 \pm 0.27$*
E734	BNL AGS	898	160 ± 19	$1.80 \pm 0.20 \pm 0.25$

* (previous analysis of partial data set)

Table 7.5.1 $\nu_\mu e \rightarrow \nu_\mu e$ cross section measurements

Group	Beam	Total	Signal	$\sigma/E[\times 10^{-42} cm^2/GeV]$
GGM	CERN PS	3	2.6	$1.0^{+2.1}_{-0.9}$
AC-PD	CERN PS	8	6.3	2.3 ± 1.1
BEBC-TST	CERN PS	1	0.5	$< 3.4(90\%CL)$
CHARM	CERN SPS	332	112 ± 21	$1.4 \pm 0.3 \pm 0.3$
E734	BNL AGS	329	52.5 ± 9.6	$1.16 \pm 0.20 \pm 0.14$*
E734	BNL AGS	572	97 ± 16	$1.17 \pm 0.16 \pm 0.13$

* (previous analysis of partial data set)

Table 7.5.2 $\bar{\nu}_\mu e \rightarrow \bar{\nu}_\mu e$ cross section measurements

Experiment	$\sin^2\theta_W$	Rad. Corr.
Atomic P.V.	$0.201 \pm 0.018 \pm 0.014$	+0.008
Atomic P.V. (New NBS)Cs	$0.211 \pm 0.007 \pm 0.018$	+0.007
$\nu_\mu e$, $\bar{\nu}_\mu e$	0.221 ± 0.019	+0.002
$\nu_\mu p$, $\bar{\nu}_\mu p$	0.208 ± 0.033	+0.002
eD asym.	$0.226 \pm 0.015 \pm 0.013$	−0.005
$\nu_\mu N$	$0.242 \pm 0.003 \pm 0.005$	−0.009
$M_W = 80.9 \pm 1.4 GeV$	0.212 ± 0.008	+0.017
$M_Z = 91.9 \pm 1.8 GeV$	0.208 ± 0.011	+0.022
World average $\sin^2\theta_W = 1 - M_W^2/M_Z^2$		0.230 ± 0.004
E734 $\sigma(\nu_\mu e)$, $\sigma(\bar{\nu}_\mu e)$:	$0.199 \pm 0.020 \pm 0.013$	+0.002
E734 $d\sigma/dy$ ($\nu_\mu e$, $\bar{\nu}_\mu e$):	$0.195 \pm 0.018 \pm 0.013$	-

Table 7.5.3 $\sin^2\theta_W$ determinations

In this thesis, the cross sections for $\nu_\mu e \to \nu_\mu e$ and $\bar{\nu}_\mu e \to \bar{\nu}_\mu e$ elastic scattering were determined. Several other experiments have measured the cross sections. The results are summarized in Table 7.5.1 and Table 7.5.2 [37].

The weak neutral current coupling constants were determined in a model independent way with a four fold ambiguity. Results from independent experiments remove the ambiguity. The allowed values of g_V and g_A are consistent with the predictions of the Standard Model where $g_V = -1/2 + 2\sin^2\theta_W$ and $g_A = -1/2$. Determinations of $\sin^2\theta_W$ from several experiments are given in Table 7.5.3 (See Ref. 8 and Ref. 43). along with the estimates of the radiative corrections.

The excellent angular resolution in this expeiment allowed us to fit to the differential distributions of $\nu_\mu e \to \nu_\mu e$ and $\bar{\nu}_\mu e \to \bar{\nu}_\mu e$ scattering for the first time. The results agree well with the Standard Model predictions of the structure of the neutral current. The analysis of the differential distribution gives the best determination of $\sin^2\theta_w$ which is presented separately in Table 7.5.3.

Group	Reaction	$E_\nu [GeV]$	$x = 0.23$	$x = 0.233$	$x = 0.25$
GGM	$\bar{\nu}_\mu e$	2.0	7.43	7.42	7.37
AC-PD	$\bar{\nu}_\mu e$	2.0	2.89	2.87	2.78
GGM	$\nu_\mu e$	2.2	2.84	2.85	2.96
AC-PD	$\nu_\mu e$	2.2	1.15	1.19	1.36
E734	$\nu_\mu e + \bar{\nu}_\mu e$	1.3		0.85	

(units of $\times 10^{-9}$ Bohr magnetons)

Table 7.5.4 Upper bound determinations for the magnetic moment

Upper limits were established for the values of the magnetic moment and charge radius of the muon neutrino. Determinations of the upper limit for the magnetic moment from this and several other experiments are given in Table 7.5.4[9] for various values of $\sin^2\theta_W$. The astrophysical limit[39](for $m_{\nu_\mu} < 10keV$) is:

$$f < 8.5 \times 10^{-11}.$$

Expectations from various gauge theories that extend the Standard Model establish upper limits for the magnetic moment:

$$f < 5.4 \times 10^{-12} Bohr\ magnetons$$

Theoretical calculations using the Standard Model give values for the charge radius in the following range:

$$< r^2 > \sim 10^{-33} - 10^{-34} cm^2$$

For a list of references about possible electromagnetic properties of neutrinos see Ref. 10. Also see Appendix C.

Appendix 1.

Eyescan Rules

The following is a summary of the rules followed for each eyescan.

1. First Eyescan Rules

Shower definition - A "good" shower is a forward electromagnetic shower with a "clean" vertex. A "good" shower should not look hadronic or have kinks. Do not use any energy, angle of fiducial volume criteria for the first scan.

While scanning, use the above definition and follow this algorithm:

Is there a "good" shower in the events?

Yes - continue

No - go to next event

Is the shower associated (points back to a common point) with any interaction greater than 3 modules in size?

Yes - if shower is associated with another shower, mark off 9 (gamma event); go to next event

No - continue

Is the shower larger than 6 modules and clean ("no kinks")?

Yes - mark off 1,3

No - mark off 2,4

Is the shower associated with any interaction less than or equal to 3 modules in size?

Yes - if up stream mark off 5 (stub up), if down stream mark off 6 (stub down)

No - continue

Is there a short track (less than 10 modules) coming from the vertex of the shower?

Yes - mark off 8 (ep event)

No - continue

Is there an unassociated interaction (muon or track) in the event?

Yes - mark off 7 (2 in 1 event); go to next event

No - go to next event

Summary of flag codes:

1,3 - good, large electromagnetic shower

2,4 - poor, small electromagnetic shower

5 - up stream stub

6 - down stream stub

7 - 2 in 1 event

8 - $e^{-}p$ event

9 - 2 gamma event

2. Second Eyescan Rules

Shower definition - A "good" shower is deined as any forward electromagnetic shower (non-hadronic, no kinks) with a "clean" vertex (no extra prongs, no extra hits) satisfying the following fiducial and energy constraints

$$4 < X_{PDT} < 53$$

$$4 < Y_{PDT} < 53$$

$$3 < Z_{MOD} < 101$$

$$E_{cal1} < 60MeV$$

$$E_{cal2} < 60MeV$$

$$E_{tot} > 100MeV.$$

Kept Events:

Any "good" shower event not failing the listed criteria with no associated interactions should be flagged with CODE 1 ("Keep Event") and its vertex noted. (CODE 1 is exclusive with CODE 3.)

Need Study Events:

Any shower event with "substantial" bad energy information (e.g. "***") or with another "event" (muon, etc.) in the same time cluster which will "complicate" the shower event (e.g. no clear separation) should be flagged with CODE 2 ("Needs Study").

Good Stub Events:

Any shower event with an associated (both views) up stream stub (at least one calorimeter hit of greater than 5 MeV and one PDT hit) within 20 modules of the shower vertex should be flagged as a photon with CODE 3 ("Good Stub") and its vertex noted. (CODE 3 is exclusive with CODE 1.)

Extra Up Stream Energy:

Any shower event with unassociated extra up stream energy within 20 modules of the vertex should be flagged with CODE 4 ("Extra Up").

Extra Down Stream Energy:

Any shower event with extra down stream energy outside of the shower "road" and within 20 modules of the vertex should be flagged with CODE 5 ("Extra Down").

2 in 1 Events:

Any shower with unassociated "activity" of greater than 2 calorimter calls (e.g. tracks, interactions, noise) anywhere in the event frame should be flagged with CODE 6 ("2 in 1").

Appendix 2.
Monte Carlo

Certain essential nonmeasurable quantities (acceptances and efficiencies) were determined by Monte Carlo techniques.

The Monte Carlo procedure was divided into two parts. The first part used the best knowledge of the neutrino flux, theoretical differential cross sections, and target nuclei properties to generate events; for each event, it produced four vectors of particles involved in a reaction under study.

The second part translated the particle four vectors into a pattern of hits, with energies and times, in the detector. The best knowledge of geometry, materials, and performance of the detector was used to simulate the passage of reacting particles through the detector. Thus ionization loss and nuclear scattering of particles was simulated, and using the measured resolution functions, a data tape compatible with the raw data format was produced. The Monte Carlo data tapes were analyzed with the same programs used for the real data, and the performance of the analysis program on simulated events with known kinematics was determined. For a detailed description see Ref. 17.

Appendix 3.

Charge Radius

Neutrinos may interact with photons in higher order processes and thus aquire a charge radius. Three diagrams that contribute to $\nu_\mu e \rightarrow \nu_\mu e$ scattering are illustrated in Fig. 3.1. Fig. 3.1(a) is the first order diagram ($O(G_F)$) that occurs through the neutral current. It is described by the following effective Lagrangian:

$$L_I = \frac{G_F}{2\sqrt{2}}\bar{\nu}_\mu\gamma_\mu(1+\gamma_5)\nu_\mu 2\bar{e}\gamma^\mu(g_V + g_A\gamma_5)e$$

$$g_V = -1/2 + 2\sin^2\theta_w$$

$$g_A = -1/2$$

The first order diagram results in the Standard Model cross section described in Chapter 1. Fig. 3.1(b) are the two second order diagrams ($O(G_F\alpha)$) that occur through the exchange of a photon. These diagrams are considered the charge radius diagrams and described by the following effective Lagrangian:

$$L_{II} = \frac{G_F}{\sqrt{2}}\bar{\nu}_\mu\gamma_\mu(1+\gamma_5)\nu_\mu(\frac{\sqrt{2} < r^2 >}{6G_F})(4\pi\alpha)\bar{e}\gamma^\mu e$$

where $(\frac{<r^2>}{6})$ quantifies all effects at the neutrino vertex in terms of a charge radius, $< r^2 >$, which is allowed to be positive or negative; $4\pi\alpha$ is the electromagnetic coupling; there is no spin flip of the neutrino. The total cross section is computed from the total effective Lagrangian, $L = L_I + L_{II}$. The cross section derived from L differs from that derived from L_I only by the substitution: $\sin^2\theta_w \rightarrow \sin^2\theta_w + \delta$ where δ is given below:

$$\sigma = \frac{G_F m_e E_\nu}{2\pi}((g_V \pm g_A)^2 + \frac{1}{3}(g_V \mp g_A)^2)$$

$$g_V = -1/2 + 2(\sin^2\theta_w + \delta)$$

$$g_A = -1/2$$

$$\delta = \frac{\sqrt{2}\pi\alpha}{3G_F} < r^2 >$$

The upper sign in the cross section is for $\nu_\mu e \rightarrow \nu_\mu e$ and the lower sign is for $\bar{\nu}_\mu e \rightarrow \bar{\nu}_\mu e$. The above clarification was obtained by consultation with Prof. J.E. Kim. Please see Ref. 42 for further details.

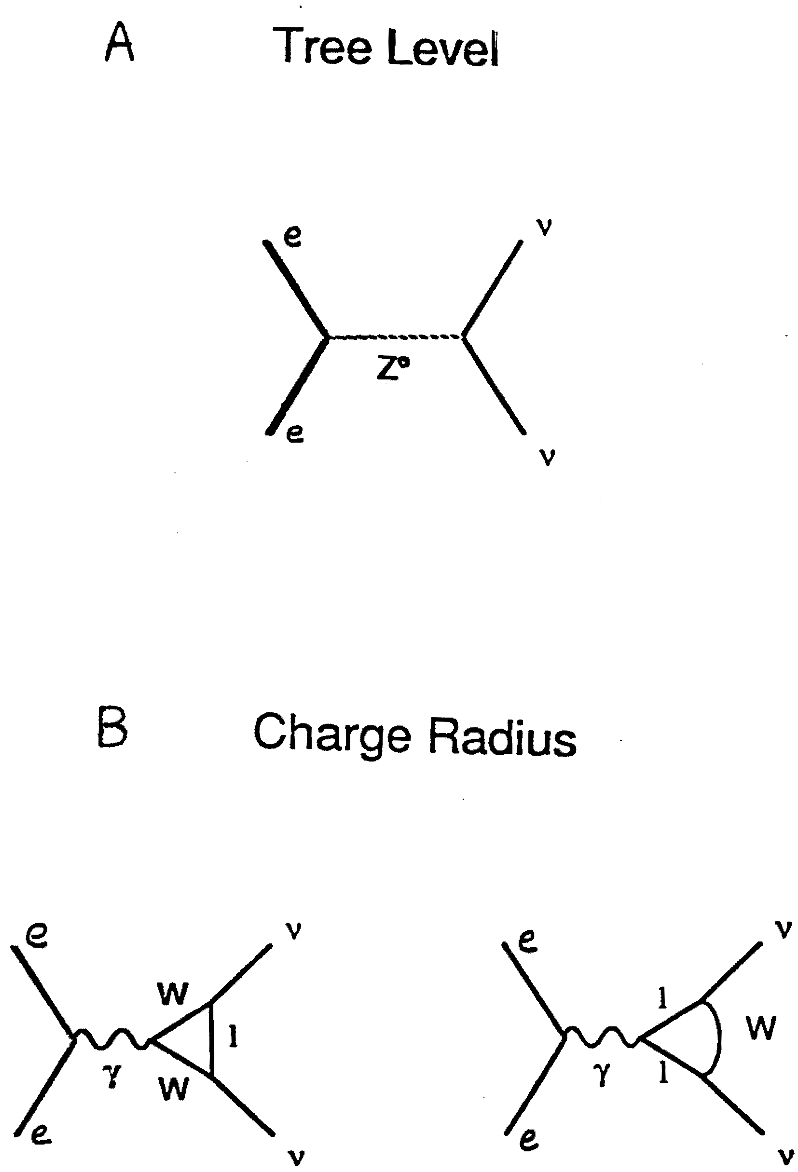

Figure 3.1 (a) First order diagram for $\nu_\mu e \rightarrow \nu_\mu e$ scattering through the neutral current. (b) The second order diagrams that can be quantified in terms of a charge radius for the muon neutrino.

References

1. Weinberg, S., Phys. Rev. Lett. **19**, 1264, (1967).

2. Salam, A., *Elementary Particle Theory*, ed. N.Svartholm, Almqvist and Wiksell, Stockholm, (1968).

3. Glashow, S.L., Nucl. Phys. **22**, 579, (1961).

4. Bagania, P.,*et. al.*, Phys. Lett. **129B**, 130, (1983).

5. Arnison, G., *et. al.*, Phys. Lett. **129B**, 273, (1983).

6. Georgi, H. and Glashow, S.L., Phys. Lett. **33**, 438, (1974).

7. Blewitt, G., et. al., Phys. Rev. Lett. 55, 2114 (1985).

8. Amaldi, U., et.al., Phys Rev D, **36**, 1385 (1987).

9. Kyuldjiev, A. V., Nuclear Physics, **B243** (1984) 387-397.

10. Abe, K., *et al.*, Phys. Rev. Lett. **58**, No. 7, 636-639 (1987).

11. Ahrens, L.A.,*et al.*, Phys. Rev. Lett. **51**, No. 17, 1514 (1983).

12. Ahrens, L.A.,*et al.*, Phys. Rev. Lett. **54**, No. 1, 18 (1985).

13. Ahrens, L.A., et. al., NIM, **A254**, 515 (1987).

14. Hughlock, B.W., Ph.D. Thesis (1983), Brown University, Dept. of Physics, unpublished.

15. Tatsumi, S., Ph.D. Thesis, Osaka University (1984), unpublished..

16. Doughty, D.C., Ph.D Thesis (1984), University of Pennasylvania, Dept. of Physics, unpublished..

17. Stern, E.G., Ph.D. Thesis (1986), State University of New York at Stonybrook, unpublished.

18. Hurley, M.B., Ph.D. thesis, University of Pennsylvania (1984), unpublished..

19. Callas, J.L., Ph.D. thesis, Brown University (1987), unpublished..

20. Ahrens, L.A.,*et. al.*, Physical Review D, **34**, No. 1, 75-84(1986).

21. Tseng, E., The Determination of the Neutrino Flux of the Brookhaven Wide Band Beam, Undergraduate thesis, Brown University (1987).

22. Ahrens, L.A., et.al., Phys. Rev. D **23**, 2732 (1985).

23. Program Notes PN97, PN98, PN100, Fermilab Computer Department.

24. Connolly, P.L., and Cutts, D., "The Use of Microprocessors in a Neutrino Experiment", Proc. of the CERN Topical Conference on the Application of Microprocessors to High Energy Physics Experiments, CERN, Geneva, Switzerland, MAY, 1981 (unpublished).

25. Tatsumi, S., Ph.D Thesis, Osaka University (1984), unpublished..

26. Hughlock, B.W., Ph.D. Thesis, Brown University (1983), unpublished..

27. C. H. Llewellyn-Smith, Phys. Rep. **3C**, 261(1972).

28. R. M. Barnett, Phys. Rev. D **15**, 97(1977).

29. L. A. Ahrens, et.al., Phys. Rev. D, **35**, No. 3, 785(1987).

30. Rein, D. and Sehgal, L.M., Annals of Phys., **133** , 79, (1981).

31. James, F. and Roos, M., Computer Physics Communications, **10**, 343 (1975)..

32. Panmån,J., Rappoteur's talk, Proc. Neutrino '84, Dortmound, (1984) to be published.

33. Reines,F., Gurr,H.S., and Sobel,H.W., Phys. Rev. Lett. **37**, 315, (1976).

34. Beg,M.A.B., Marciano,W.J., Ruderman,M., Phys. Rev. **D17**, 1395, (1978).

35. Grosser,D., Phys. Lett. **166B**, 340, (1986).

36. Roussarie,A., XII Int. Conf. on High Energy Phys. Berkeley, 1986.

37. Murtagh,M.J., "Review of Neutrino-Electron and Antineutrino-Electron Elastic Scattering Experiments", talk given at NEUTRINO '84, XIth International Conf. on Neutrino Physics and Astrophysics, Nordkirchen, FRG (1984).

38. Altarelli,G., Talk presented at the 23rd Int. Conf. on High Energy Physics, Berkeley, (1986).

39. Sutherland,P., Ng,J.N., Flowers,E., Ruderman,M. and Inman,C., Phys. Rev. **D13**, 2700, (1976).

40. Beg,M.A., Marciano,W.J. and Ruderman,M., Phys. Rev. **D17**, 1395, (1978).

41. Kim,J.E., Phys. Rev. **D14**, 3000, (1976); Marciano,W.J. and Sanda,A.I., Phys. Lett. **67B**, 303, (1977).

42. Kim,J.E., Mathur,V.S., Okubo,S., Phys. Rev. **D9**, 3050, (1974).

43. Marciano,W.J., Talk presented at Neutrino 88, the 13th international conference on neutrino physics and astrophysics, Tufts University, June 1988, proceeding to be published.